LA-14270-T
Thesis

Multispectral Thermal Imagery and Its Application to the Geologic Mapping of the Koobi Fora Formation, Northwestern Kenya

Los Alamos
NATIONAL LABORATORY
EST. 1943

The World's Greatest Science Protecting America

This thesis was accepted by the Earth and Planetary Sciences Department, The University of New Mexico, Albuquerque, New Mexico, in partial fulfillment of the requirements for the degree of Master of Science. The text and illustrations are the independent work of the author, and only the front matter has been edited by the IM-1 Writing and Editing Staff to conform with Department of Energy and Los Alamos National Laboratory publication policies.

Los Alamos National Laboratory, an affirmative action/equal opportunity employer, is operated by the University of California for the United States Department of Energy under contract W-7405-ENG-36.

This report was prepared as an account of work sponsored by an agency of the United States Government. Neither the Regents of the University of California, the United States Government nor any agency thereof, nor any of their employees make any warranty, express or implied, or assume any legal liability or responsibility for the accuracy, completeness, or usefulness of any information, apparatus, product, or process disclosed, or represent that its use would not infringe privately owned rights. Reference herein to any specific commercial product, process, or service by trade name, trademark, manufacturer, or otherwise does not necessarily constitute or imply its endorsement, recommendation, or favoring by the Regents of the University of California, the United States Government, or any agency thereof. The views and opinions of authors expressed herein do not necessarily state or reflect those of the Regents of the University of California, the United States Government, or any agency thereof. Los Alamos National Laboratory strongly supports academic freedom and a researcher's right to publish; as an institution, however, the Laboratory does not endorse the viewpoint of a publication or guarantee its technical correctness.

LA-14270-T
Thesis
Issued: February 2006

Multispectral Thermal Imagery and Its Application to the Geologic Mapping of the Koobi Fora Formation, Northwestern Kenya

Mary K. Greene

Los Alamos
NATIONAL LABORATORY
EST. 1943

The World's Greatest Science Protecting America

MULTISPECTRAL THERMAL IMAGERY AND ITS APPLICATION TO THE GEOLOGIC MAPPING OF THE KOOBI FORA FORMATION, NORTHWESTERN KENYA

BY

MARY K. GREENE

ABSTRACT OF THESIS

Submitted in Partial Fulfillment of the
Requirements for the Degree of

Master of Science
Earth and Planetary Sciences

The University of New Mexico
Albuquerque, New Mexico

December, 2005

ACKNOWLEDGEMENTS

I have quite a few people to thank for their efforts on my behalf and on behalf of this project.

First of all I thank my primary advisors, Dr. Jack Harris of Rutgers University and the Koobi Fora Field School, Dr. Paul Pope of Los Alamos National Labs' ISR-2 Space and Remote Sensing Sciences group, and Dr. Louis Scuderi of the Earth and Planetary Sciences Department, UNM. Each of these gentlemen contributed in a unique way to this study, and without their efforts and dedication to a multidisciplinary and multi-institutional approach for this Masters, it would never have been completed. **Dr. Harris** shared over thirty years of Koobi Fora geological and archaeological expertise with me and was an outspoken advocate for my mapping project from its earliest inception all the way through to its completion. He spent many hours with me walking over outcrops and answering all questions I had with the vast stores of his knowledge of Koobi Fora. **Dr. Pope** also took on this project with nothing more than blind faith that it could be done and spent countless hours working to acquire imagery for the map. He spent an extensive amount of his own time teaching me the basics of remote sensing physics, image processing, and digital map creation. His exacting eye caught my mistakes and helped me to create the best map possible, and I am deeply indebted to him for teaching me the digital cartographic skills that Koobi Fora research so badly needs. Finally, **Dr. Scuderi**, another believer in my abilities before they were proven, provided challenging coursework and brought twenty-plus years of remote sensing experience to this project. He provided me with the direction needed to search the literature for background

information relevant to this study and many valuable criticisms of my written work. His support for this project and encouragement of me as I fought to create the map were unwavering and complete, and I am immensely grateful for his dedication to the multi-institutional approach that the project required. I thank all of these gentlemen for all of the time that they invested in my education, for giving me the freedoms and constraints I needed to succeed in this work, and, above all, for their undying patience.

I also thank the two remaining members of my thesis committee at UNM, Dr. Peter Fawcett and Dr. Les McFadden. Both of these gentlemen lent their invaluable support to this project and provided valuable criticisms of my written work.

The Koobi Fora Field School and Rutgers, the State University of New Jersey, provided all field support for this project. I am indebted to future doctors David Braun, Briana Pobiner, Purity Kuira, Emmanuel Ndiema, and Rhonda Quinn for their scientific, logistical and moral support as well as camaraderie while at Koobi Fora. Dr. Gail Ashley and Dr. Kay Behrensmeyer, visitors to the Field School, provided field education on the Holocene stromatolites, sedimentology and characteristics of the Koobi Fora Formation. Dr. Giday Woldegabriel, a researcher at both Koobi Fora and in the Rift Valley in his native Ethiopia, provided essential criticism of the geology portion of this manuscript. I also thank the Kenyan support staff of the Field School and base camp for keeping us fed and safe in a very harsh and dangerous environment. Dr. Michael Kobrick and Terri Formico of NASA's Jet Propulsion Laboratory provided me with the SRTM DEM that was used to make my final map 3-dimensional, an added perspective which is invaluable to the field geologist. ISR-2 Space and Remote Sensing Sciences group at Los Alamos National Laboratory provided the computing and software resources necessary to complete this project, and the MTI ground station at Sandia National Laboratory worked with us to target the imagery accurately.

Lastly, and most importantly of all, I thank my husband, **Brian Harmon**, for everything. He had no idea that when I made him swear to follow me to the ends of the Earth that I'd make him keep good on his promise. Brian was my companion throughout this entire wonderful journey, and the success of the fieldwork portion of this study was due to the outstanding GPS skills he possesses and which he passed on to me and the Field School students. More importantly, he lent calm and patience to my life that was much needed during the 80-hour-plus weeks I worked to complete my fieldwork, coursework and thesis in addition to my job duties. He has endured much for the sake of this project and has given me a world of love and support during its course. I am a very lucky woman indeed.

I dedicate this work to my grandmother, Roberta O'Connor Cremer, and my mother, Barbara Cremer Greene. They spent the first five years of my life trying to figure out where I'd gotten to, gave up, and spent the rest of their lives sending me out into the world to explore, discover, and bring them back tales of the world they'd never see. Tá mo chroí istigh ionat go deo.

Multispectral Thermal Imagery and its Application to the Geologic Mapping of the Koobi Fora Formation, Northwestern Kenya

Mary K. Greene

B.S., Geology
B.S., Anthropology
Beloit College, 1995

M.S., Earth and Planetary Sciences
University of New Mexico, 2005

ABSTRACT

The Koobi Fora Formation in northwestern Kenya has yielded more hominin fossils dated between 2.1 and 1.2 Ma than any other location on Earth. This research was undertaken to discover the spectral signatures of a portion of the Koobi Fora Formation using imagery from the DOE's Multispectral Thermal Imager (MTI) satellite. Creation of a digital geologic map from MTI imagery was a secondary goal of this research.

MTI is unique amongst multispectral satellites in that it co-collects data from 15 spectral bands ranging from the visible to the thermal infrared with a ground sample distance of 5 meters per pixel in the visible and 20 meters in the infrared.

The map was created in two stages. The first was to correct the base MTI image

using spatial accuracy assessment points collected in the field. The second was to mosaic various MTI images together to create the final Koobi Fora map. Absolute spatial accuracy of the final map product is 73 meters.

The geologic classification of the Koobi Fora MTI map also took place in two stages. The field work stage involved location of outcrops of different lithologies within the Koobi Fora Formation. Field descriptions of these outcrops were made and their locations recorded. During the second stage, a linear spectral unmixing algorithm was applied to the MTI mosaic.

In order to train the linear spectra unmixing algorithm, regions of interest representing four different classes of geologic material (tuff, alluvium, carbonate, and basalt), as well as a vegetation class were defined within the MTI mosaic. The regions of interest were based upon the aforementioned field data as well as overlays of geologic maps from the 1976 Iowa State mapping project. Pure spectra were generated for each class from the regions of interest, and then the unmixing algorithm classified each pixel according to relative percentage of classes found within the pixel based upon the pure spectra values. A total of four unique combinations of geologic classes were analyzed using the algorithm. The tuffs within the Koobi Fora Formation were defined with 100% accuracy using a combination of pure spectra from the basalt, vegetation, and tuff.

TABLE OF CONTENTS

LIST OF FIGURES

LIST OF TABLES

INTRODUCTION

The Koobi Fora hominid fossil region of northwestern Kenya (Figure 1) is the source of more remains of early hominins between 2.1 and 1.2 Ma in age than any other place in the world. Important specimens from the area include KNM-ER 1470, a complete skull of *Homo habilis* (Leakey and Leakey, 1978), and archaeological site

Figure 1. U.S. State Department map of Kenya. Koobi Fora is outlined in blue.

FxJj 20, the earliest evidence of controlled fire use in the human fossil record (Harris and Isaac, 1997).

Paleontological research began at Koobi Fora in 1968 with a preliminary investigation by Dr. Richard Leakey of the National Museums of Kenya (Leakey and Leakey, 1978). In addition to thousands of specimens of classes *Probiscoidea, Giraffidae, Bovidae, Suidae,* and *Equidae,* 450 hominin specimens from genera *Australopithecus* and *Homo* have been found in sediments ranging from 4.3 to 1.2 million years in age (Leakey et al., 1995; Feibel et al., 1989). Figure 2 illustrates the fossil collection areas that have been defined within the region since the Koobi Fora Research Project first began its work.

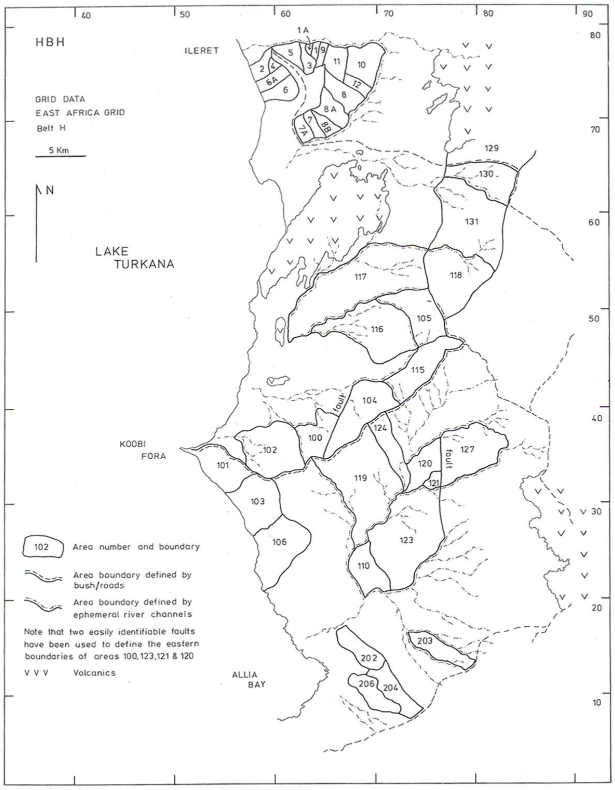

Figure 2. Koobi Fora geographic and collection areas map (Leakey and Leakey, 1978).

Geologic maps based on aerial photographs of Koobi Fora were first created in the 1970s and 1980s (Bainbridge, 1976; Bowen, 1974; Burggraf, 1976; Frank, 1976; Key and Watkins, 1988; White, 1976). Geologists have used Landsat imagery to map the faults and crystalline rock of Kenya's Gregory Rift, which lies south of Koobi Fora (Vidal, 1988; Tibaldi and Ferrari, 1988). More recently, geographers have used Landsat imagery to map land use in the Kakamega district of Kenya and vegetation cover near Lake Naivasha, Kenya, both of which lie to the south of the study area (de Jong and Riezebos, 1990; Barsi, 1995). Asfaw et al. (1990) have used Landsat imagery and Space Shuttle photography to explore the geology of fossiliferous sediments in the Afar Depression and Ethiopian Rift. However, the use of satellite imagery and a geologic spectral classification technique to create a detailed map of the Koobi Fora Formation has not been attempted prior to this study. As certain members within the Formation are associated with fossil and archaeological discoveries (Feibel et al., 1989), a surface geologic map created via spectral unmixing may assist in the planning of future expeditions to areas of Kenya and Ethiopia where analogous sediments exist.

Goals of this study and study method

This research was undertaken to discover the unique spectral signatures of the different lithologies within the Koobi Fora Formation, and to use this information to digitally map the surface geology of part of the Koobi Fora Formation in a detailed spatial and spectral manner. Imagery from the DOE's Multispectral Thermal Imager (MTI) satellite is the basis of the digital map. MTI collects data with a 5 meter ground sample distance (GSD) in the visible portions of the electromagnetic spectrum and a 20 meter GSD in the infrared and thermal infrared portions of the electromagnetic spectrum.

Figure 3 illustrates the basic study method. MTI data were collected, pre-processed and taken into the field. Observations of the weathered surface geology of the Koobi Fora Formation were made and recorded and spatial correction points were obtained. A mosaic of Koobi Fora imagery was then created and georeferenced. The mosaic, used along with the aforementioned field observations and historical map data, was used to define geologic regions of interest with which to train a spectral unmixing program. The program produced a series of surface geologic maps for individual lithologies within the Koobi Fora Formation, and the overall accuracy of these maps was calculated.

The end result is a multispectral surface geologic map of part of Koobi Fora that has an absolute spatial accuracy of 73 meters in latitude and longitude. The best unmixing result produced a set of geologic classification maps with 100% overall accuracy. The worst result produced a set of geologic classification maps with 60% overall accuracy.

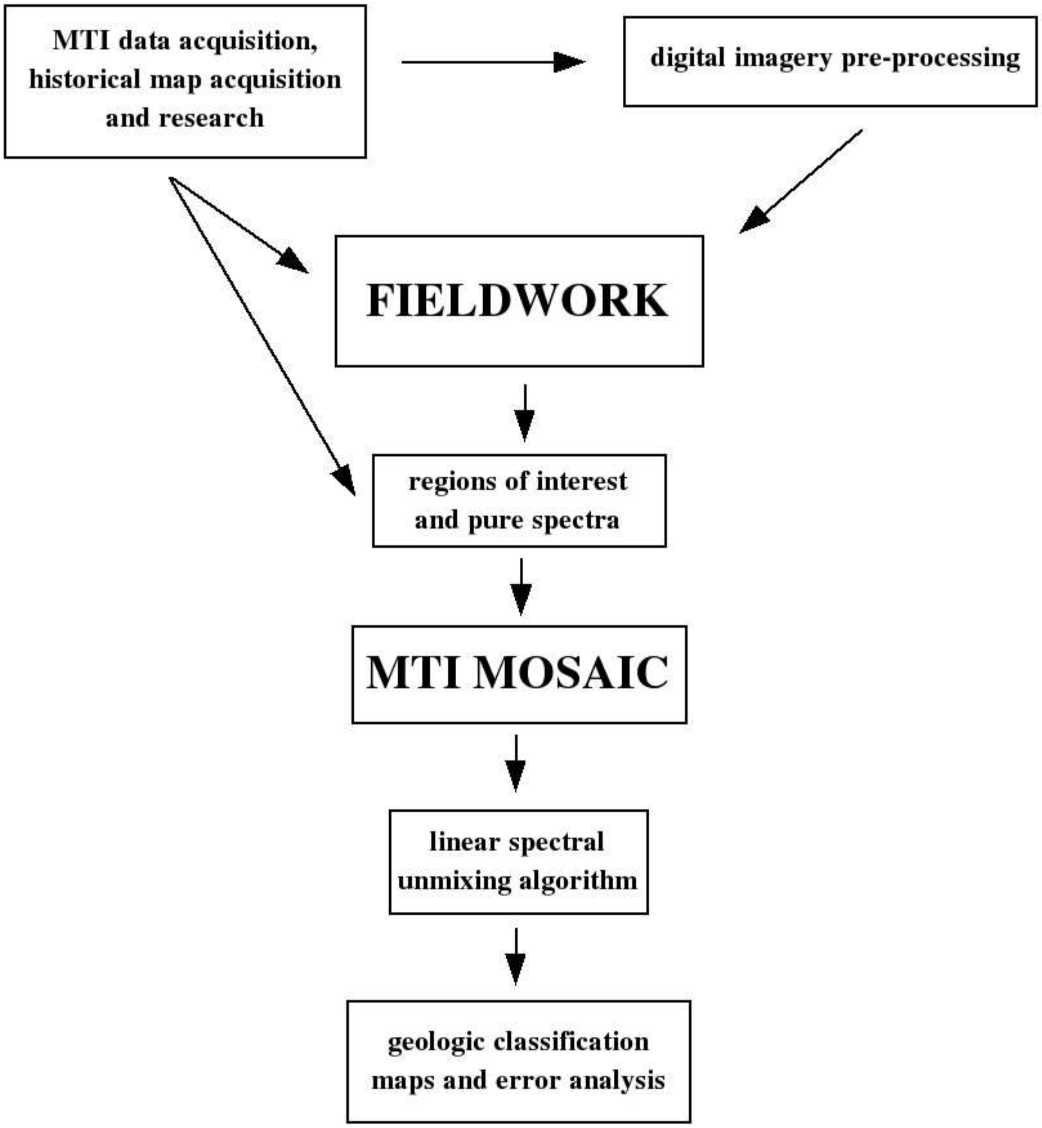

Figure 3. Basic study method for the Koobi Fora MTI mapping project.

CHAPTER 1
THEORY

1.1 The electromagnetic spectrum and principles of electromagnetic energy

The foundation of remote sensing is the electromagnetic spectrum. All matter at temperatures above 0 degrees K radiates electromagnetic energy in accordance with basic wave theory (Lillesand and Kiefer, 2000). The Sun radiates electromagnetic energy at 5800 degrees K, which then travels at the speed of light to the surface of the Earth. This radiative output is the source of most passive remote sensing reflection and emission.

The electromagnetic spectrum is a continuum that defines the wavelengths of electromagnetic energy that are reflected and emitted by matter (Sabins, 1997). The divisions by wavelength of this spectrum are shown in Figure 1.1. It is important to note that the portion of this spectrum visible to the human eye is very small relative to all possible wavelengths of energy. The most powerful justification for multispectral remote sensing studies is that they show us what we can't see about the Earth's surface.

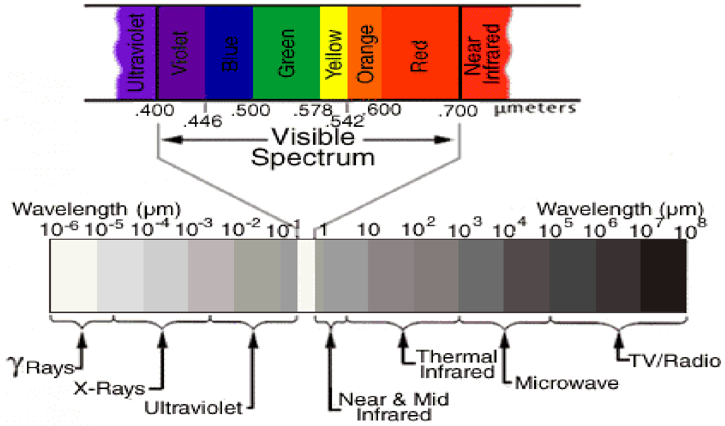

Figure 1.1. The electromagnetic spectrum.

The basis of remote sensing is the many types of interactions that occur as a result of incident radiation from the Sun on an object and emission of energy from the Earth's surface. Figure 1.2 shows a simplified diagram of these interactions.

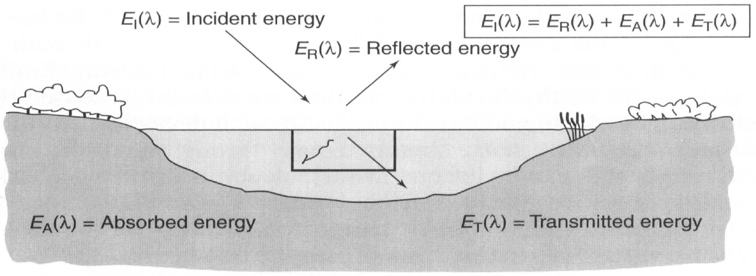

Figure 1.2. Simplified relationships of electromagnetic energy with the Earth's surface (Lillesand and Kiefer, 2000).

For energy incident on the Earth's surface, it follows through the Law of Conservation of Energy that

(Equation 1.1)

$$E_I(\lambda) \equiv E_R(\lambda) + E_A(\lambda) + E_T(\lambda)$$

where

$$E_I(\lambda) = \text{energy incident on an object}$$
$$E_R(\lambda) = \text{energy reflected by the object's surface}$$
$$E_A(\lambda) = \text{energy absorbed by the object}$$

and

$$E_T(\lambda) = \text{energy transmitted through the object} \quad .$$

From this relationship, reflectance is defined as the energy incident on an object minus the energy absorbed by an object and the energy transmitted through an object. However, an object's reflectance is not a directly measurable quantity. All satellite sensors measure the spectral radiance, L_λ , of the Earth's surface. This quantity is defined as the total reflected and emitted electromagnetic energy that is captured by the satellite sensor. Because electromagnetic energy at different wavelengths interacts with the Earth's surface in different ways, reflected energy is the primary detectable component of spectral radiance below 3 microns in wavelength and reflected and emitted energies are the primary detectable components of radiance above 3 microns.

1.2 Visible and near infrared energy and reflectance

The Earth's surface reflects the Sun's energy diffusely, which produces different reflectance spectra for surface materials. Reflectance spectra of wavelengths below 3 microns, which includes the visible, near infrared, and mid-infrared portions of the electromagnetic spectrum, can be used to gather information about surface geology and vegetation cover (Drury, 2001). The near infrared portion of the electromagnetic spectrum, defined as the range from 0.77 microns to 0.91 microns, can detect healthy vegetation and transition metals such as manganese and ferric iron. Finally, many different igneous and sedimentary lithologies have distinct reflectance spectra in the shortwave infrared portion of the electromagnetic spectrum, which is defined as the region from 1.0 to 3.0 microns in wavelength.

1.3 Thermal infrared energy and emissivity

The portion of the electromagnetic spectrum above 3 microns in wavelength is classified as the thermal infrared. In this region, heat is analogous to light and the emissivity and temperature of surface materials is the property that is inferred. Kirchoff's law states that

(Equation 1.2)

$$\epsilon_{(\lambda)} = \alpha_{(\lambda)}$$

or, that an object's emissivity is equal to its absorptance. As with spectral reflectance, the intensity and spectral characteristics of the energy emitted from a body depend on the composition and temperature of that body (Gupta, 2003). The simplified Stefan-Boltzmann law states that

(Equation 1.3)

$$M = \sigma T^4$$

where

$$M = total\ radiant\ exitance\ of\ a\ material's\ surface,\ Watts\,(W)\,m^{-2}$$
$$\sigma = Stefan - Boltzmann\ constant,\ 5.6697\ x\ 10^{-8}\,W\,m^{-2}\,K^{-4}$$

and

$$T = absolute\ temperature\,(K)\ of\ the\ emitting\ material$$

(Lillesand and Kiefer, 2000). This equation describes the behavior of a blackbody substance, which is an ideal hypothetical substance that absorbs all radiation incident upon it. In reality, all materials approximate the behavior of a blackbody substance, and thus emissivity of real substances is measured as a proportion of the ideal.

The thermal infrared region of the electromagnetic spectrum is defined as the range from 3 microns to 1 millimeter in wavelength. The portion of the spectrum between 8 and 12 microns is particularly good for distinguishing different geologic materials.

1.4 Spectral reflectance and emission spectra of Earth surface materials

Much work has been done on the spectral reflectance and emissivity of geologic materials in the laboratory (Siegal and Gillespie, 1980; Beaumont and Foster, 1992; Drury, 2001; Gupta, 2003; Price, 1995; Sabins, 1997). As stated previously, because of the different interactions that minerals and rocks have with different wavelengths of energy, multispectral thermal images can provide information about surface geology. In the visible and near infrared portions of the electromagnetic spectrum, electronic processes such as transition in the outer orbital electrons in transition metals (Fe, Mn, Cu) cause the changes that are detectable by remote sensing. In the shortwave infrared and thermal infrared portions of the electromagnetic spectrum, the variable vibrational processes of atoms and molecules within a material are responsible for their emission properties (Gupta, 2003).

Silicon dioxide (SiO_2) is the most abundant oxide component of common rock-forming minerals on the Earth's surface. Figure 1.3 illustrates the emission spectrum for quartz, the pure mineral form of SiO_2. Quartz has a strong absorption feature in the thermal infrared between wavelengths 8 and 9 microns. The reflectance spectrum of quartz exhibits a peak from 1.5 to 1.75 microns in the shortwave infrared (Figure 1.4).

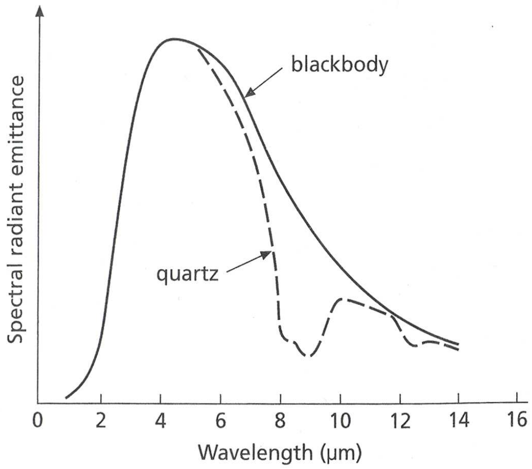

Figure 1.3. The emission spectrum for quartz. Note the distinct absorption feature at 8 microns (Drury, 2001).

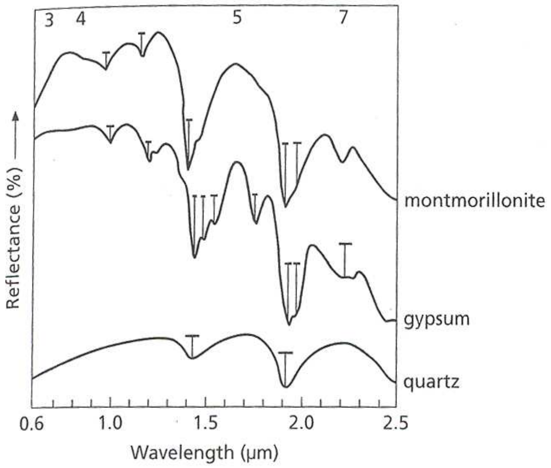

Figure 1.4. The reflectance spectrum for quartz. Note the reflectance peak between 1.5 and 1.75 microns in all three minerals (Drury, 2001).

The silicate families of minerals contain various amounts of the elements Si and O. Their transmission spectra are all somewhat similar to that of quartz, but the main absorption trough shifts up the electromagnetic spectrum in accordance with the type of silicate structure involved (Drury, 2001).

Carbonate rocks also make up a significant portion of Earth's land surface. They display a reflectance peak in the region between 1.5 and 1.75 microns. They also display distinctive spectral absorptance at 2.35 microns and high thermal emissivity in the range from 8 to 12 microns.

Iron in its many forms is the most common metal on the Earth's surface. The ferric ion (Fe^{3+}) displays a distinct reflectance peak in the near infrared region between wavelengths 0.7 and 0.8 microns (Figure 1.6). The thermal infrared features of iron and manganese oxides also produce significant emission peaks near 8 microns (Hunt, 1980).

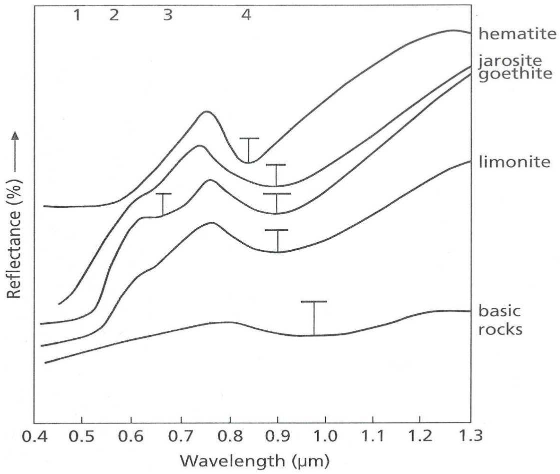

Figure 1.5. The reflectance spectrum for common iron oxide minerals. Note the reflectance peak in the region from 0.7 to 0.8 microns in all of the minerals (Drury, 2001).

The Koobi Fora Formation and the surrounding volcanics are very lithologically diverse. All of the tuff members of the Koobi Fora Formation are composed of SiO_2 in the form of volcanic glass, the biogenic carbonates found throughout the study area are made up of $CaCO_3$, and the basalts are Fe and Mg rich. As shown above, remote sensing studies have been shown to be able to discriminate these lithologies based on their reflection and emittance characteristics. MTI senses wavelengths that distinguish each of these elements, and as such is ideally suited for the discrimination required in this study. The characteristics of MTI are discussed in the following chapter.

CHAPTER 2
THE MULTISPECTRAL THERMAL IMAGER SATELLITE

2.1 MTI mission and unique characteristics

The Multispectral Thermal Imager (MTI) is a United States Department of Energy satellite. The satellite is a collaborative research and development project between Los Alamos National Laboratory, Sandia National Laboratory, and the Savannah River Technology Center. Its purpose is to demostrate advanced multispectral and thermal imaging in support of nonproliferation, environmental, and global mapping efforts (Bell and Weber, 2001). An artist's rendition of the MTI flight configuration is shown in Figure 2.1.

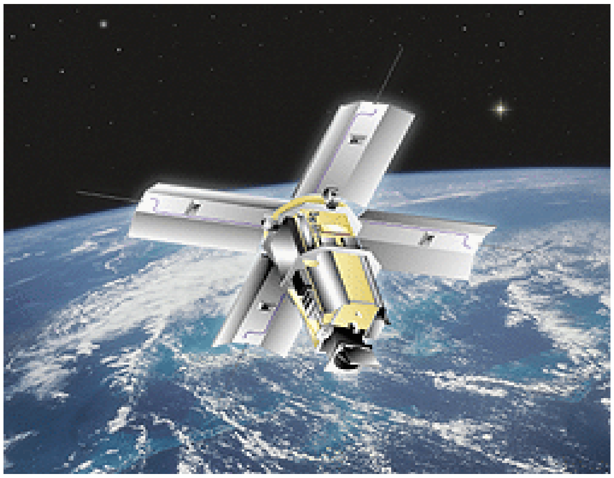

Figure 2.1. Artist's rendition of MTI flight configuration.

MTI was launched on March 12, 2000 into a sun-synchronous polar orbit with 1 PM and 1 AM local time equatorial crossing times. The satellite co-collects data from 15 different spectral bands over a 12 by 24 kilometer target area. The GSD of the visible bands is 5 meters per pixel, while that of the near, mid-, and thermal infrared bands is 20 meters per pixel. Figure 2.2 illustrates the spectral bands sensed by MTI and the total radiance of each band. Table 2.1 shows the details of the MTI satellite bands and Table 2.2 is a comparison of MTI to other current Earth imaging satellites. MTI's distinguishing characteristics relative to other multispectral sensors are that it co-collects data from more bands than any other satellite currently in orbit, and that the resolution of the visible and infrared bands is superior to all other multispectral satellites.

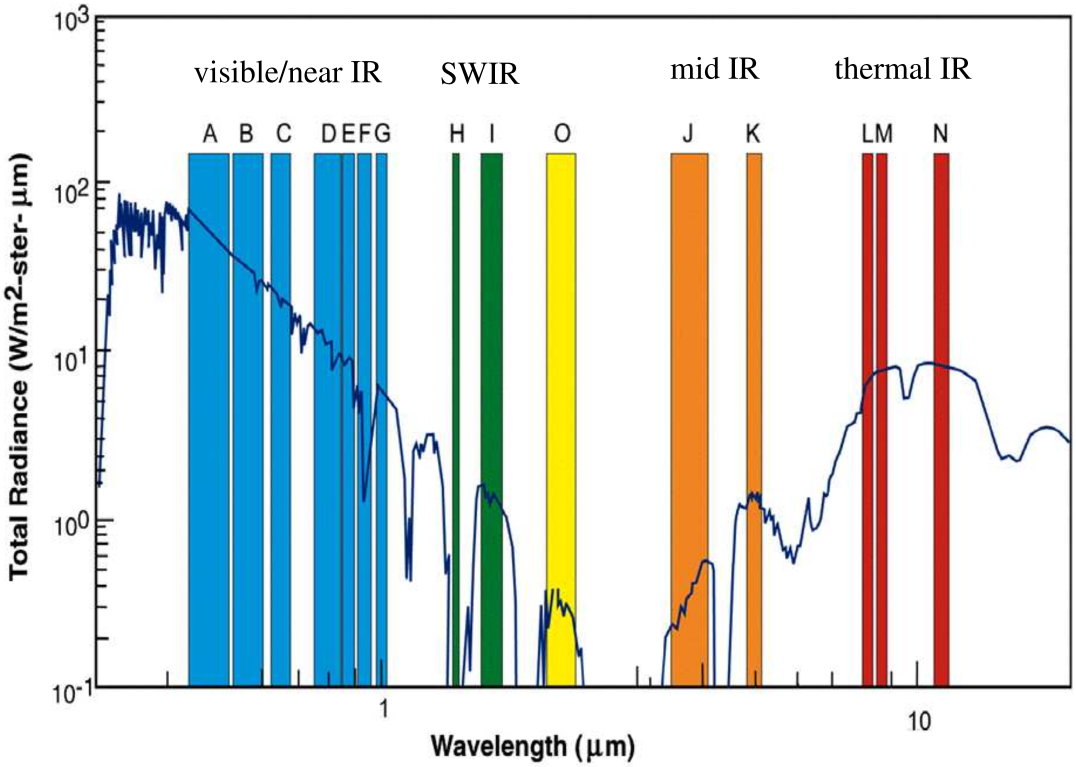

Figure 2.2. MTI spectral band versus wavelength for all bands sensed. MTI collects radiance data from five subgroupings within the electromagnetic spectrum, denoted here by different colors (Clodius, 2004).

MTI BAND	WAVELENTH MINIMUM (microns)	WAVELENGTH MAXIMUM (microns)	WAVELENGTH AVERAGE (microns)	GROUND SAMPLE DISTANCE (m)	DETECTOR MATERIAL	DESIGNED TO DETECT
A	0.45	0.52	0.49	5	Si-PIN	blue “true color”
B	0.52	0.60	0.56	5	Si-PIN	green “true color”
C	0.62	0.68	0.65	5	Si-PIN	red “true color”
D	0.76	0.86	0.81	5	Si-PIN	vegetation
E	0.86	0.89	0.88	20	InSb	water vapor
F	0.91	0.97	0.94	20	InSb	water vapor
G	0.99	1.04	1.02	20	InSb	water vapor
H	1.36	1.39	1.38	20	InSb	cirrus
I	1.54	1.75	1.65	20	InSb	surface
J	3.49	4.10	3.80	20	InSb	surface
K	4.85	5.05	4.95	20	InSb	atmosphere
L	8.01	8.39	8.20	20	HgCdTe	atmosphere/surface temperature
M	8.42	8.83	8.63	20	HgCdTe	surface temperature
N	10.15	10.70	10.43	20	HgCdTe	surface temperature
O	2.08	2.37	2.23	20	InSb	surface temperature

Table 2.1. MTI spectral band characteristics (Clodius, 2004).

	SPOT XS	**Landsat 7 ETM**	**MTI**
terrain coverage, kilometers	60 by 60	90 by 90	12 by 24
spatial resolution, m	20, all bands	15/30, visible/IR	5/20, visible/IR
visible bands, micrometers	X	0.45-0.52	0.45-0.52
	0.50-0.59	0.52-0.61	0.52-0.60
	0.61-0.68	0.63-0.69	0.62-0.68
infrared and thermal IR bands, micrometers	0.79-0.89	0.78-0.90	0.76-0.86
	X	X	0.86-0.89
	X	X	0.91-0.97
	X	X	0.99-1.04
	X	X	1.36-1.39
	X	1.55-1.75	1.54-1.75
	X	2.10-2.40	2.08-2.37
	X	X	3.49-4.10
	X	X	4.85-5.05
	X	X	8.01-8.39
		X	8.42-8.83
	X	10.40-12.50	10.15-10.70

Table 2.2. A comparison of the MTI satellite with other Earth imaging systems.

2.2 MTI payload

MTI's payload includes a telescope and a cryogenically cooled focal plane on which the 15 linear spectrally sensitive detector arrays and built-in calibration sources reside. Spectral data is collected in pushbroom fashion as the satellite ground track moves across the targeted scene. The telescope optics transfer this information onto the three sensor chip assemblies (SCAs) located on the focal plane, illustrated in Figure 2.3. Bands A-D are collected by silicon photodiode detectors, bands E-K and O are collected by InSb photodiodes, and the thermal bands L-N are collected by HgCdTe diodes. Each of these semiconductors was selected because of its superior ability to detect the radiance properties of particular wavelengths.

2.3 Damage to MTI since launch

The satellite originally contained an elaborate calibration system, with sources of thermal and cold reference calibration for the SCAs. Seven months after launch, failure of a portion of the electronics caused the calibration systems to fail and the aperture door to remain in its open position. MTI has been damaged further by five sun looks, which occurred as a result of the loss of the gyro system (Clodius, 2004). This loss causes the satellite to send incorrect information about its orientation to the ground control station. It can thus be mistakenly pointed directly at the sun when it passes over a magnetic pole. Table 2.3 summarizes the sun looks of the satellite and their effect on images procured for this study. The result of each of these looks was damage to the detectors on SCAs one and three, which produces a blurred result in some bands in the final images.

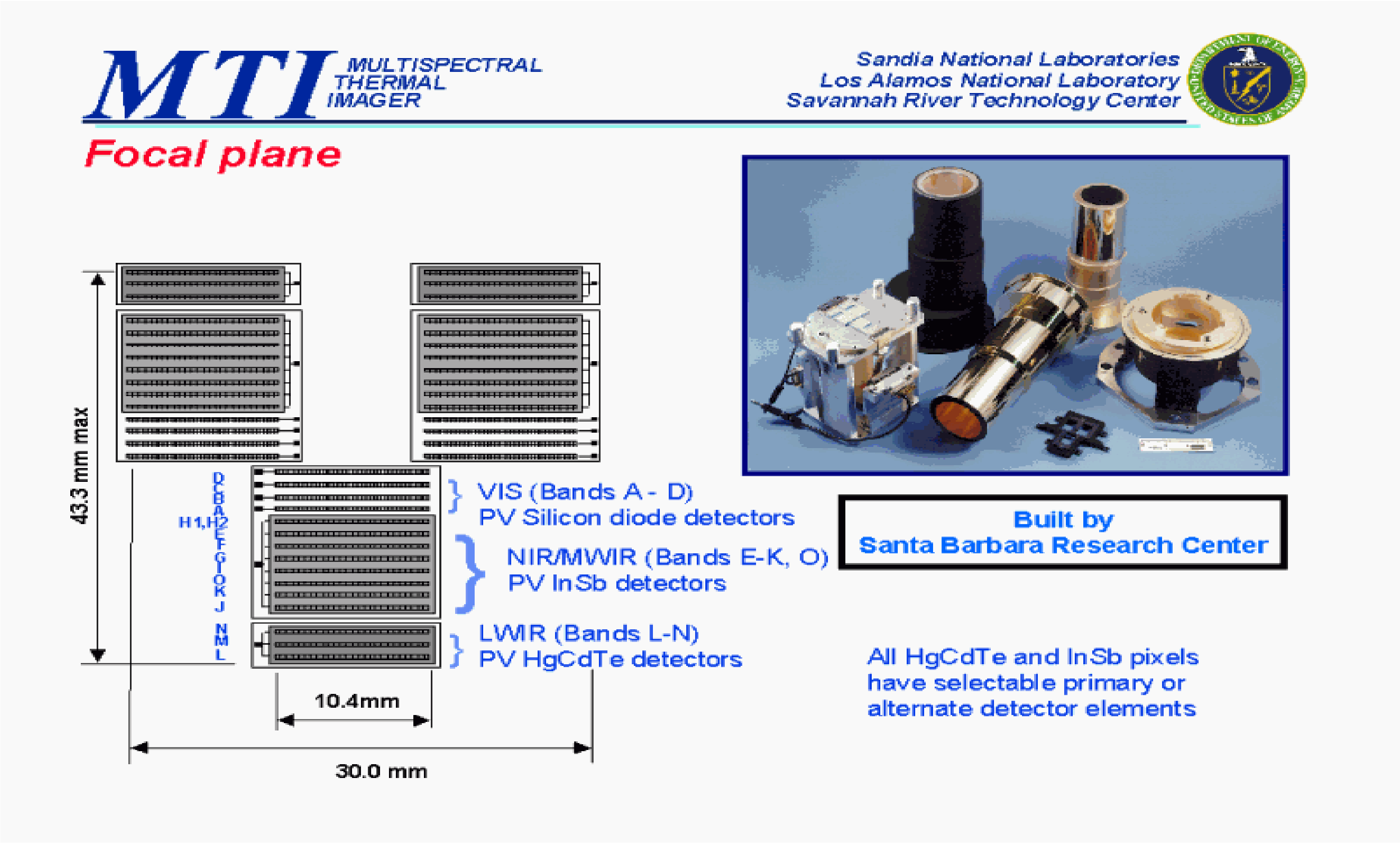

MTI MULTISPECTRAL THERMAL IMAGER

Sandia National Laboratories
Los Alamos National Laboratory
Savannah River Technology Center

Focal plane

} VIS (Bands A - D)
PV Silicon diode detectors

} NIR/MWIR (Bands E-K, O)
PV InSb detectors

} LWIR (Bands L-N)
PV HgCdTe detectors

Built by
Santa Barbara Research Center

All HgCdTe and InSb pixels
have selectable primary or
alternate detector elements

Figure 2.3. MTI focal plane layout.

After the first sun look, the orientation of the satellite was changed by 180 degrees. This caused sensor chip arrays one and three to be reversed in the final mosaic created for this study.

MTI SUN EXPOSURE DATE	Koobi Fora mosaic imagery affected
11/12/01	110662, 110685
05/24/03	152567, 153633

Table 2.3. MTI sun looks that affected the imagery used in this study.

All of these problems have had minimal effects on the subsequent imagery procured by the satellite. No sensors were completely destroyed by any of the sun looks, which is a remarkable outcome for such a series of events. The damage to the SCAs was visible on only a few of the images procured for this study, and it occurred in bands that were not used to create the final mosaic.

MTI is currently in a holding pattern, which means that it is not collecting imagery at this time. As the satellite has already exceeded its intended mission length by two years, the future of the MTI project remains uncertain.

CHAPTER 3
KOOBI FORA GEOLOGY AND CARTOGRAPHIC HISTORY

3.1 Structural geology and tectonics

The Koobi Fora depositional basin lies in the Turkana Depression, north of the Gregory Rift of the East African Rift System (Baker, 1972). Figure 3.1 illustrates the geography of the rift. The distinguishing feature of the Koobi Fora Basin is that it is located in a trough between the major extrusive volcanic features of the Ethiopian Dome and the Kenyan Dome (Morley, 1999). Rifting began on the eastern side of Lake Turkana during the early Cretaceous and throughout the Paleogene migrated westward (Morley, 1999). The current geometry of the Turkana half graben dates to the early Pliocene, when uplift along the northwestern edge of the Kenyan Dome produced subsequent downwarping of the regional lithosphere (Key and Watkins, 1988; Savage and Williamson, 1978).

The structural evolution of the Turkana half graben is illustrated in Figure 3.2. (Morley, 1999). As Miocene synformal depression gave way to a dominant boundary fault during the Pliocene, minor faults on the eastern margin of the graben were abandoned and sediment accumulated in these areas. The current lake covers several of these half grabens and the sediment that accumulated therein (Dunkelman et al., 1988). During the Pliocene and Pleistocene epochs, movement along the boundary faults of the western-dipping monocline of the half graben produced a migrating lake shoreline, which in turn affected fluvial flow through the basin (White et al., 1981). Sedimentary

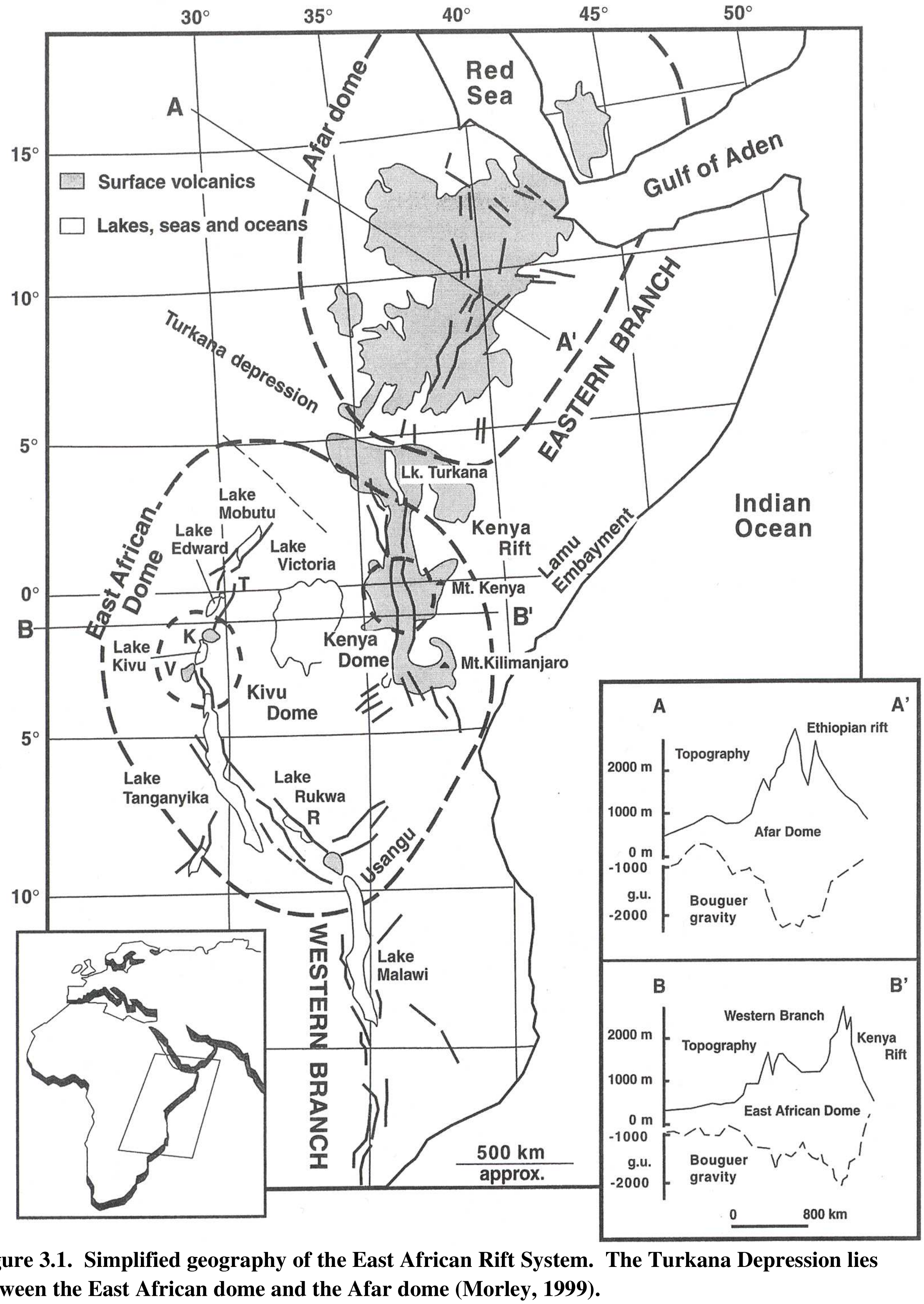

Figure 3.1. Simplified geography of the East African Rift System. The Turkana Depression lies between the East African dome and the Afar dome (Morley, 1999).

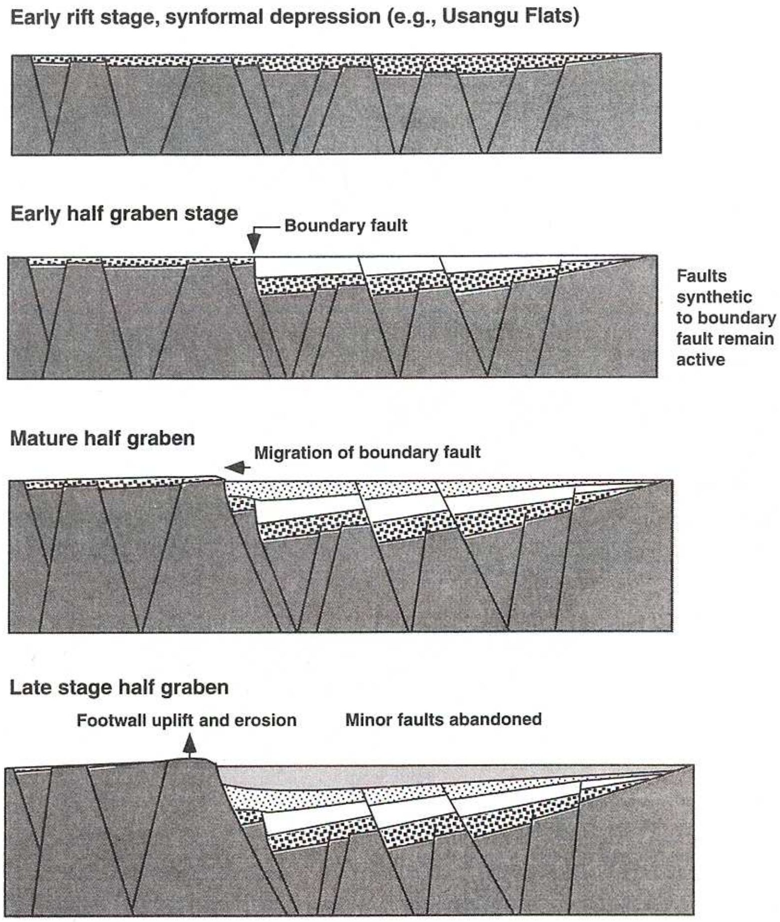

Figure 3.2. Evolution of the Turkana half graben (Morley, 1999).

deposition coincided with very active extrusive volcanic fields to the east and south of the Koobi Fora Basin (Key and Watkins, 1988).

Two major controls on sedimentary deposition in the basin through time, whether fluvial or lacustrine, have been tectonics and climate (Feibel, 1997b; Feibel et al., 1991). Lake Turkana's shoreline has migrated in part due to movement on the half graben faults. De Menocal (1995) documented shifts in African climate at 2.8, 1.7, and 1.0 Ma towards progressively cooler and drier conditions in East Africa. Less precipitation would have affected water and sediment supply into the lake. The depth of the lake has varied such that during the interval from 1.7 to 1.5 Ma the basin was dominated by the ancestral Omo River (Rogers and Harris, 1994). Given the tectonically active environment of the Turkana Depression and the variability of flow through the basin that is recorded in its sediments, it is easy to see why the Koobi Fora Formation is as lithologically complex as it is, and why different tuff and sedimentary members have proven difficult to correlate laterally throughout the basin (Brown, 1994).

3.2 Cartographic history

Bowen (1974) was the first to map the geology of the Koobi Fora region. He completed three maps at a scale of 1:50,000 for his Ph.D. dissertation. These were based on black and white aerial photographs from Huntings Survey Ltd. of Nairobi, which were taken at a scale of 1:23,000. Coverage areas of these maps were of the Ileret, Koobi Fora, and Allia Bay regions. In 1976, maps of the Karari Escarpment were published at a scale of 1:6,000 by a research team from Iowa State University under the direction of Carl Vondra and Bruce Bowen. A two sheet set was made for the northern Karari Escarpment by Bainbridge (1976) and Frank (1976), and a four sheet set for the southern Karari escarpment by White (1976) and Burggraf (1976). Most recently, Key and Watkins (1988) of the Ministry of Environment and Natural Resources, Mines and Geology Department, Republic of Kenya, produced a general geologic map of the Sabarei district of northwestern Kenya. This map included Koobi Fora geology, but relied heavily on the Iowa State studies for its basis. Their study included a composite map at a scale of 1:250,000.

3.3 The Koobi Fora Formation

The first stratigraphic classification of the area, also produced by Bowen (1974), has been extensively revised by Brown and Feibel (1986, 1991) due to their work in correlating fluvial tuffaceous deposits across the Turkana basin (Feibel et al., 1989). Regional work on the tuffaceous sediments of the basin has linked the formations of western Lake Turkana and southern Ethiopia with those of the Koobi Fora Formation (Feibel, 1997a; Brown, 1994). Behrensmeyer and Isaac (1997) provide a synthesis of the stratigraphic and paleogeographic work that has been conducted over the last 25 years at Koobi Fora. Table 3.1 shows a summary of the sedimentary facies that various researchers have recorded and the environment of deposition that correlates with each facies. Figure 3.3 illustrates the idealized environments of deposition of the sedimentary facies.

Findlater (Interpretive)	Vondra and Bowen (Descriptive)
Lacustrine low energy	Includes laminated siltstone facies
Lacustrine high energy	Includes arenaceous bioclastic carbonate facies
Alluvial delta plain	Includes lenticular fine-grained sandstone and lenticular bedded siltstone facies
Alluvial valley plain	Lenticular conglomerate, sandstone, and mudstone facies
Alluvial coastal plain	Not distinguished

Table 3.1. Facies models and correlative environments of deposition for the Koobi Fora Formation (Behrensmeyer and Isaac, 1997).

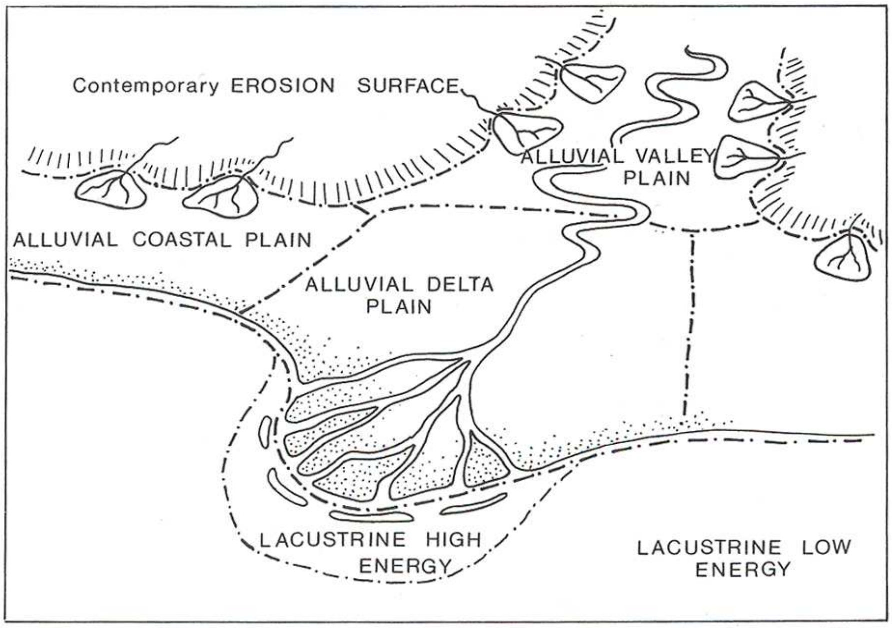

Figure 3.3. Idealized environments of deposition as envisioned by Findlater (1978).

This study sought to map part of the Koobi Fora Formation as defined by Brown and Feibel (1986). The portion included in this study dates from 2.6 Ma to 1.2 Ma and consists of four members of the Formation. These are the Upper Burgi Member, the KBS Member, the Okote Member, and the Chari Member. Each of these members is bounded by or contains a fluvially reworked tuff to which it lends its name. Also present in the study area are the extrusive volcanics of the Suregai highlands and alluvium deposits, which have been derived from erosion of the sediments of the Koobi Fora Formation and the extrusive volcanics to the east of the basin. A generalized stratigraphic column of the Koobi Fora Formation is shown in Figure 3.4.

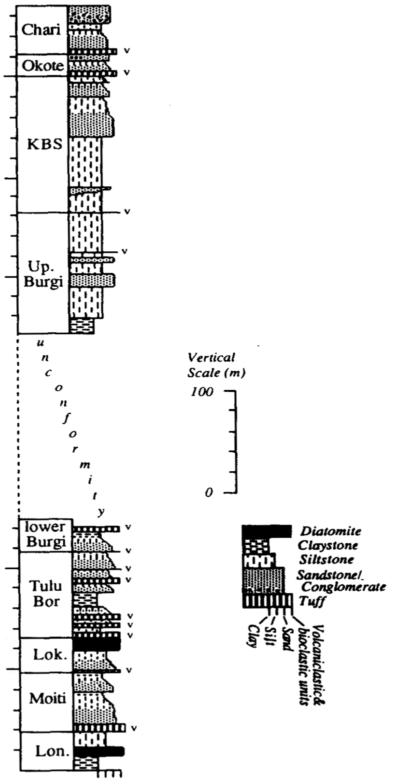

Figure 3.4. Generalized stratigraphic section for the Koobi Fora Formation (Brown, 1994). The portion of the Formation above the Burgi Unconformity was mapped in this study.

The Burgi Member is a total of 120 m thick, the upper 109.1 m of which is exposed in the study area. The base of the Lower Burgi Member is the Burgi Tuff, which dates to 2.6 Ma (Feibel et al., 1989). The overlying sediments consist of four fining-upward sedimentary cycles (Brown and Feibel, 1986), with a major unconformity between the Lower and Upper submembers (Brown, 1994). The medium to coarse grained sandstones at the base of each fining-upward cycle are overlain by massive dark olive claystones and laminated siltstones. Of particular interest in the Upper Burgi Member are the many forms of carbonate that exist. Carbonate cemented orange sandstones are prevalent throughout Area 105 (Figure 3.5). Molluscan packstones

(Figure 3.6) cap the claystones in the southern portion of the study area. The packstone is made up of shells that belong to Williamson's (1982) molluscan faunal zone 3. They are in many cases covered in black desert varnish (Munsell color 10 YR 3/2), and Brown and Feibel (1986) report that iron and manganese oxides are abundant in the Upper Burgi. The Upper Burgi Member corresponds to the fluvial or deltaic flood plain depositional facies of Findlater (Behrensmeyer and Isaac, 1997).

Figure 3.5. Orange carbonate cemented sandstone of the Upper Burgi Member in Area 105.

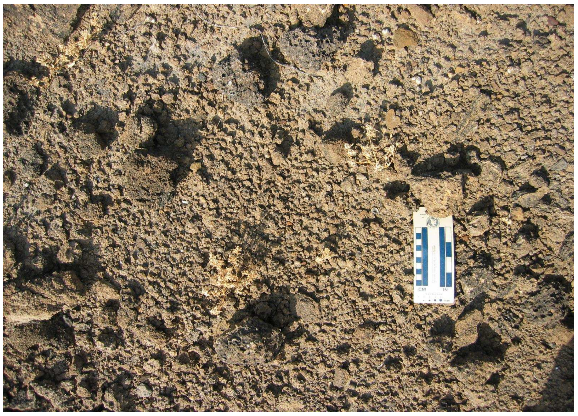

Figure 3.6. Molluscan packstones with heavy desert varnish in Area 105.

The KBS Member of the Koobi Fora Formation lies above the Upper Burgi Member. The KBS Tuff, located at the base of the member, dates to 1.88 Ma (McDougall, 1985). The member is characterized by abundant bioclastic carbonates, stromatolites, and thick channel litharenites (Brown and Feibel, 1986). Calcium carbonate nodules are so abundant in this member that they coat the post-KBS erosion surface near many archaeological sites (Figure 3.7).

Figure 3.7. Carbonate nodules on the post-KBS erosion surface at FxJj 1.

The Okote Member consists of the Okote Tuff Complex (Figure 3.8). The Okote Tuff, which is a single tuff layer within the complex, dates to 1.65 Ma (McDougall, 1985). It is easily distinguished from the other tuffs in the complex by pumice clasts up to 30 cm in diameter (Brown and Feibel, 1986). Its type section is 21.6 meters thick. The member is best defined as a series of small fluvial tuffaceous channels, with some basalt pebble conglomerates and reddened mudstones present in the sequence (Brown and Feibel, 1986). Areas of channel gravels are locally common, as is illustrated in the FxJj 18 site complex.

Figure 3.8. Okote Tuff Complex near river channel site FwJj 1, Ileret.

The Chari Tuff dates to 1.39 Ma (McDougall, 1985) and forms the base of the Chari Member. It crops out as a buff capstone in the northeastern portion of the Ileret region and along the Karari Escarpment. The member is deeply incised by fluvial channels, which appear to have eroded most of the sandstones and claystones that cap the Chari Tuff in its type section (Brown and Feibel, 1986).

3.4 Other lithologies

3.4.1 Volcanic formations

Though the volcanic history of the northwestern part of Kenya is diverse, the Koobi Fora region is dominated by the Miocene Nakwele Formation and the Miocene to Pliocene Gombe Group. Both can be categorized as flood basalts and associated pyroclastics. The Nakwele Formation is made up of phyric and aphyric basalts and rhyolitic ignimbrites and dates from 14-12 Ma (Key and Watkins, 1988). It crops out to the east of the Ileret region at the base of the Suregai highlands. The aphyric tholeiitic flood lavas of the Gombe Group date from 5.79 to 3.28 Ma and make up the Kokoi Horst (Figure 3.9), the southern portion of the Surgei highlands just north of the Karari

Escarpment, and the volcanics to the east of the Karari Escarpment (Key and Watkins, 1988).

Figure 3.9. The Gombe basalts of the Kokoi Horst.

3.4.2 Alluvium

The alluvium within the study area consists of three classes of sandy material differentiated by depositional type. Beach sands consisting of well rounded quartz grains are found along the lake shore and make up the spit near base camp at Koobi Fora. Aeolian sands are locally abundant at the southern tip of the Kokoi Horst and are made up of quartz and silt. Finally, the sand beds that make up the dry rivers are a menagerie of well rounded to angular quartz, ferrous minerals, and bits of pyroclastics.

It is important to note that vegetation distribution is highly correlated with water courses in this arid environment. Gallery forests cover 90 to 100% of the banks of the dry river and stream beds, where their roots can tap into the water that runs deep below the surface (Figure 3.10). Grasses are also abundant along the lake shore. While rocks and minerals are spectrally dominant in areas where vegetation cover is less than 40%

(Smith et al., 1990), a condition which describes the Koobi Fora landscape accurately, it is important to note the relationship between river and stream bed alluvium and vegetation.

Figure 3.10. Stream bed alluvium and gallery forest along the Ileret River.

CHAPTER 4
RESEARCH DESIGN AND METHODS

4.1 Introduction

Geologists have used remote sensing techniques to map the Earth's surface since the advent of aerial photography. Numerous studies of the spectral characteristics of geologic formations and vegetation using satellite imagery are found throughout both remote sensing and geologic literature (Beaumont and Foster, 1992; Sabins, 1997; Drury, 2001; de Wit, 2001). As illustrated in Chapter 2, the Multispectral Thermal Imager is a unique satellite amongst those currently in orbit. However, many of the aforementioned geologic applications of remote sensing data suffer from lack of field verification or compare what is found on the ground to laboratory spectra. Field geologists know that laboratory data is of limited use for weathered outcrops and surfaces.

With these concerns in mind, the research design for this study was formulated. The first phase of the research was to select the optimum spectral bands within the MTI collection range to map lithologies in the Koobi Fora Formation. The second phase of the research was fieldwork. This included collection of spatial correction data points and geologic classification data. The third phase of the research was to spatially correct the MTI imagery based on the ground-truthing data from the fieldwork phase. It was then possible to create a mosaic of the best MTI images obtained for the study area. Once the georeferenced mosaic was completed, regions of interest (ROIs) were defined using the field geologic classification data and historical map overlays. The ROIs were used as training data for a linear spectral unmixing image classification algorithm (Pope and Greene, 2005). Finally, the quantitative and qualitative accuracy of the percent cover maps generated by the algorithm was calculated and described.

4.2 Choosing appropriate wavelengths to detect the lithologies of interest

As documented in Chapter 1, different minerals and lithologies exhibit distinct reflective and emissive characteristics in different portions of the electromagnetic spectrum. Because of these characteristics, the first step in the map creation process was to choose appropriate spectral bands to create MTI field maps.

Since MTI has three major groupings of related wavelengths arranged around various atmospheric windows (Figure 2.2), it was decided that one band from each of these groups should be used in the study. The reflective and emissive properties of different materials, as defined in section 1.4, were also used to determine which bands would be used for the false color image-based field map. Thermal infrared band M (mosaic band 1) was chosen and assigned to red in the field map. Since there are many Tertiary basalts at Koobi Fora, and since this area is a desert near the equator, it was reasoned that these rocks would have strong emissivity in the thermal portion of the infrared. Likewise, because of the strong absorption feature of quartz in the thermal infrared, it was reasoned that the tuff deposits would exhibit a less strong but detectable signal in this band. Furthermore, carbonate surfaces are detectable in this region, because of the distinct peak in thermal emissivity between 8 and 9 microns that is found in carbonates. The color green was assigned to the near infrared band D (mosaic band 2), which is useful for detecting vegetation and ferric iron. Finally, because carbonates exhibit reflectance in the shortwave IR between 1.5 and 1.75 microns and high thermal emissivity at 8 microns, the color blue was assigned to shortwave IR band I (mosaic band 3).

4.3 Linear spectral unmixing

Multiple imagery classification methods exist whereby detailed information about Earth's surface in some areas of an image can be used to train a computer program to classify cover for an entire scene. Classification methods are broadly divided into discrete or “hard” and fuzzy classifiers (Jensen, 1996). Discrete methods assign entire pixels within an image to a single class and assume hard boundaries between classes. Fuzzy classifiers assign a relative membership value to mixed pixels and assume some degree of class mixture (Altman, 1994; Foody and Cox, 1994; Foody, 1996). In order to define class membership in a fuzzy system, pixels of pure composition are used to train a program that then calculates the percent cover of classes for the entire image. Fuzzy classification methods are better for analyzing data from regions such as Koobi Fora, where the sediments are weathered and geologic classes often blend into one another.

The mathematically simplest fuzzy classification method is linear spectral unmixing (Settle and Drake, 1993). Linear spectral unmixing is defined by

(Equation 4.1)

$$R_i = \sum_{j=1}^{m} (F_j * RE_{ij}),$$

where

$R_i = reflectance\ of\ the\ mixed\ spectrum\ in\ band\ i$

$RE_{ij} = reflectance\ in\ band\ i\ of\ endmember\ j$

$F_j = fraction\ of\ endmember\ j$

and

$m = number\ of\ endmembers\ j$

(Settle and Drake, 1993; de Wit, 2001).

The pure pixels within an image are used as the reference points from which the linear spectral unmixing equation assigns class membership. The results can be optimized by using the sum to one constraint,

(Equation 4.2)

$$\sum_{j=1}^{m} F_j = 1 \quad ,$$

although for many mixed pixels this creates a negative percentage value where very little of a particular class is found. Using the variables defined in Equation 4.1, the series of equations to solve for the percent cover of three geologic classes in any mixel pixel would be

(Equation 4.3)

$$R_1 = (F_1 * RE_{11}) + (F_2 * RE_{12}) + (F_3 * RE_{13})$$
$$R_2 = (F_1 * RE_{21}) + (F_2 * RE_{22}) + (F_3 * RE_{23})$$
$$R_3 = (F_1 * RE_{31}) + (F_2 * RE_{32}) + (F_3 * RE_{33}).$$

This series of equations can be solved for *n* numbers of pixels using the least squares method (Wolf and Dewitt, 2000).

CHAPTER 5
FIELDWORK

5.1 Fieldwork

Field correction of the imagery was necessary to correct its geometric distortions. All images procured via remote sensing are inherently distorted, either systematically, randomly, or both. Systematic distortion is best described by example. The eastward rotation of the Earth while imaging sensors are procuring data is an example of this type of distortion (Lillesand and Kiefer, 2000). The effect of the Earth's rotation in satellite imagery is that each ground swath that is scanned by the satellite is slightly to the west of the previous one. This is called skew distortion, and it is corrected by gathering and analyzing ground control information for the imagery. Examples of random distortion in imagery are line drop-outs or blurs due to sensor damage. These can sometimes be corrected using digital imagery pre-processing techniques such as resampling.

Fieldwork to ground truth and analyze the MTI imagery took place from July 2 through August 1, 2003. The field season had two main objectives, to obtain spatial correction data for the MTI imagery, and to obtain geologic classification data for the Koobi Fora Formation. This resulted in the measurement of 8 spatial accuracy assessment points (Table 5.1) and 50 geologic classification points (Table 5.2). As digital MTI imagery are export controlled, band combinations were selected and 3 large paper reference maps were created and taken into the field (Figures 5.1 through 5.3). 8 small visible spectrum (bands D,C,B, or near IR, red, and green) maps with a resolution of 5 meters per pixel were also created as reference documents for the spatial accuracy assessment (Figure 5.4). Finally, 26 small M,D,I (thermal IR, near IR, mid-IR) subscene maps were created to serve as geologic classification field reference documents (Figure 5.5). MTI Image 110685 was used for all of the fieldwork.

POINT IDENTIFIER	FIELD EASTING	FIELD NORTHING	EASTING CORRECTION	NORTHING CORRECTION	CORRECTED EASTING	CORRECTED NORTHING	HORIZONTAL PRECISION
SAA 1	195656.5	477772.8	0 m	-8.8 m	195656.5	477763.9	0.3 m
SAA 2	195230.1	466050.7	-0.8 m	-12.1 m	195229.3	466038.5	0.4 m
SAA 4	201785.8	466447.1	2.9 m	-5.7 m	201788.8	466441.3	0.3 m
SAA 5	200563.8	449648.5	5 m	0 m	200568.8	449648.5	0.1 m
SAA 6	205701.9	452101.4	-12.36 m	0 m	205689.6	452101.4	0.5 m
SAA 7	202838.1	480580.3	0 m	6.5 m	202838.1	480586.8	0.4 m
SAA 10	207069.2	453397.1	-0.2 m	4.6 m	207069.2	452301.7	0.4 m
FwJj1	N/A	N/A	N/A	N/A	197797.1	471463.1	0.3 m

Table 5.1. Spatial accuracy assessment points for Koobi Fora MTI imagery. All measurements are given in UTM WGS 84 coordinates unless otherwise noted.

Note: SAA 3 and SAA 8 were not visited. SAA 10 and FwJj 1 were points selected in the field for ground control use in the lab.

DATE	EASTING	NORTHING	POSITIONS	STD DEV	FORMATION	COMMENT
7/7/2003	197146.5	477125.0	61	0.7 m	Galana Boi	sands near FwJj 14
7/7/2003	197010.3	477223.7	61	1.5 m	Okote	mixed carbonate and quartz pebbles
7/7/2003	195490.9	475725.4	215	2.2 m	Okote	carbonate sand with large stromatolites
7/8/2003	200716.3	476975.8	115	1.8 m	alluvium	silty sands
7/8/2003	207907.4	477352.9	175	0.3 m	Upper Burgi	dark carbonate cobbles, red chert
7/8/2003	207960.1	477068.3	146	2.7 m	KBS tuff	fine tuffaceous glass grains
7/8/2003	207604.7	477860.0	115	1.2 m	alluvium	lagga sand
7/9/2003	195006.0	477742.7	107	0.5 m	alluvium	silt
7/9/2003	195590.9	477825.7	75	1.0 m	alluvium	lagga sand
7/10/2003	195473	467824.1	75	2.6 m	eroded Galana Boi	sandy soil
7/10/2003	200025.8	467183.0	61	0.6 m	alluvium	sand and basalt cobbles
7/10/2003	201776.4	466092.4	227	0.4 m	Tertiary volcanics	basalt
7/10/2003	201417.1	465207.2	66	1.7 m	Tertiary volcanics	basalt
7/17/2003	210422.2	455845.1	61	0.7 m	eroded Okote	coarse sand and pebbles
7/17/2003	210523.5	455991.4	69	2.0 m	alluvium	lagga sands
7/17/2003	210751.0	455951.1	60	0.9 m	eroded Okote	carbonate nodules
7/19/2003	206839.7	452494.8	60	2.1 m	Upper Burgi	orange carbonate sand
7/19/2003	206859.3	452603.4	60	0.7 m	eroded Okote	silt
7/19/2003	206802.7	452309.8	119	2.8 m	Upper Burgi	black shelly carbonate
7/19/2003	208501.7	453985.2	unknown, file lost	unknown, file lost	eroded Okote	carbonate and claystone

Table 5.2.A. Geologic classification points taken using the Trimble GeoExplorer II GPS.

DATE	EASTING	NORTHING	POSITIONS	STD DEV	HORIZIONTAL PRECISION	FORMATION	COMMENT
7/6/2003	199106.8	474938.1	31	0.1 m	0.4 m	Chari tuff	sandy tuff, argillaceous grains
7/6/2003	197797.1	471463.1	60	0.1 m	0.3 m	Okote	sands and silts
07/07/03	195402.3	475927.0	61	0.4 m	0.5 m	Galana Boi	stromatolites
7/12/2003	213047.7	459067.9	60	0.1 m	0.3 m	Chari tuff	fine grained tuff
7/12/2003	213072.4	459446.6	60	3.3 m	0.3 m	Okote	very fine silt
7/12/2003	214135.0	462017.6	60	0.3 m	0.3 m	KBS member	heavily cemented carbonate
7/12/2003	207345.0	450564.0	60	0.2 m	0.3 m	post-KBS erosional surface	heavily cemented carbonate sands
7/13/2003	207305.1	450552.6	60	1.6 m	0.3 m	KBS tuff	fine glass grains
7/13/2003	209050.1	451836.5	60	0.3 m	0.3 m	KBS member	heavily cemented tuff
7/14/2003	215009.5	462831.3	60	0.1 m	0.3 m	Okote	very fine silt
7/14/2003	214928.9	462623.4	60	0.2 m	0.3 m	Okote	mixed pebbles
7/14/2003	214919.6	462576.1	60	0.1 m	0.3 m	Okote	stream channel gravels
7/14/2003	214937.2	462575.1	60	0.1 m	0.3 m	Okote	conglomerated silty sand
7/14/2003	214971.9	462549.5	61	0.1 m	0.3 m	Okote	silt, caliche pebbles
7/14/2003	214960.6	462548.6	60	0.1 m	0.3 m	Okote	caliche pebbles
7/14/2003	215006.7	463005.7	60	0.6 m	0.4 m	KBS tuff	tuff weathering to glass powder
7/14/2003	214488.1	463171.4	60	1.1 m	0.3 m	Upper Burgi	clay
07/14/03	214142.3	462588.4	60	0.1 m	0.4 m	Okote	sands, gravels
7/14/2003	214340.5	462387.3	60	0.1 m	0.4 m	Okote	silty sand
7/21/2003	200512.6	449709.9	60	0.1 m	0.3 m	Upper Burgi	sandy carbonate
7/21/2003	200567.4	449692.8	60	0.1 m	0.3 m	alluvium	lagga sand
7/21/2003	200813.1	449646.1	64	1.3 m	0.3 m	Upper Burgi	clay

Table 5.2.B. Geologic classification points taken using the Trimble ProXRS GPS.

Table 5.2.B. continued

DATE	EASTING	NORTHING	POSITIONS	STD DEV	HORIZIONTAL PRECISION	FORMATION	COMMENT
7/21/2003	205521.0	451899.3	60	0.1 m	0.3 m	Galana Boi	silty sands
7/23/2003	204739.3	452025.5	60	0.9 m	0.3 m	Upper Burgi	carbonate sands
7/23/2003	205007.5	452770.4	60	0.3 m	0.3 m	unknown	undifferentiated lag
7/23/2003	204719.8	453410.0	60	1.3 m	0.3 m	unknown	sand on grassy plain
7/23/2003	204650.8	453856.1	60	1.8 m	0.4 m	Upper Burgi	tuffaceous carbonate sands
7/24/2003	209501.7	477379.8	62	0.5 m	0.3 m	Upper Burgi	carbonate gravel

DATE	EASTING	NORTHING	POSITIONS	STD DEV	HORIZONTAL PRECISION	FORMATION	COMMENT
7/20/2003	462415	214028	60	unknown	6-8 m	KBS tuff	fine tuff glass grains
7/20/2003	462376	213362	60	unknown	6-8 m	Upper Burgi/KBS contact	clay and carbonate pebbles

Table 5.2.C. Geologic classification points taken using only the Garmin V GPS.

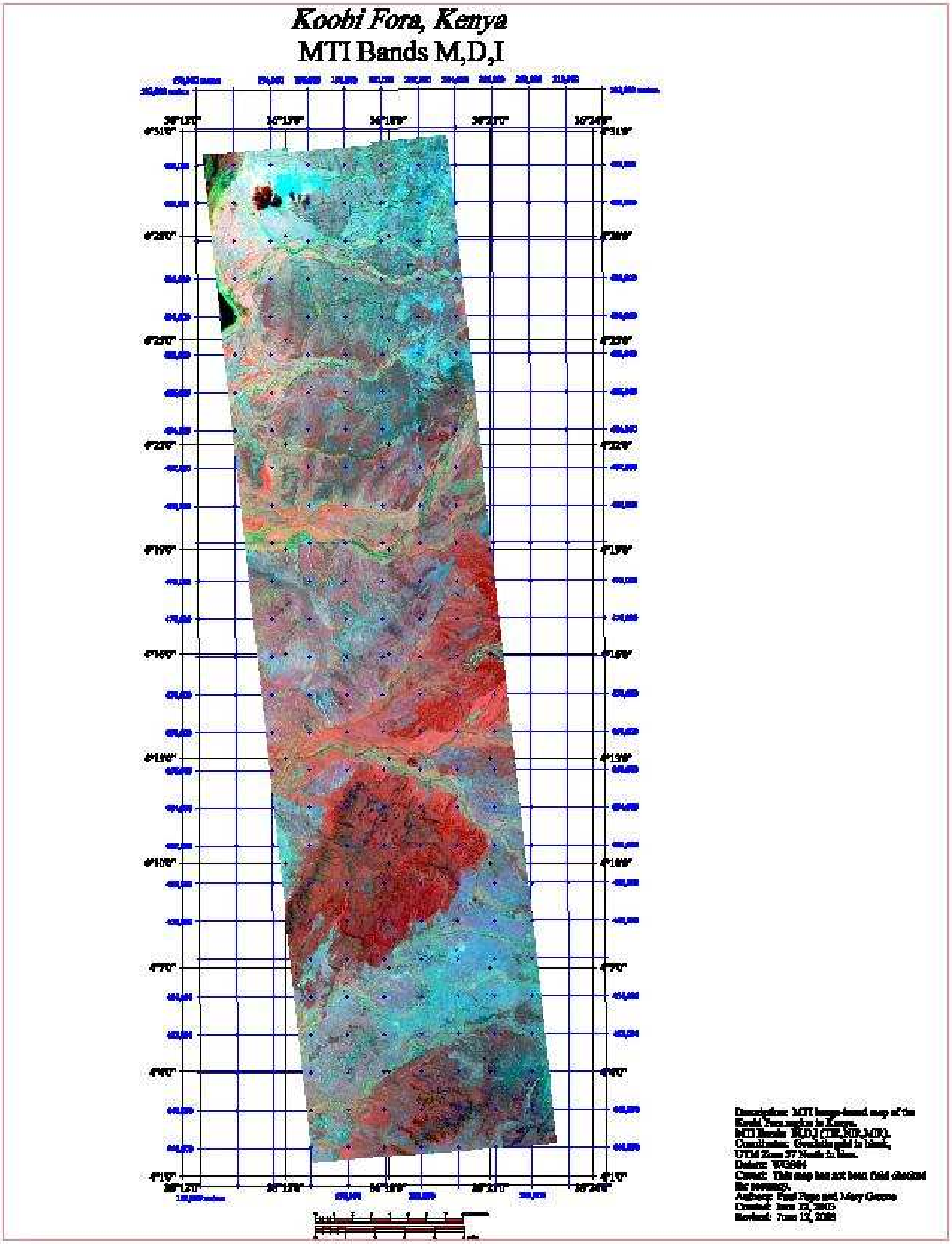

Figure 5.1. Field map of M,D,I band combination taken to Koobi Fora.

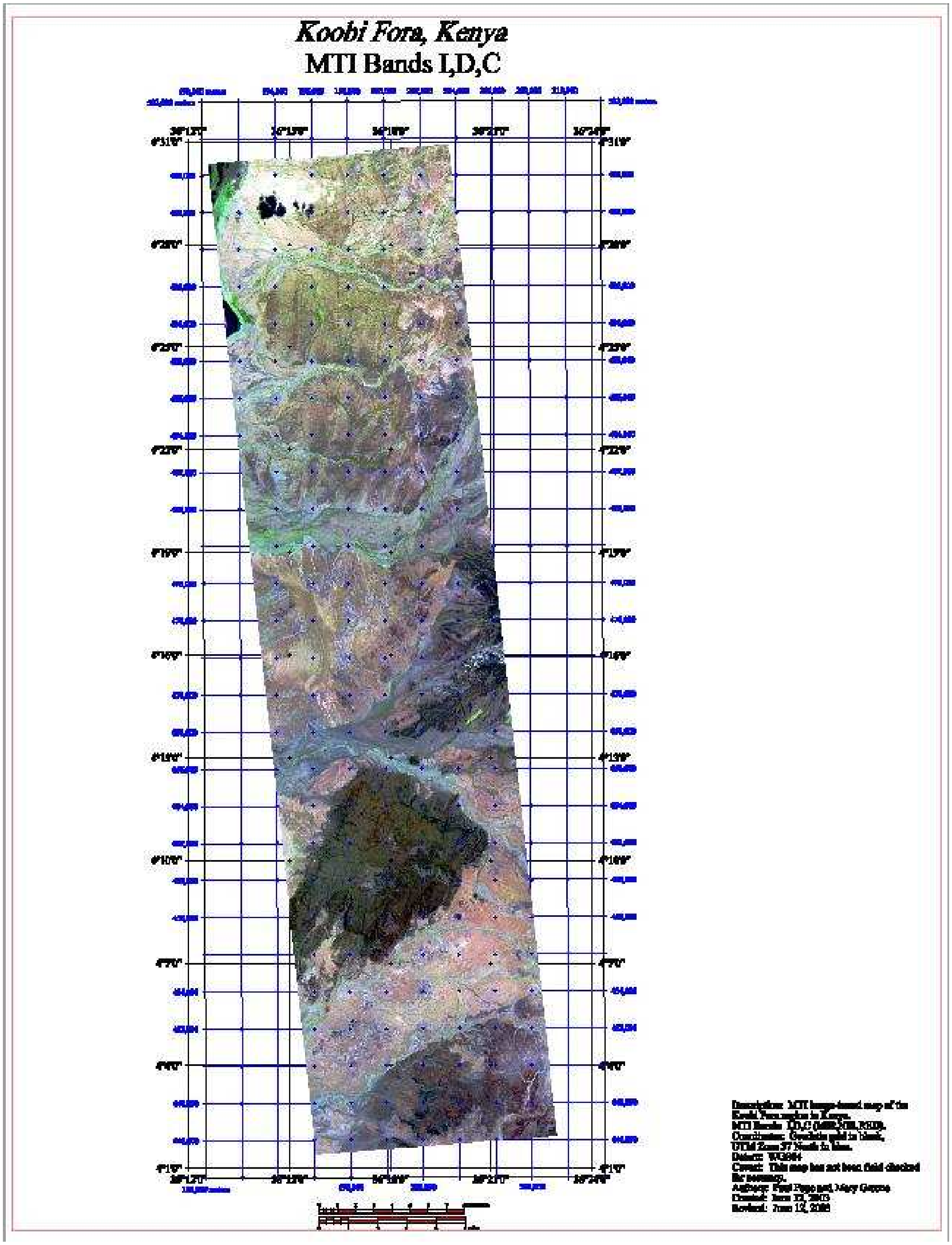

Figure 5.2. Field map of I,D,C band combination (Landsat-like) taken to Koobi Fora.

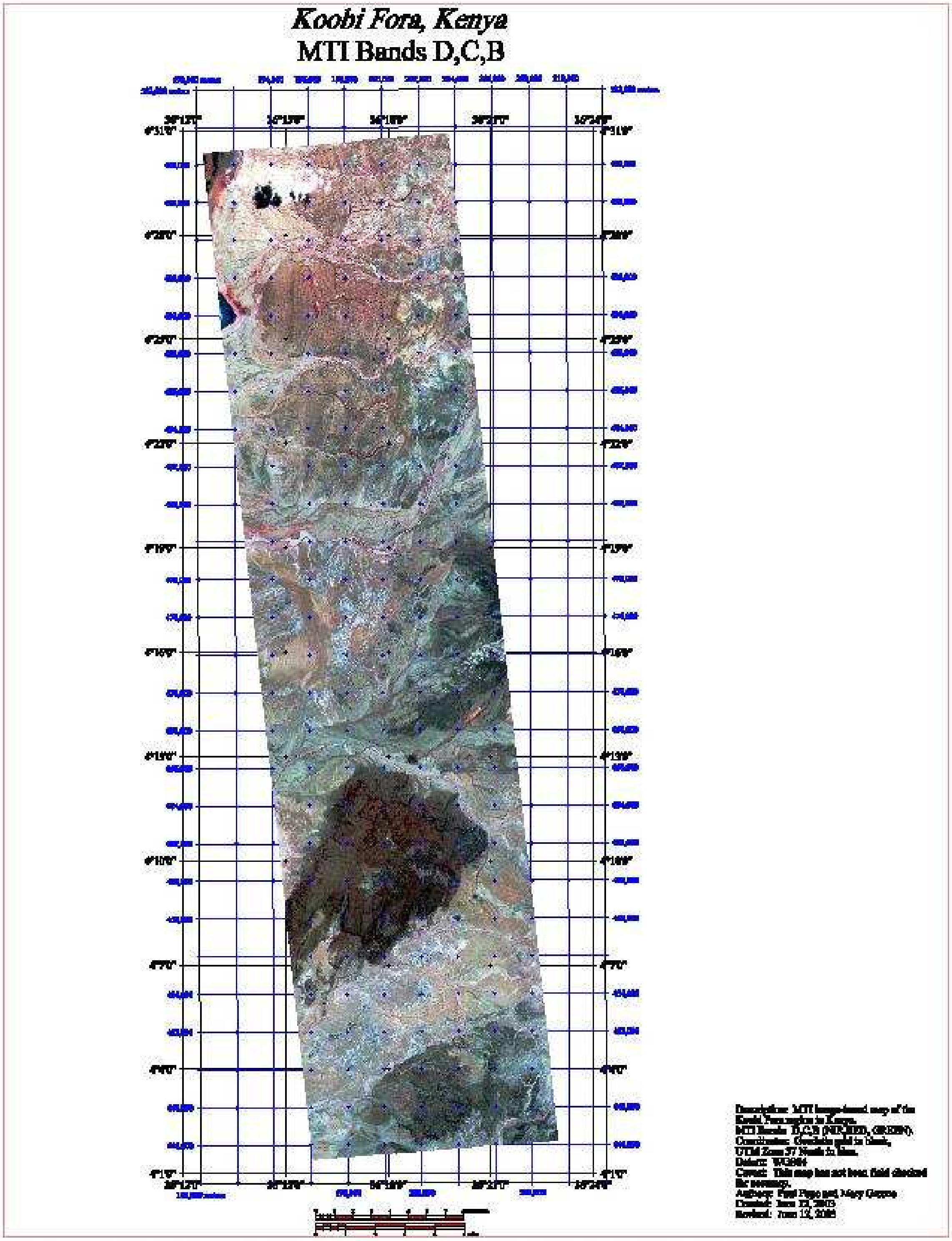

Figure 5.3. Field map of D,C,B band combination taken to Koobi Fora.

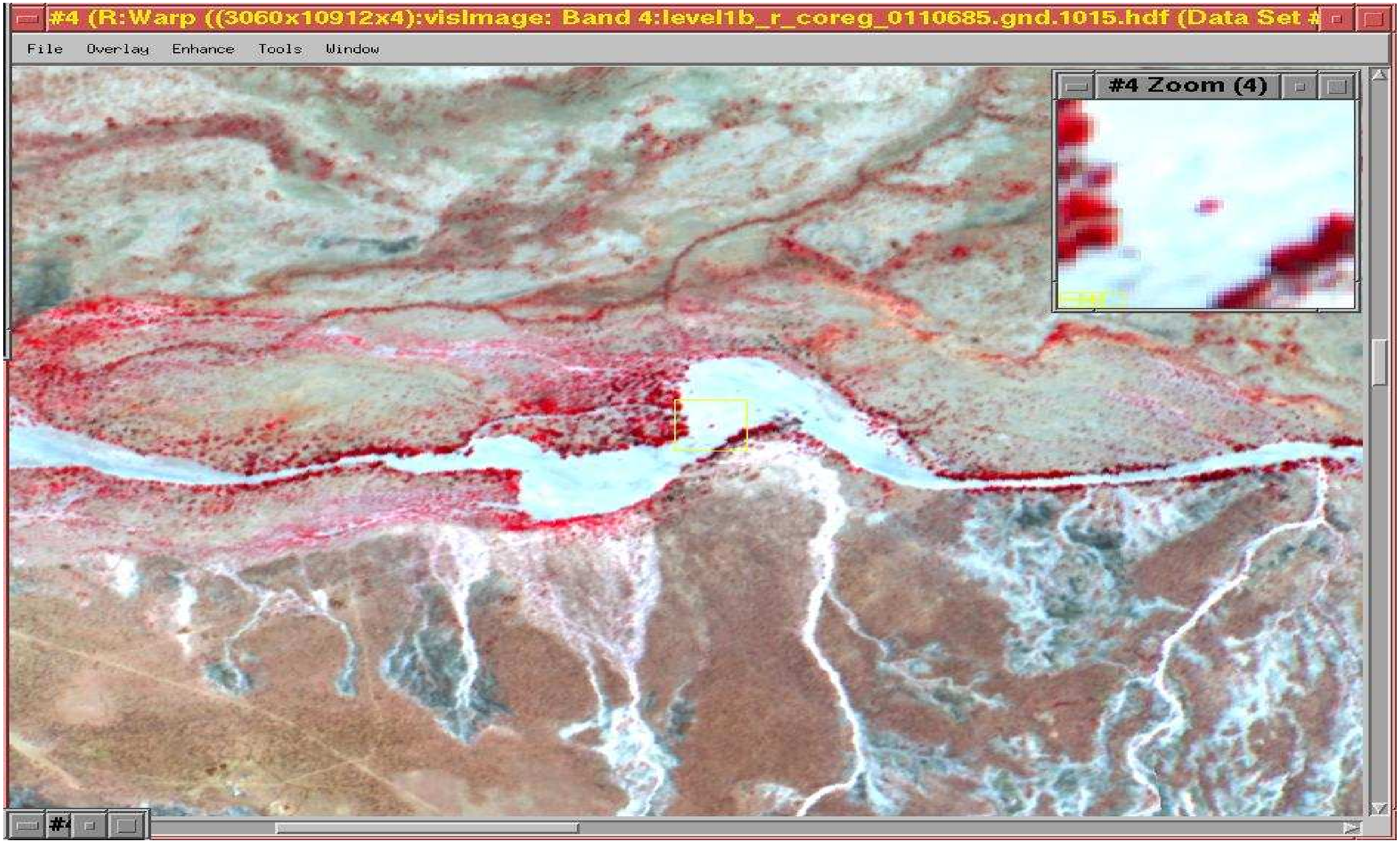

Figure 5.4. Spatial accuracy assessment point image taken to Koobi Fora.

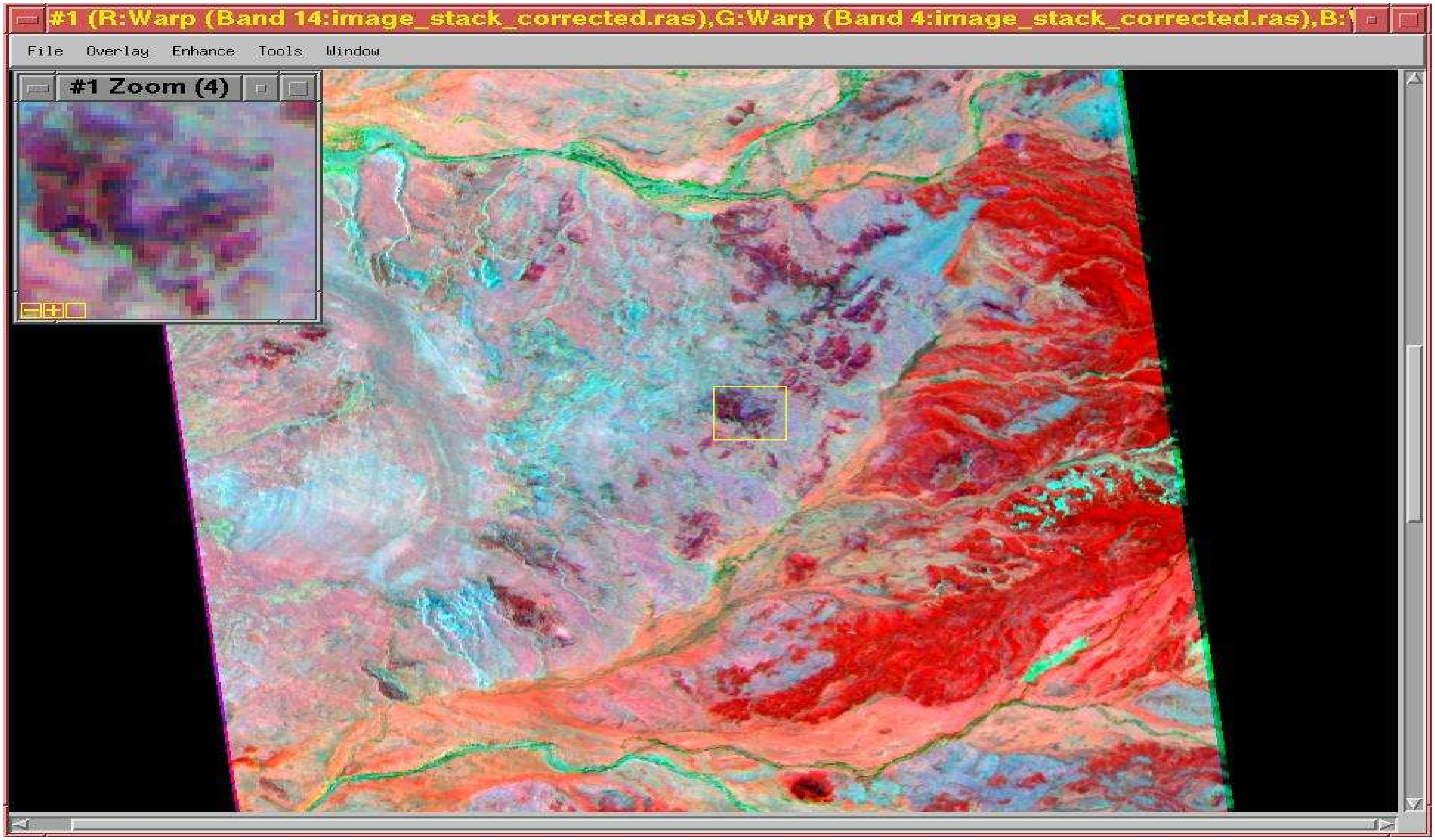

Figure 5.5. Geologic classification point image taken to Koobi Fora.

5.2 Spatial accuracy assessment

The spatial accuracy assessment was conducted in two phases due to logistical limitations and safety issues. The northern portion of the image was visited first, and five spatial accuracy points in an optimum distribution (one in each corner, one in the center) were measured. The northern portion of the field map was then corrected using the data obtained from this initial spatial accuracy survey, and the coordinates of the appropriate classification points were corrected using an affine transformation function. The southern portion of the image was visited during the second half of the field season. After collecting the final spatial accuracy assessment points, the entire map was corrected based on the same affine transformation. All spatial accuracy assessment points were measured using a Trimble Pro-XRS global positioning system receiver. The data from the ProXRS was real time differentially corrected via Afsat, a satellite owned and operated by OmniStar Inc. An average of 60 points was taken as the definitive position of each spatial correction feature. Each of the positions measured was selected on the basis of well defined identity in the MTI imagery. The only well defined features on the image are very large trees (*Acacia sp.* and *Salvadora persica*) that are located in the middle of dry stream beds. Eight trees with an appropriate distribution throughout the image were selected as imagery correction points. As it was impossible to obtain a satellite signal for the ProXRS while directly underneath any of the trees, a compass bearing to the tree and a distance measurement from the center of the tree's canopy was recorded. The range of the horizontal accuracy of the spatial accuracy assessment points was 0.3 to 0.5 meters.

5.3 Geologic classification

Geologic classification points were initially selected based on their spectral signature in the M,D,I band combination. However, once in the field, logistical limitations and safety issues forced a redesign of the geologic classification data collection scheme. Instead of visiting only selected classification points, previously mapped geologic formations, points of opportunity and points of archaeological interest were also visited. Several geologic classification lines were also recorded, in order to trace outcrops over large areas and provide ground-truthing data for a digital elevation model (DEM) of the Karari Escarpment. As equipment needed to be shared with other researchers in the field, some of the geologic classification points were measured using the Trimble ProXRS, and some were measured using a Trimble GeoExplorer II global positioning system receiver. All lines were measured using the Trimble ProXRS. The GeoExplorer II data was not real time differentially corrected and had a spatial accuracy of 0.3-2.8 meters. In addition to the reading from the Trimble ProXRS or the Trimble GeoExplorer II, a second reading was taken at each geologic classification point with a Garmin V handheld global positioning system receiver. The spatial accuracy of the Garmin V was 6 meters. The geologic classification points were an average of 60 points. The lines were taken as one position reading per second.

Post-processing of the spatial and geologic classification data was not possible, the most significant being that there is no global positioning system base station collecting data within 300 kilometers of the Koobi Fora region. Beyond 300 kilometers the usefulness of post-processing data points becomes negligible. As a result, and as an alternative to the original project design, it was decided to take geologic classification points on outcrops that were very large. Only outcrops of single lithologies that were at least 100 meters square were used as geologic classification points.

After geographic positions were recorded on each outcrop selected for classification, a field description of the outcrop or regolith was made. A full description of each sample can be found in Appendix A. A Munsell soil color chart (GretagMacbeth, 2000) was used for the color description of each sample. Grain size, sphericity, and sorting of the surface sediments were measured using the Kent State University grain size card. Vegetation cover type was recorded where applicable. Finally, each geologic classification point sample location was photographed using a Canon PowerShot S45 digital camera.

CHAPTER 6
MTI IMAGE PROCESSING AND MAP CREATION

6.1 MTI imagery catalogue

A catalog of MTI imagery obtained for Koobi Fora is shown in Table 6.1. An overlay map of each image acquired was used to calculate the targeting coordinates for each subsequent image (Pope, 2004, personal communication). Image requests were submitted to and fulfilled by the Sandia National Laboratories MTI ground station. Table 6.1 shows that most of the imagery was collected during 2003. The time separation in imagery collection was due to the acquisition of a number of images with significant cloud cover. Furthermore, requests made by the author to expand this project to include the Karari Escarpment were received favorably by the MTI Users Group, and imagery from this area took additional time to acquire.

6.2 MTI imagery mosaic creation

Creation of the MTI imagery mosaic took two months. All image processing was done in ENVI 4.0 from RSI, Inc. MTI images consist of data from the three sensor chip arrays (SCAs, Figure 2.2). Prior to creating the digital mosaic, each SCA image was evaluated individually for cirrus and other cloud cover, sufficient overlap, and obvious sun look damage in the M, D, and I bands. Since all SCAs of a given image were not always of the highest quality, it became necessary to omit data from some SCAs in favor of higher quality data from others. Figure 6.1 shows a crude mosaic of the SCAs selected for use in the final mosaic. The three bands of each SCA were then manually registered

Image ID	Acquisition Date	UTC Time of Overpass	Look Angle (degrees)	Solar Elevation Angle (degrees)
110662	07/16/02	08:07:42.05	22.4072	65.3811
110685	07/18/02	08:03:21.05	11.2807	64.8023
151176	04/18/03	07:30:20.15	16.5865	64.3069
151184	04/19/03	07:24:59.15	0.3747	63.0107
151793	06/11/03	07:16:21.15	-17.5290	55.8890
151974	06/26/03	07:24:30.15	-34.4966	52.2780
151995	06/27/03	07:18:37.15	-5.6262	55.5242
152118	07/12/03	07:25:08.15	no data	no data
152245	07/29/03	07:17:52.15	7.2126	56.8189
152252	07/30/03	07:11:44.15	3.0450	55.6122
152378	08/14/03	07:15:05.14	9.0795	58.3670
152787	09/15/03	07:05:21.15	1.3958	60.4675
152567	08/30/03	08:07:42.05	7.7889	59.8733
152585	08/31/03	08:03:21.05	-10.6883	58.4798
153633	12/13/03	07:30:20.15	-8.7102	48.0554

Table 6.1. MTI Koobi Fora imagery catalogue.

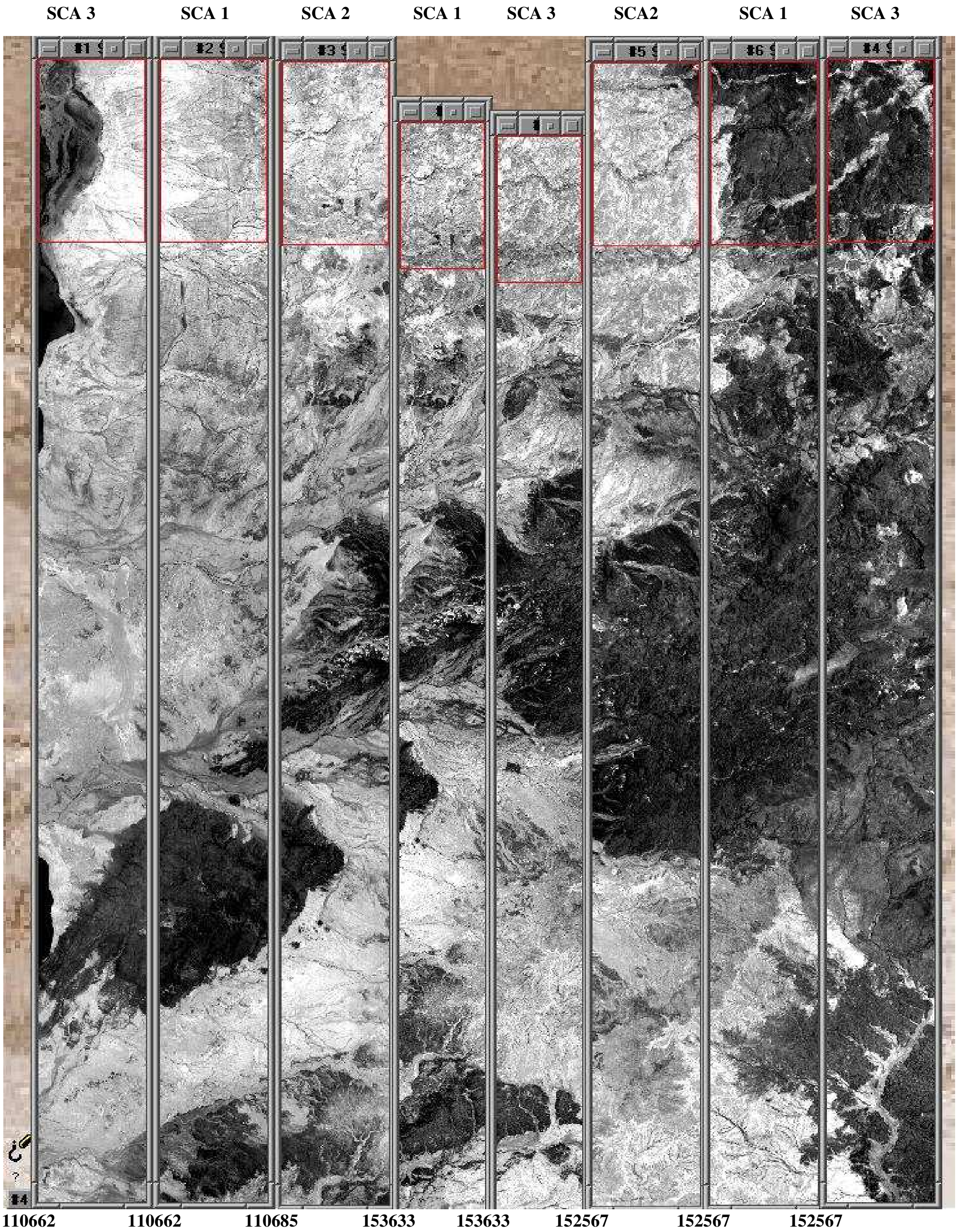

Figure 6.1. Crude beginning mosaic of SCAs selected for the final mosaic.

to one another by choosing distinct points in the overlap regions of the images. Once a homogeneous points file was created, an image stack was made by running a short IDL program.

Because the imagery was acquired over a period of eighteen months, it was necessary to run a manual linear contrast matching transformation on the SCA image stacks that were selected for the mosaic. The outer SCA images were contrast matched to the center SCA, which was image ID 153633, SCA 1. The linear contrast matching transformation did not alter the radiance values for any SCA. However, in spite of the transformation, the final mosaic shows a difference in spectral response between the northeastern and southwestern portions of the mosaic. This is most noticeable in the very center of the mosaic.

The final step in the mosaicking process was to register the individual SCAs to a georeferenced image from NASA's global orthorectified Landsat data set (Tucker et al., 2004). The contrast matched and georeferenced data from the different SCAs was then mosaicked together using ENVI's mosaic tool. The final product is shown in Figure 6.2. Figure 6.3 shows a map of all the spatial accuracy assessment points used in the study, and Figure 6.4 shows a map of all of the geologic classification points used in the study. Figure 6.5 shows an overlay of Bowen's 1974 geologic map on the multispectral geologic map. The closeups of the Ileret and Karari Escarpment show a relatively good fit between the MTI imagery and the gross divisions of the Koobi Fora Formation as defined by Bowen. This demonstrates that it is possible to differentiate surface lithologies

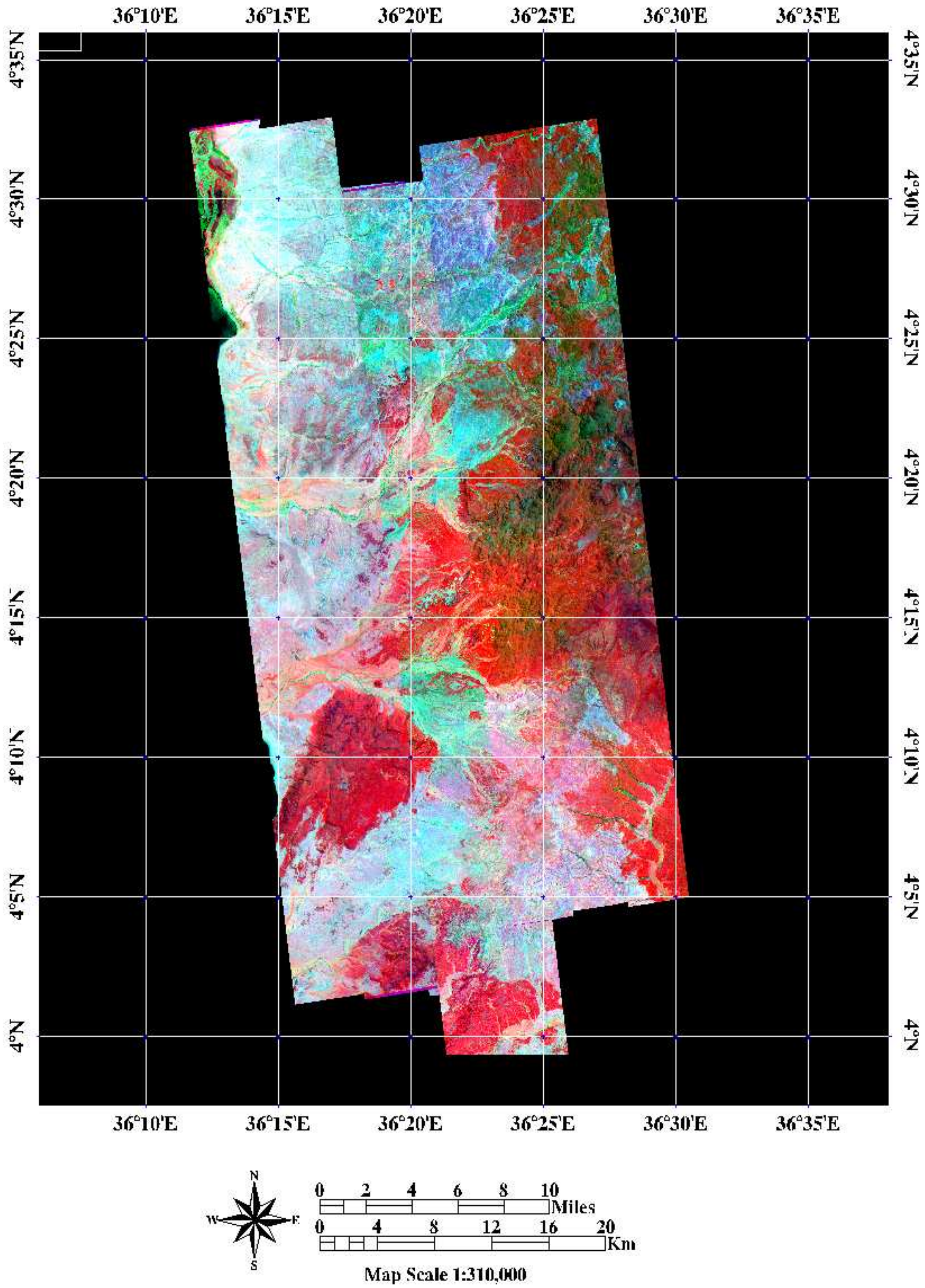

Figure 6.2. MTI map of Koobi Fora.

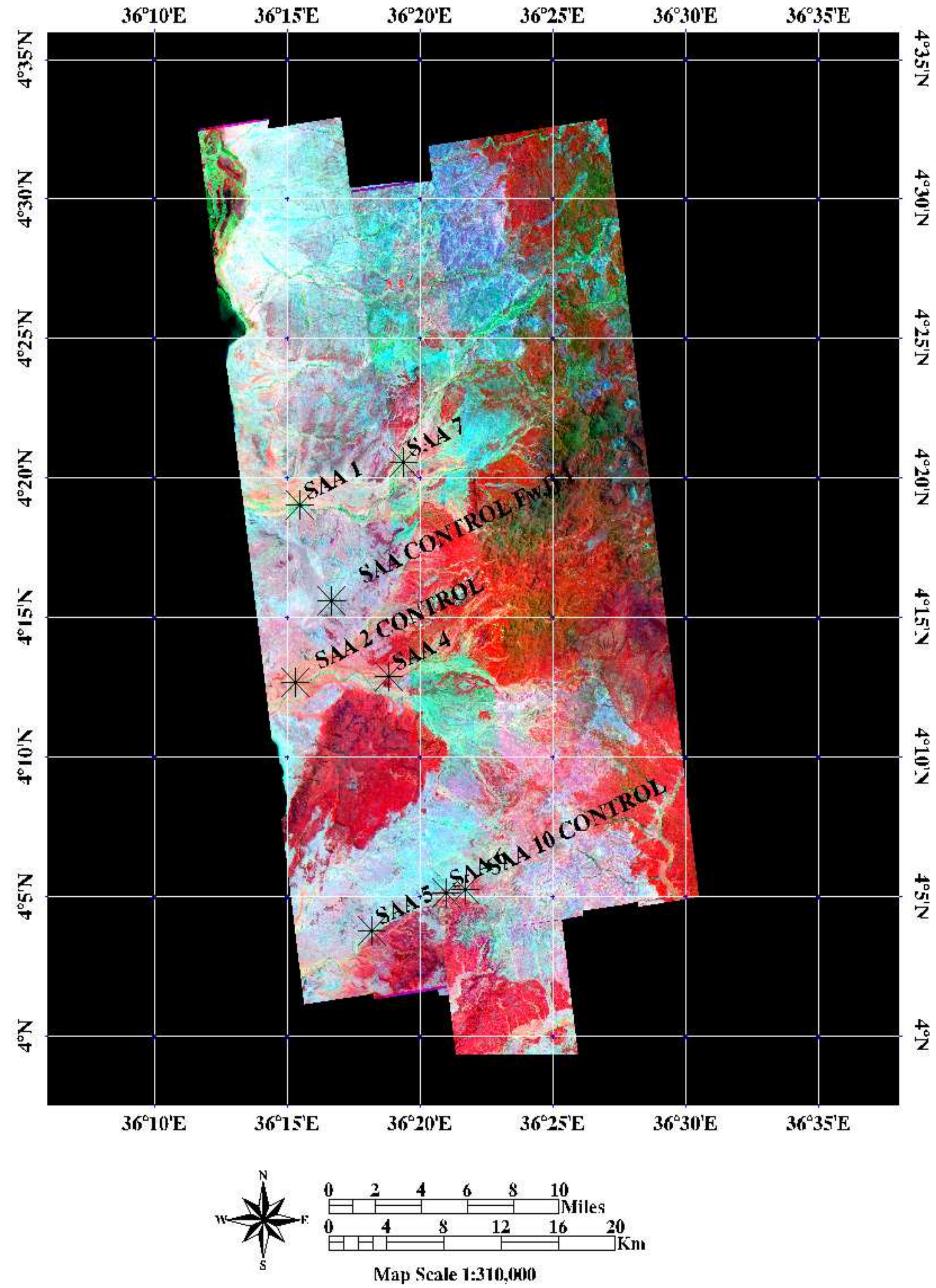

Figure 6.3. Location map of all spatial accuracy assessment points used in this study.

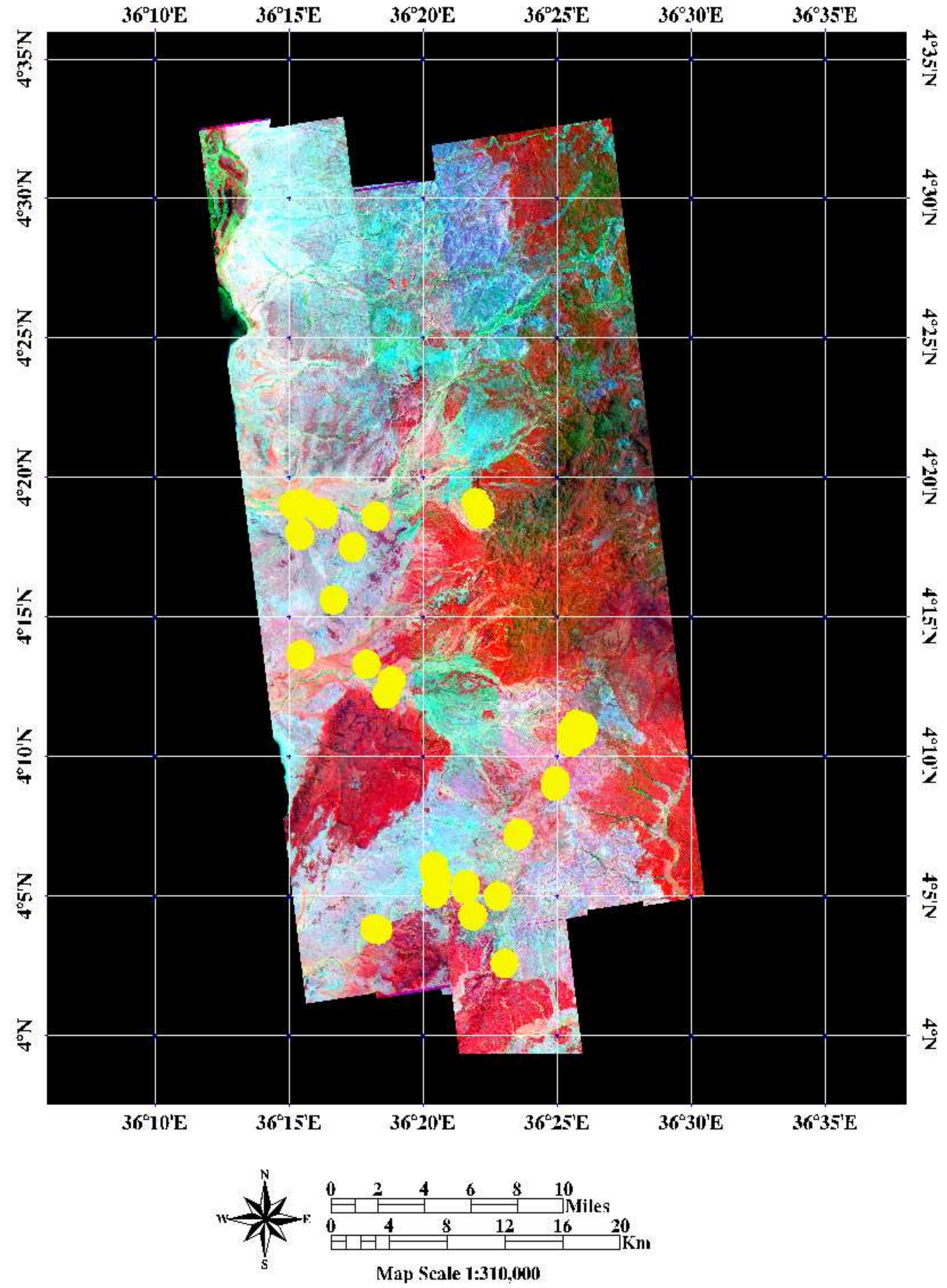

Figure 6.4. Location map of all geologic classification points used in this study.

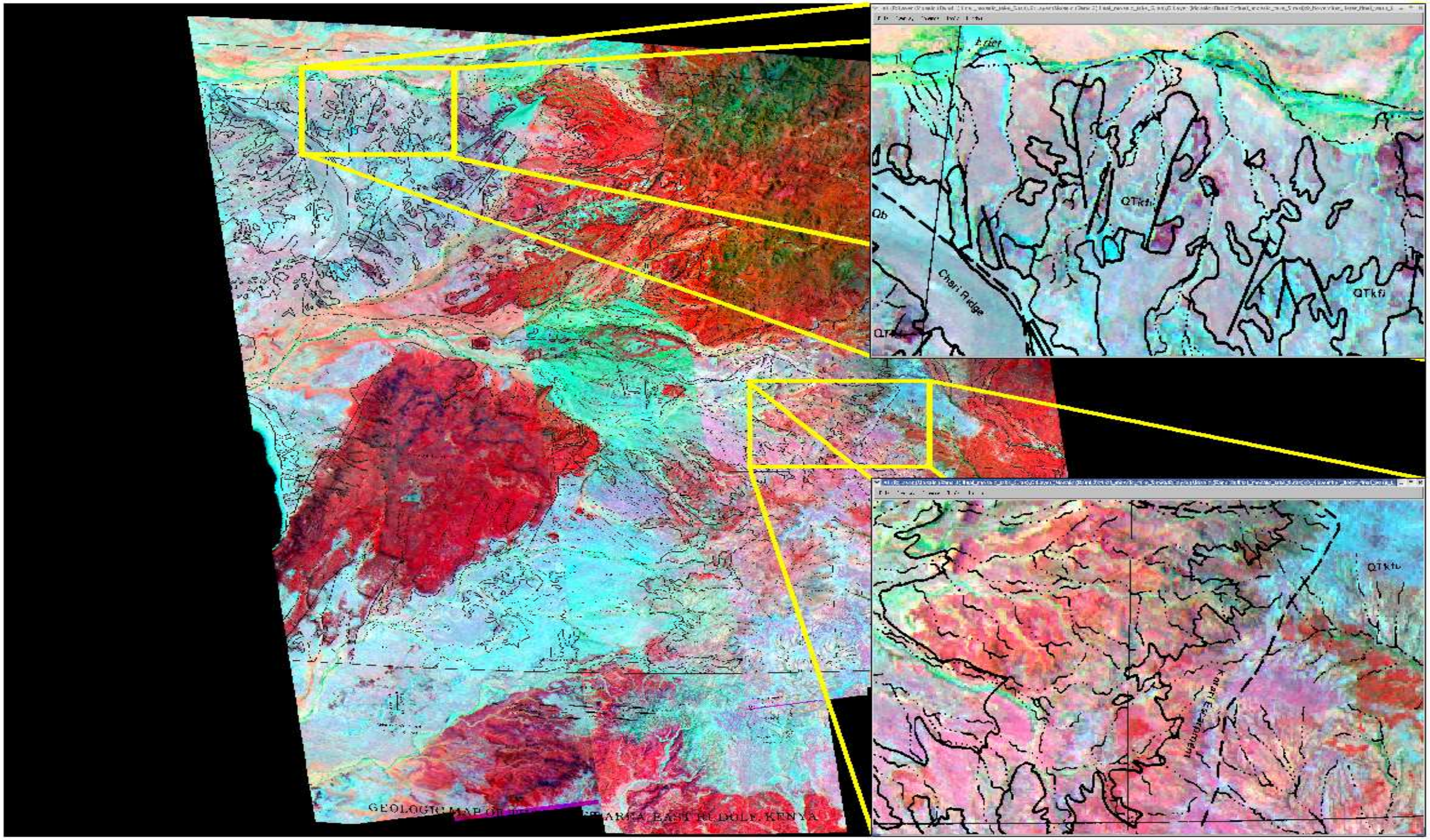

Figure 6.5. An overlay of Bowen's 1974 map on the MTI imagery.

lithologies based solely on spectral response. Though the lithostratigraphic nomenclature for the Koobi Fora Formation has changed since Bowen's map was created (Brown and Feibel, 1986), the lithologies on the ground have not. In fact, the diversity of response within the closeups in Figure 6.5 shows that the MTI image offers greater surface geologic detail than Bowen's map.

Figure 6.6 shows a 3-dimensional map of the Karari Escarpment. It consists of the MTI mosaic, a DEM data set from the NASA SRTM project (NASA JPL, 2003), and overlays of geologic classification points and DEM ground-truthing lines taken during the field season. Lines walked along the KBS Tuff and Chari Tuff show that the tuffs can be defined in the MTI mosaic. The color of tuff in the image varies from bright cyan to dark blue. It is important to note that the dry stream and river beds are a similar color in the mosaic, but they are bounded by green areas of vegetation. A stream channel can be seen running through the left side of this 3-dimensional map. Thus, adding the DEM to the MTI mosaic creates a map product that displays the geologic information within its spatial context. This may make the MTI mosaic more valuable when attempting to use it in the field to identify certain lithologies.

6.3 MTI mosaic spatial error analysis

Once the MTI mosaic was completed, error analysis of the final product was conducted. The Landsat to MTI relative georeferencing error was computed by comparing points on the georeferenced MTI imagery with their corresponding coordinates on the Landsat imagery. Table 6.2 shows the results of this analysis, where the final MTI mosaic is calculated to have a relative spatial accuracy of 12 meters +/- 32 meters in latitude and 2 meters +/- 43 meters in longitude. The absolute spatial accuracy of the map is 73 meters.

MTI X	MTI Y	Landsat X	Landsat Y	difference in X, pixels	difference in Y, pixels
872.43	1079.86	871.50	1081.50	0.93	-1.64
1757.00	787.71	1759.00	789.75	-2	-2.04
1359.75	1789.00	1357.50	1789.50	2.25	-0.50
2123.00	2743.00	2121.50	2741.00	1.50	2.00
1147.50	2983.50	1147.00	2980.75	0.50	2.75

RELATIVE ACCURACY

mean difference in x	mean difference in y
0.6 pixels	0.1 pixels
12.7 meters	2.2 meters
0.0001 degrees	0.00002 degrees
standard deviation of x	**standard deviation of y**
1.6 pixels	2.1 pixels
32.2 meters	43.1 meters
0.00001 degrees	0.00001 degrees

ABSOLUTE ACCURACY

MTI		Landsat	
variance in x, meters	1024	absolute accuracy, meters	50
variance in y, meters	1849		
total variance	2873	total variance	2500

total variance, MTI and Landsat	5373 meters
absolute accuracy, MTI mosaic	73.3 meters

Table 6.2. Relative and absolute spatial accuracy assessment of MTI data as compared with Landsat Global Orthorectified data (Tucker et al., 2004).

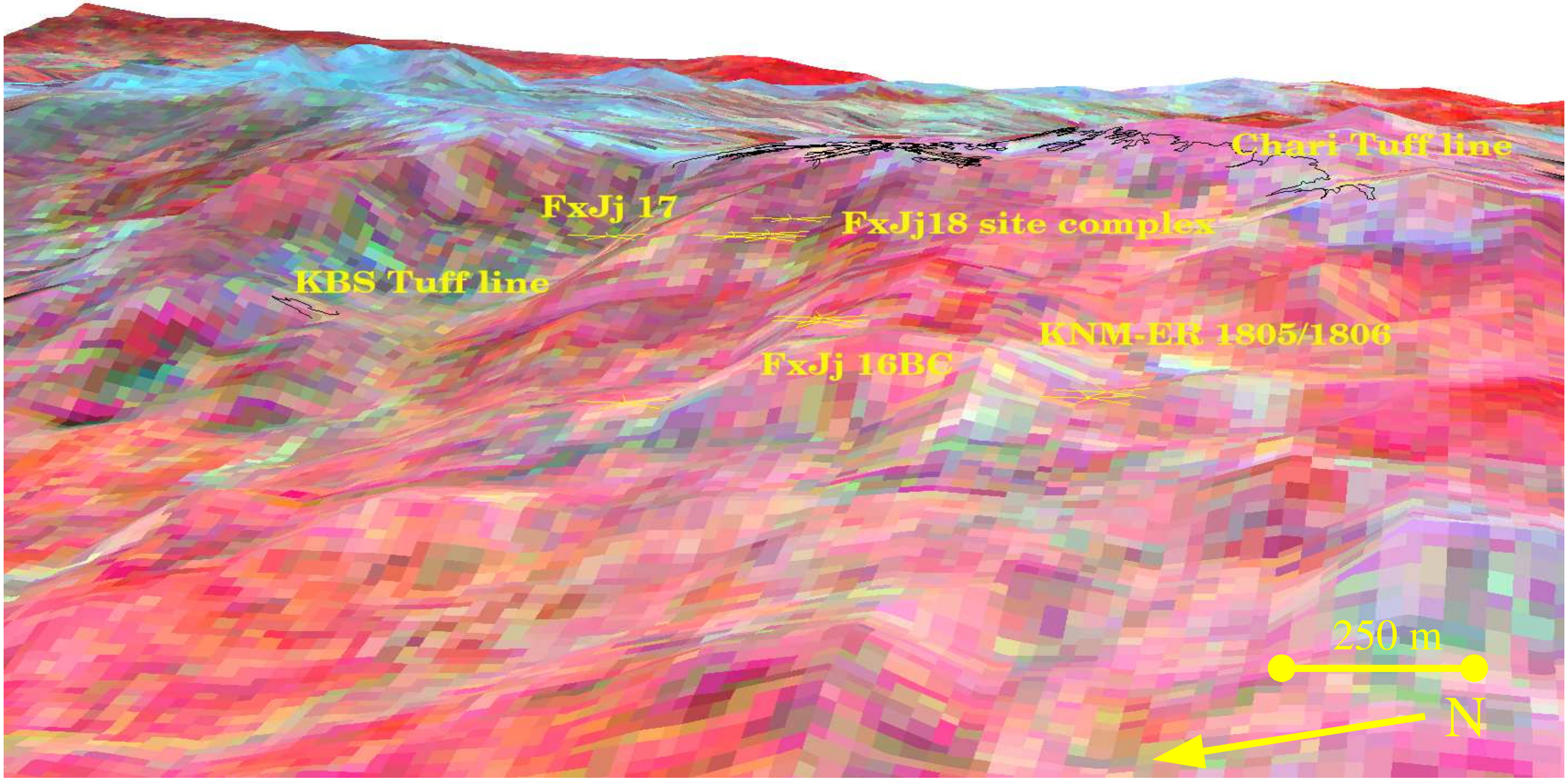

Figure 6.6. 3-dimensional map of the Karari Escarpment.

CHAPTER 7
GEOLOGIC CLASSIFICATION

7.1 MTI image geologic classification mapping

By applying the linear spectral unmixing algorithm to the MTI mosaic, geologic classification maps were created for two sets of three and two sets of four combinations of five geologic classes. These are percent cover maps for geologic classes tuff, carbonate, basalt, alluvium, and for the vegetation class.

It was anticipated that the different tuffs in the Koobi Fora Formation would have similar spectral signatures, and therefore geologic classification points from outcrops of the KBS, Okote, and Chari tuffs were used as regions of interest (ROIs) for a single tuff class. The alluvium class consisted of all three types of alluvium, and every effort was made to exclude vegetation from this class. Carbonate was selected as a geologic class because of its prevalence and diversity of forms throughout the study area and its anticipated spectral difference from the other classes. The basalt geologic class was selected and defined for the same reasons.

The unmixing maps were constructed by selecting areas of pure outcrop within the georeferenced MTI mosaic in order to create the ROIs. The size of the ROIs mirrors that of the outcrops that were described in the field or located within an outcrop on a map overlay. The 1978 Iowa State maps were used in this process, and overlays were created by georeferencing them to the MTI mosaic (Figures 7.1-7.4). Twenty ROIs consisting of a minimum of thirty pure pixels were defined for each geologic class. Ten ROIs were chosen randomly from this larger group and used to generate pure spectra with which to train the IDL unmixing program. A graph of the pure spectra is shown in Figure 7.5 The normalized pure spectra graph shown in Figure 7.6 illustrates more clearly the differences between the pure spectra of the different geologic classes.

7.2 Pure spectra

The pure spectra values were obtained by gathering the statistics of each training ROI and calculating the mean radiance value for each mosaic band. The ten ROIs not used for training of the image were used for accuracy assessment of the percent cover maps. Each ROI was assigned to the geologic class with the highest mean value in the accuracy statistics.

The graphs of the pure spectra, shown in Figures 7.5 and 7.6, illustrate the mean radiance value of each lithology in each MTI band within the Koobi Fora mosaic. Tuff and carbonate have similar pure spectra, with tuff displaying higher radiance values in each band. The pure spectrum for basalt shows that it has the highest radiance value of any geologic class in band 1 and no radiance value in bands 2 and 3. Alluvium shows the opposite response in bands 2 and 3, where it has the highest radiance value of any class; its radiance in band 1, however, is the second lowest of all classes. The pure spectrum for vegetation shows almost no radiance value in band 1, the second highest radiance of all classes in band 2, and relatively low radiance in band 3.

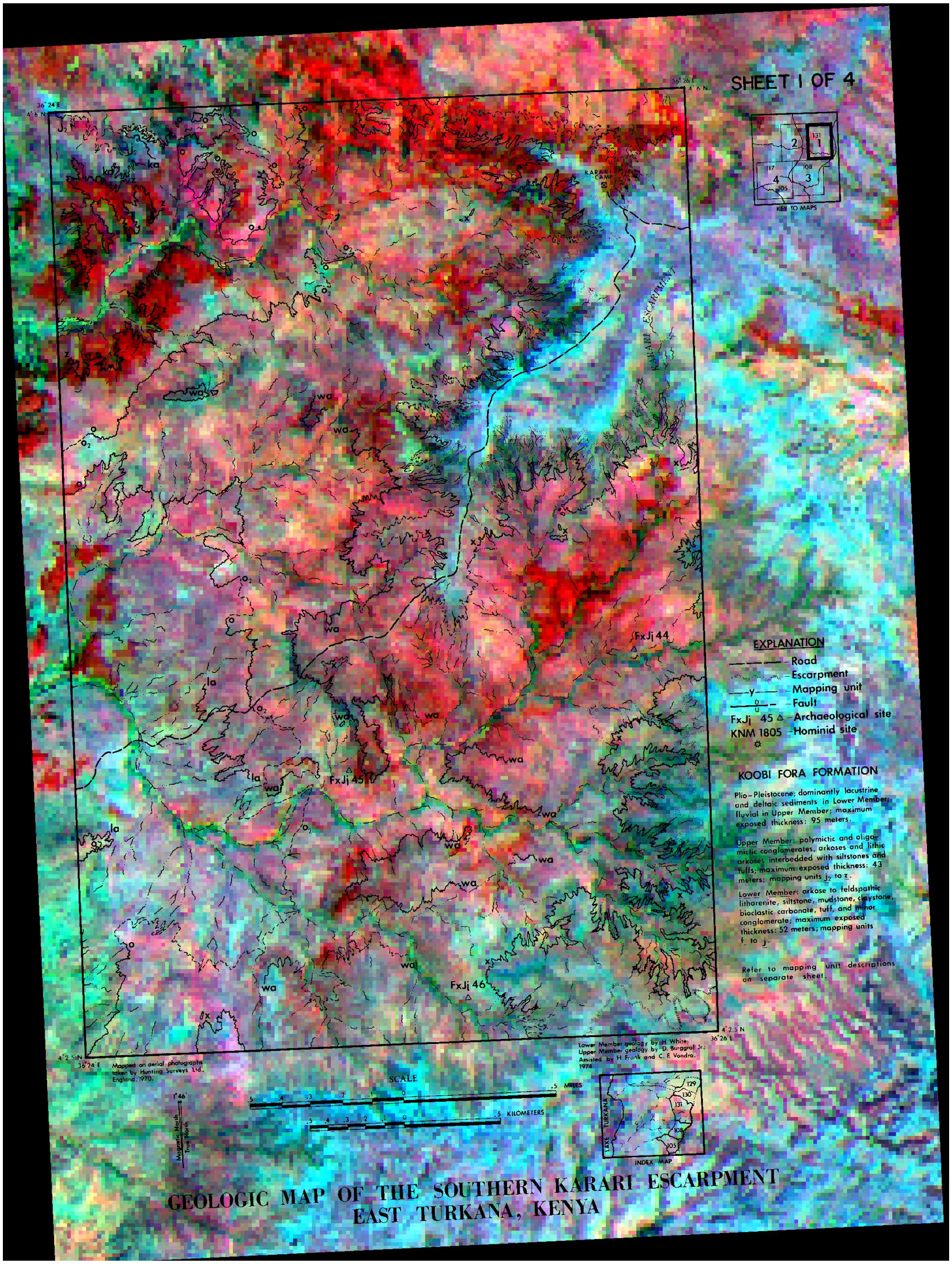

Figure 7.1. Overlay of Iowa State Karari Escarpment geologic map 1 on the MTI imagery.

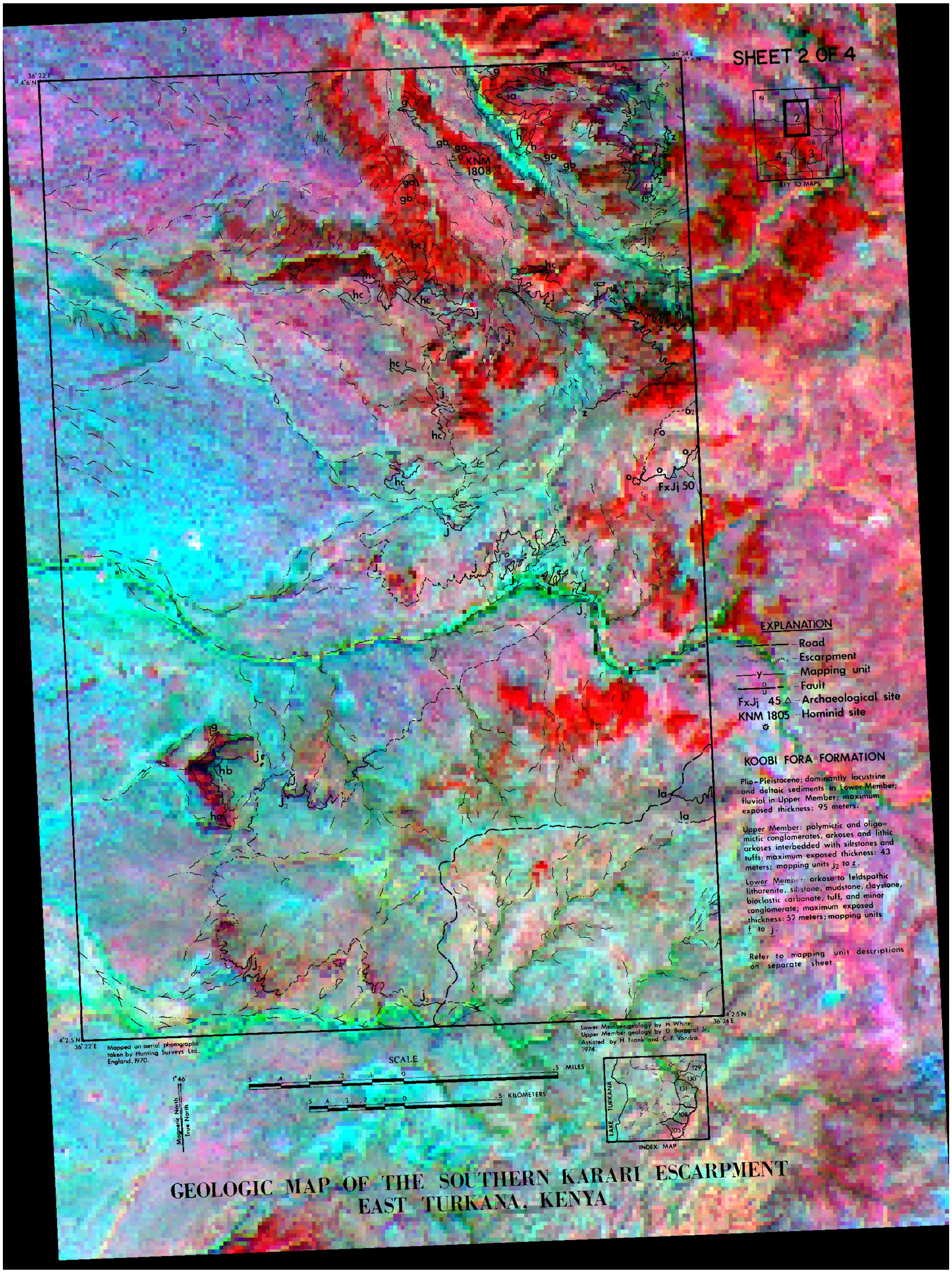

Figure 7.2. Overlay of Iowa State Karari Escarpment geologic map 2 on the MTI imagery.

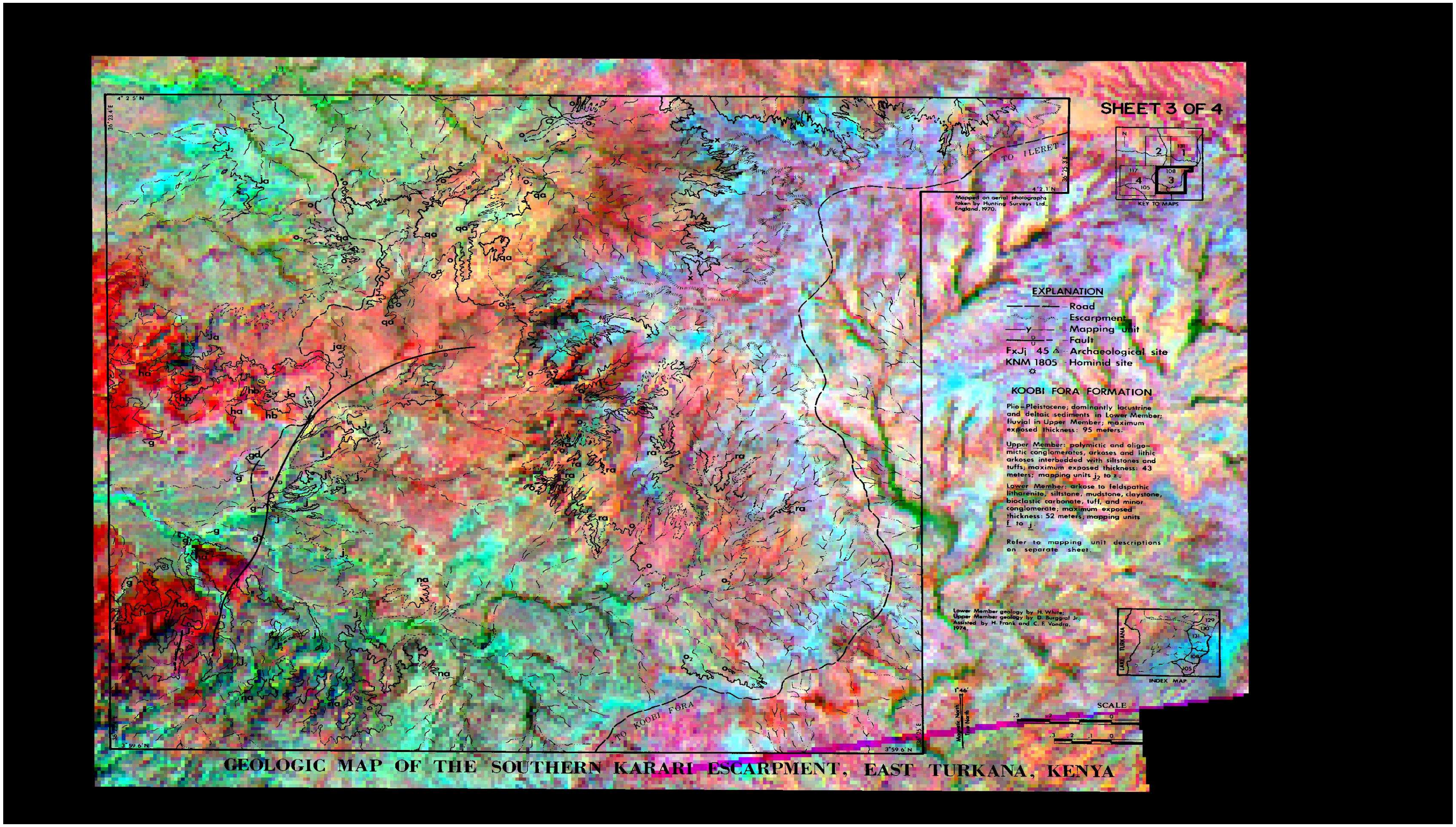

Figure 7.3. Overlay of Iowa State Karari Escarpment geologic map 3 on the MTI imagery.

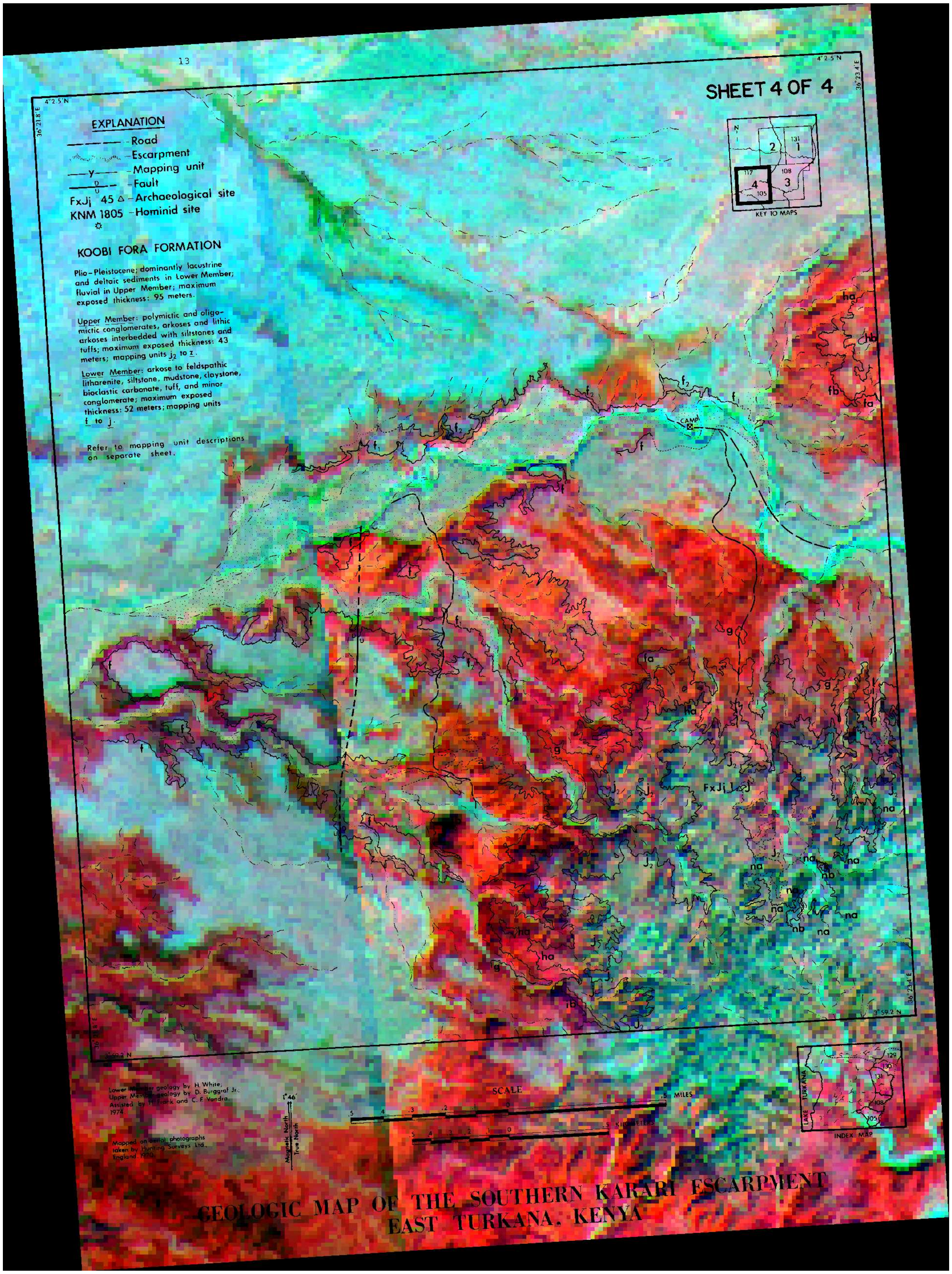

Figure 7.4. Overlay of Iowa State Karari Escarpment geologic map 4 on the MTI imagery.

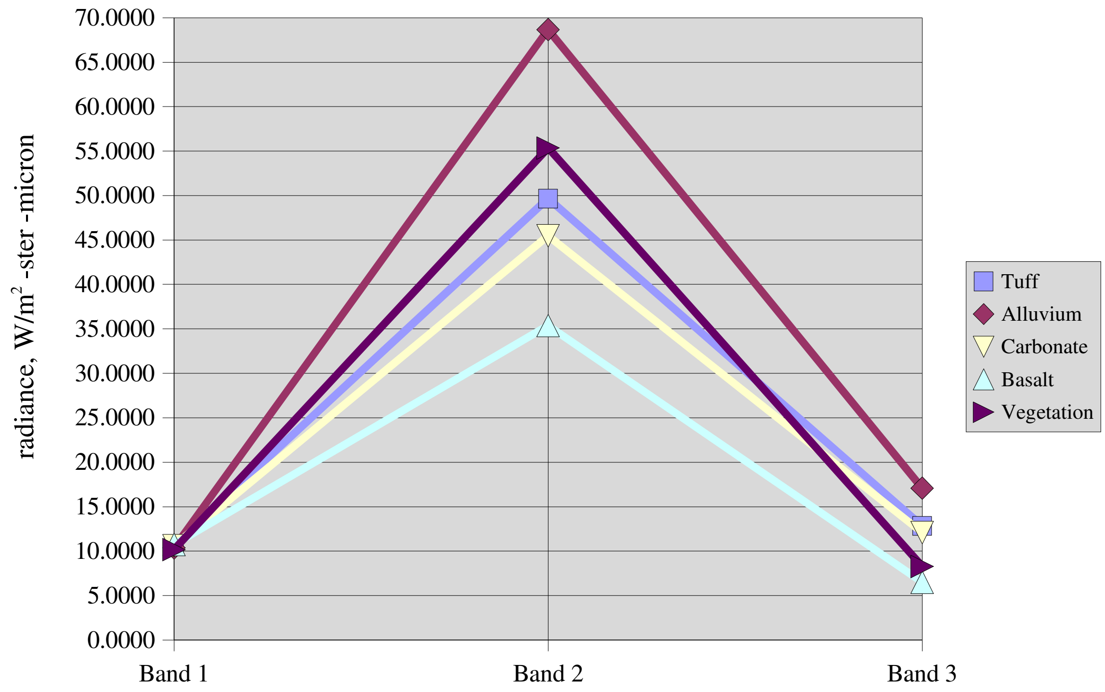

Figure 7.5. Graph of pure spectra derived from training ROIs.

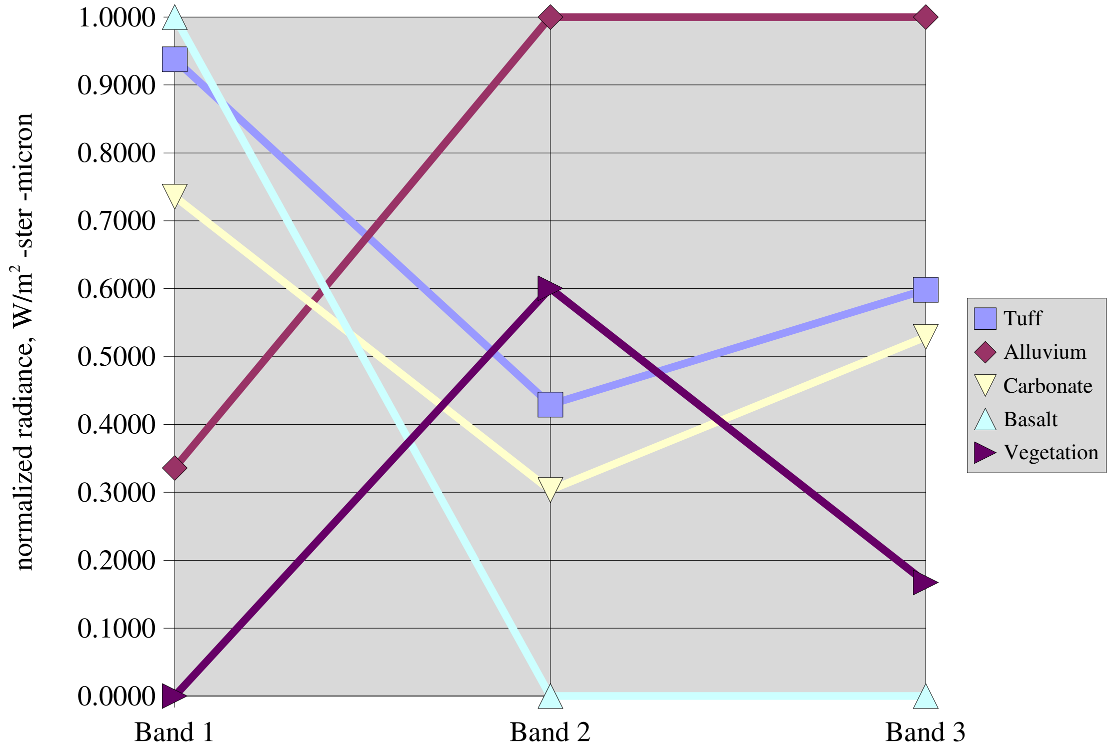

Figure 7.6. Normalized pure spectra.

7.2.1 Pure spectra combinations used in classification mapping

Four different unmixing runs were completed in order to explore the quantitative and qualitative accuracy of results arising from different pure spectra combinations. These combinations are summarized in Table 7.1.

	TUFF	ALLUVIUM	CARBONATE	BASALT	VEGETATION
RUN 1	X			X	X
RUN 2	X		X		X
RUN 3	X		X	X	X
RUN 4	X	X	X	X	

Table 7.1. Unmixing combinations used for creation of percent cover maps.

The first and second runs were designed to quantify the amount of differentiation possible between the carbonate and basalt geologic classes. The third run was created to more accurately represent ground conditions, and to see if the alluvium ROIs might contain some vegetation. The final run was designed to consist of entirely geologic material.

7.3 Results- run 1

Each of the four runs produced unique results. The combination of pure spectra that worked best with the unmixing algorithm was the basalt, tuff, and vegetation combination used in run 1. The error matrix for this run is shown in Table 7.2. The graph of the normalized pure spectra (Figure 7.6) shows that the pure spectra for basalt, tuff, and vegetation are very different from one another. These differences were likely a factor in the relative success of this run. As the author doubted the 100% accuracy results of run 1, this particular combination of ground cover elements was analyzed with the unmixing algorithm several times using different ROI combinations. The end result was always 100% accuracy in geologic and vegetation class definition.

	tuff	basalt	vegetation		
tuff	10	0	0	10	
basalt	0	10	0	10	
vegetation	0	0	10	10	
	10	10	10	30	

	producer's accuracy %		user's accuracy %		overall accuracy %
tuff	100	tuff	100		100
basalt	100	basalt	100		
vegetation	100	vegetation	100		

Table 7.2. Error matrix for run 1.

The percent tuff cover map, shown in Figure 7.7, illustrates that the algorithm classified quartz and tuff coverage. For example, Figure 7.8 is an overlay of one of the Iowa State maps on the percent tuff cover map for run 1. It shows that the Chari Tuff outcrops along the Karari Escarpment were well-defined by the algorithm. However, beach sands west of Ileret and aeolian dunes south of the Kokoi Horst were also classified as tuff in this percent cover map. The spatial pattern of the tuff outcrops is quite distinct from that of other lithologies within the Koobi Fora Formation, and it is this spatial separation that may make the map valuable in the field definition of tuff outcrops in spite of the misclassification problem.

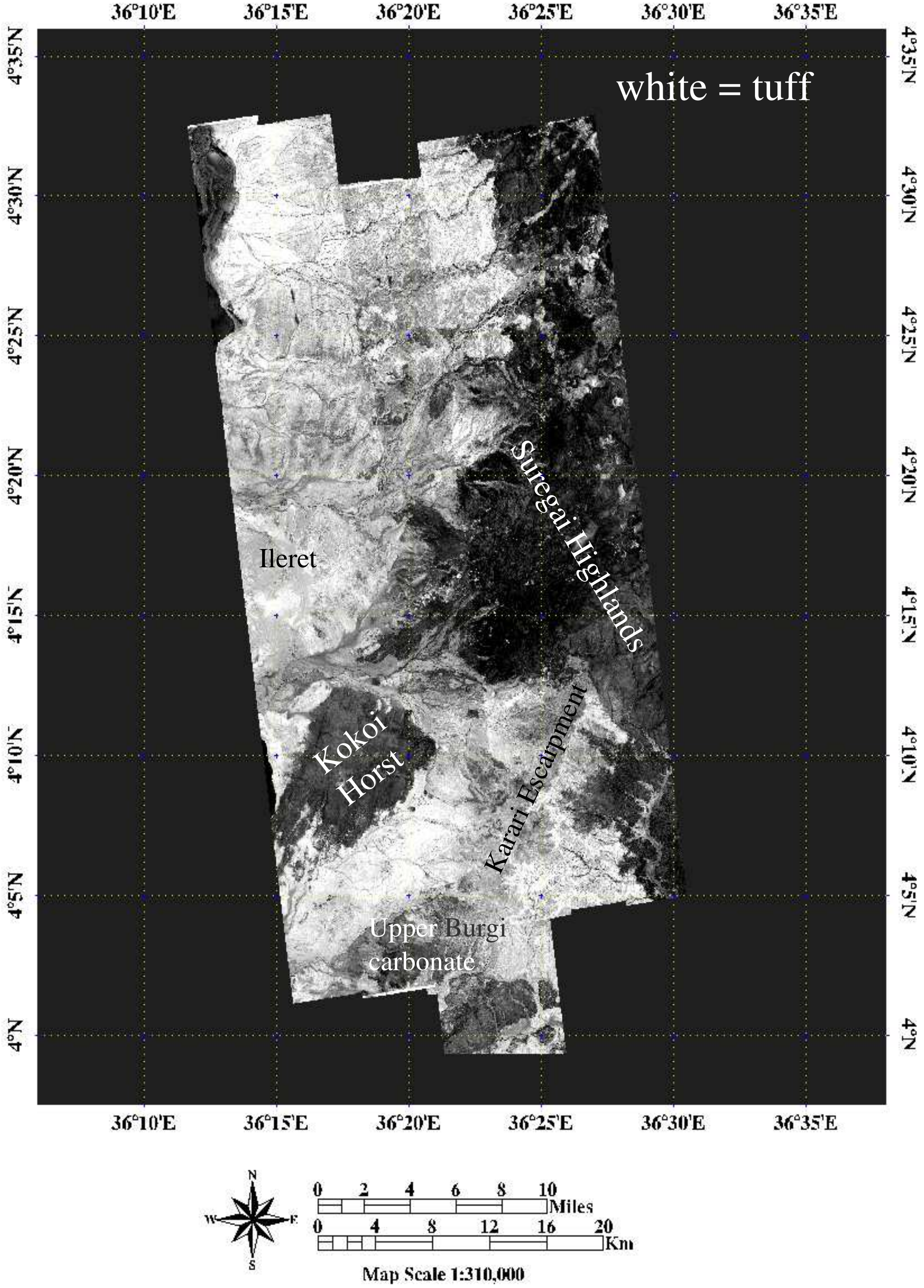

Figure 7.7. Run 1 (tuff/basalt/vegetation) percent tuff map, with major geographic features labeled.

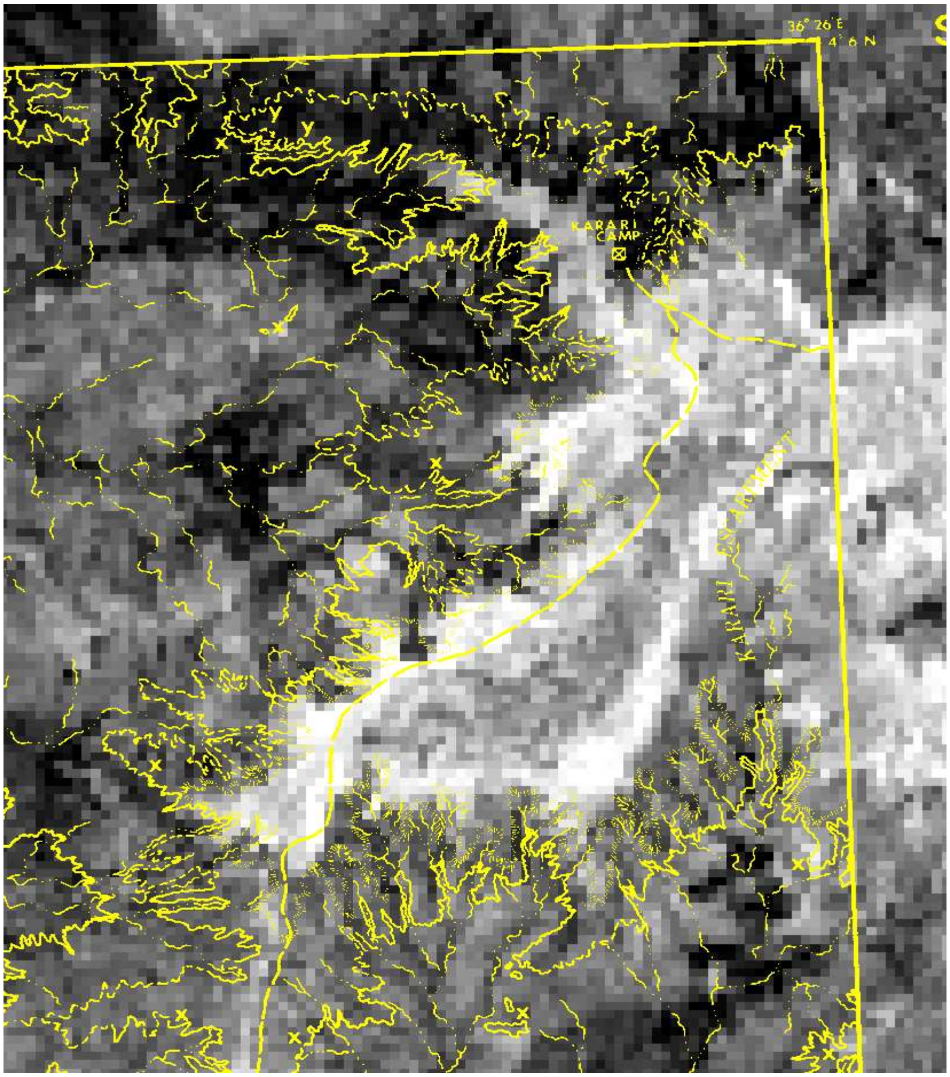

Figure 7.8. An overlay of Burggraf's 1976 southern Karari Escarpment map (scale = 1:6,000) on the percent tuff map. The Chari Tuff is bright white in this image.

The percent basalt cover map for run 1 (Figure 7.9) was accurate in its definition of the flood basalts of the Suregai Highlands and the Kokoi Horst. The Upper Burgi molluscan packstone in the southern portion of the map was misclassified as basalt, however. This is because of the black weathering rind found on the packstone outcrops, which made their response in the thermal infrared portion of the electromagnetic spectrum similar to that of basalt.

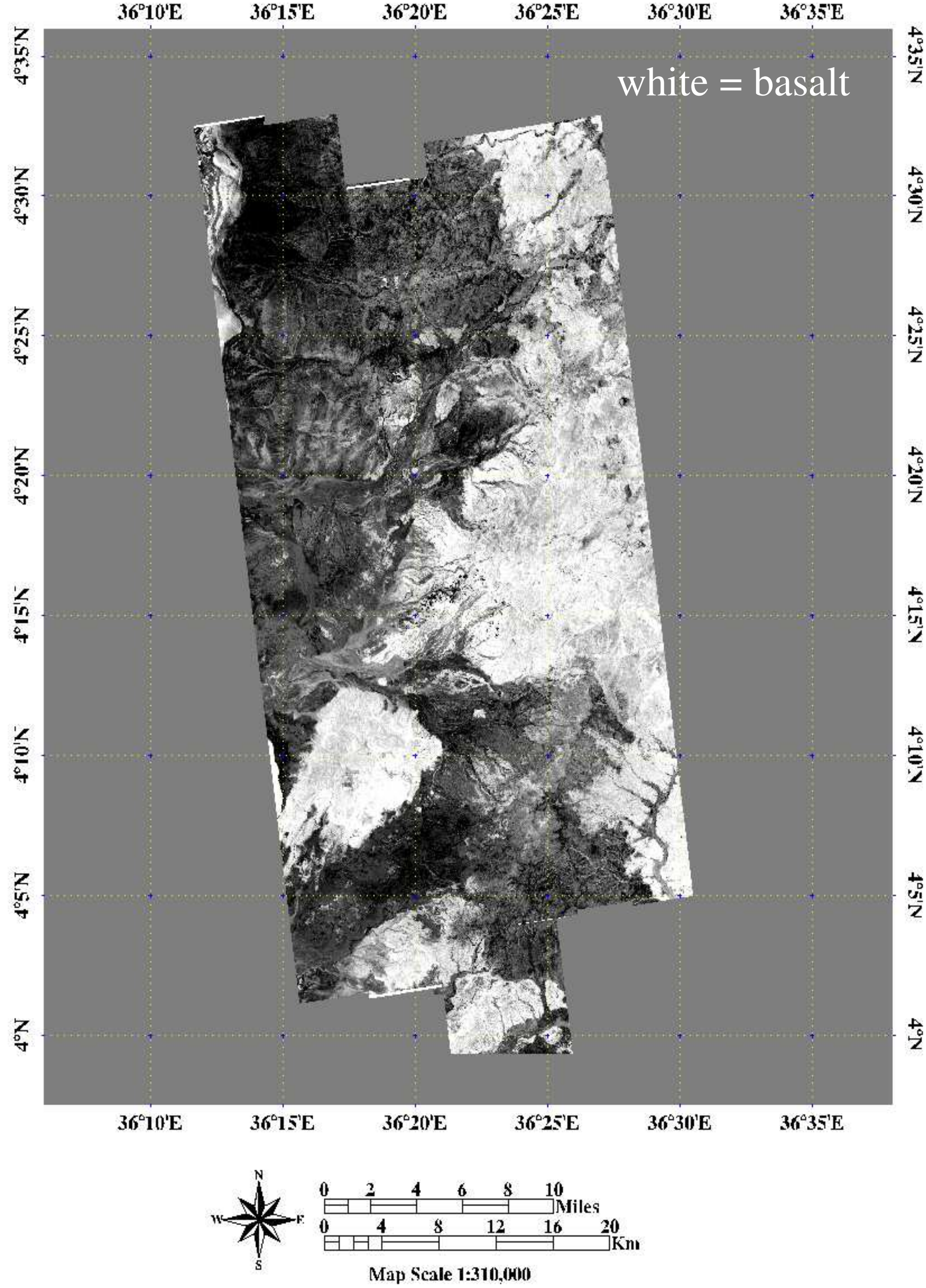

Figure 7.9. Run 1 (tuff/basalt/vegetation) percent basalt map.

The percent vegetation cover map for run 1 is shown in Figure 7.10. It accurately defined the concentration of vegetation along the dry stream beds and along the lake shore at Koobi Fora. The bright vegetation response in the center SCA and the northeastern portions of the map did not indicate an abundance of vegetation, but was due rather to the contrast matching problem in the final mosaic. The RMS error map (Figure 7.11) shows that the algorithm's error was highest in these areas.

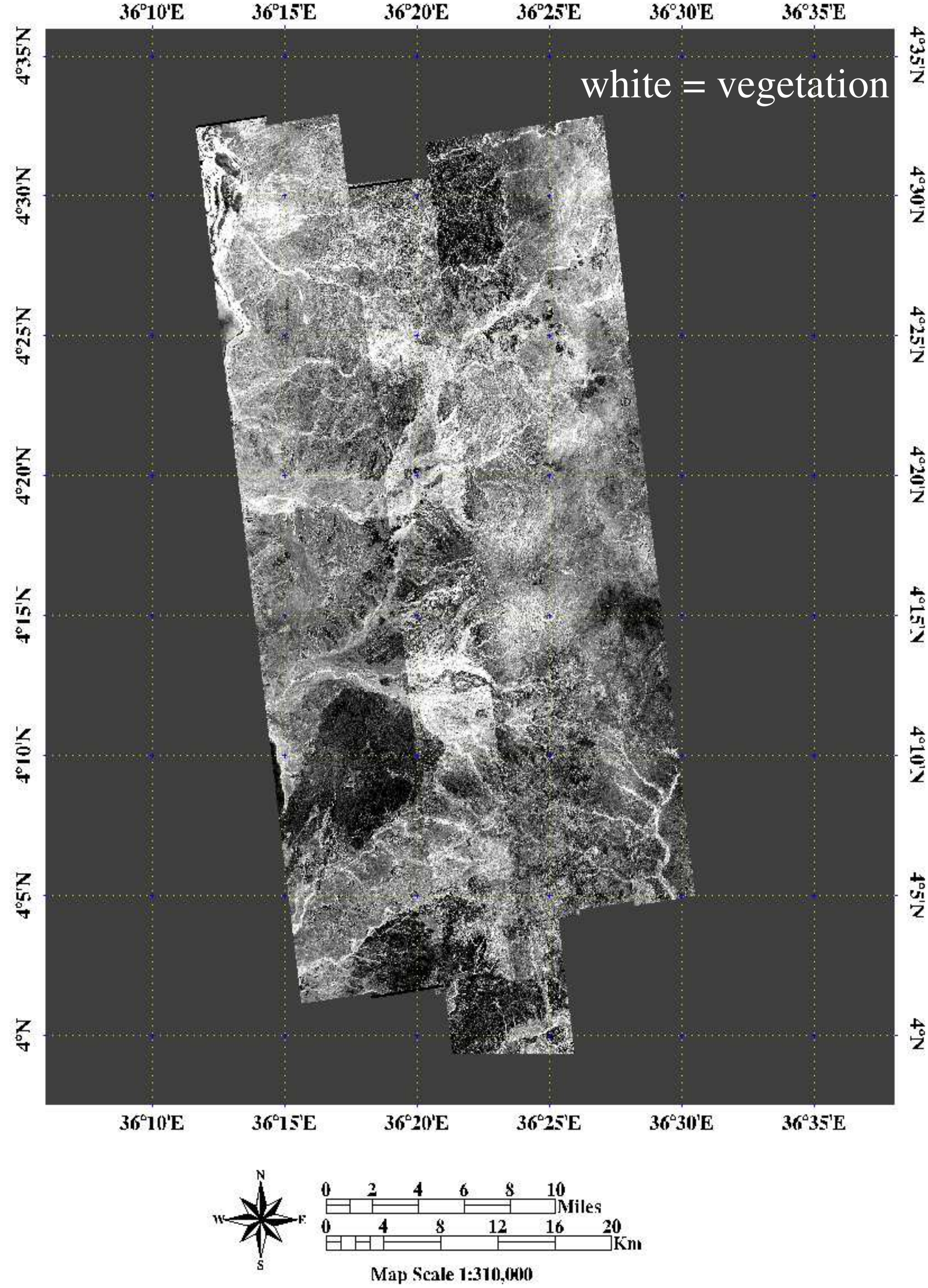

Figure 7.10. Run 1 (tuff/basalt/vegetation) percent vegetation map.

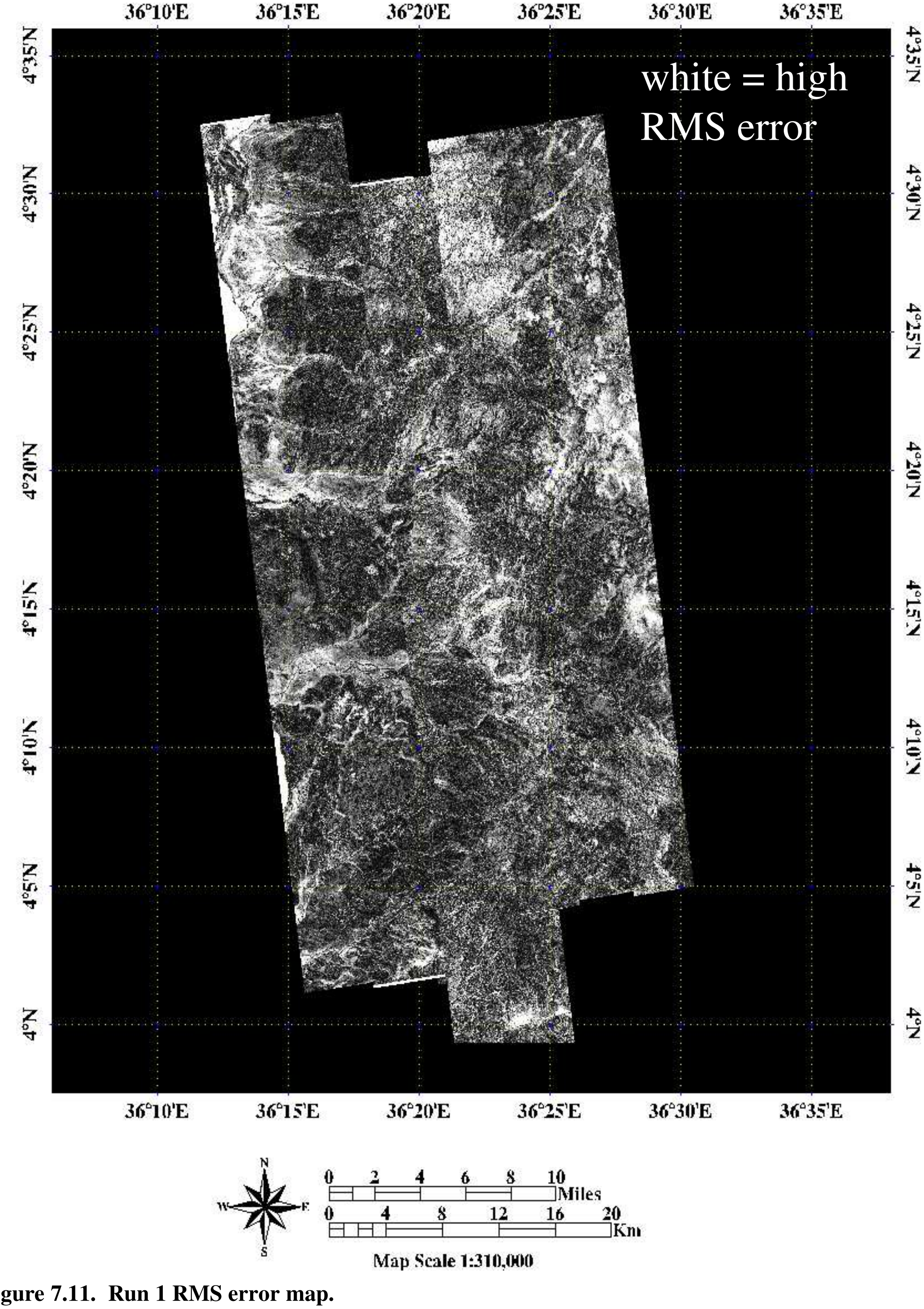

Figure 7.11. Run 1 RMS error map.

7.4 Results- run 2

The introduction of biogenic carbonate into the unmixing equation produced quite different results. The graph of the normalized pure spectra (Figure 7.6) shows that tuff and carbonate have the most similar pure spectra of all of the classes. Both tuff and carbonate have their highest radiance response in band 14, a lower response in band 4, and a high response in band 10.

	tuff	carbonate	vegetation		
tuff	9	2	8	19	
carbonate	1	8	1	10	
vegetation	0	0	1	1	
	10	10	10	30	

	producer's accuracy %		user's accuracy %		overall accuracy %
tuff	90	tuff	47.37		60
carbonate	80	carbonate	80		
vegetation	10	vegetation	100		

Table 7.3. Error matrix for run 2.

The error matrix for run 2 is shown in Table 7.3. Vegetation detection in run 2 had a producer's accuracy of only 10%, and tuff had a user's accuracy of less than 50%. The confusion in these two classes drives the overall accuracy of the unmixing maps down to 60 percent. In sum, this combination of pure spectra did not define the geologic classes well enough for the end products to be useful in the field.

The percent tuff cover map for run 2 is shown in Figure 7.12. In spite of its low user accuracy in the error matrix (Table 7.3), tuff definition was qualitatively better in some areas of this map than the tuff map generated in run 1. For example, Figure 7.13 compares the definition of the KBS Tuff at archaeological site FxJj10. The top image

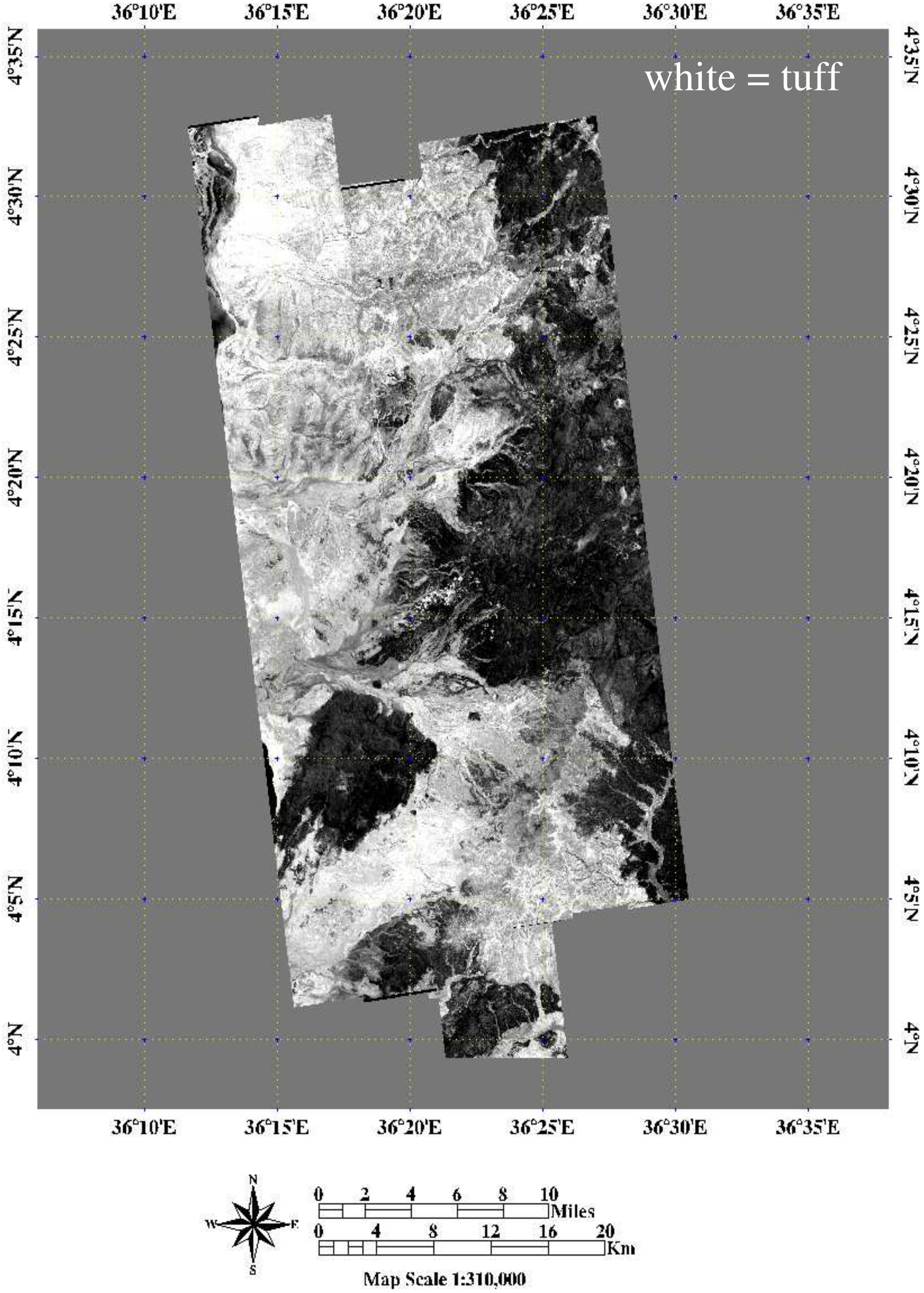

Figure 7.12. Run 2 (tuff/carbonate/vegetation) percent tuff map.

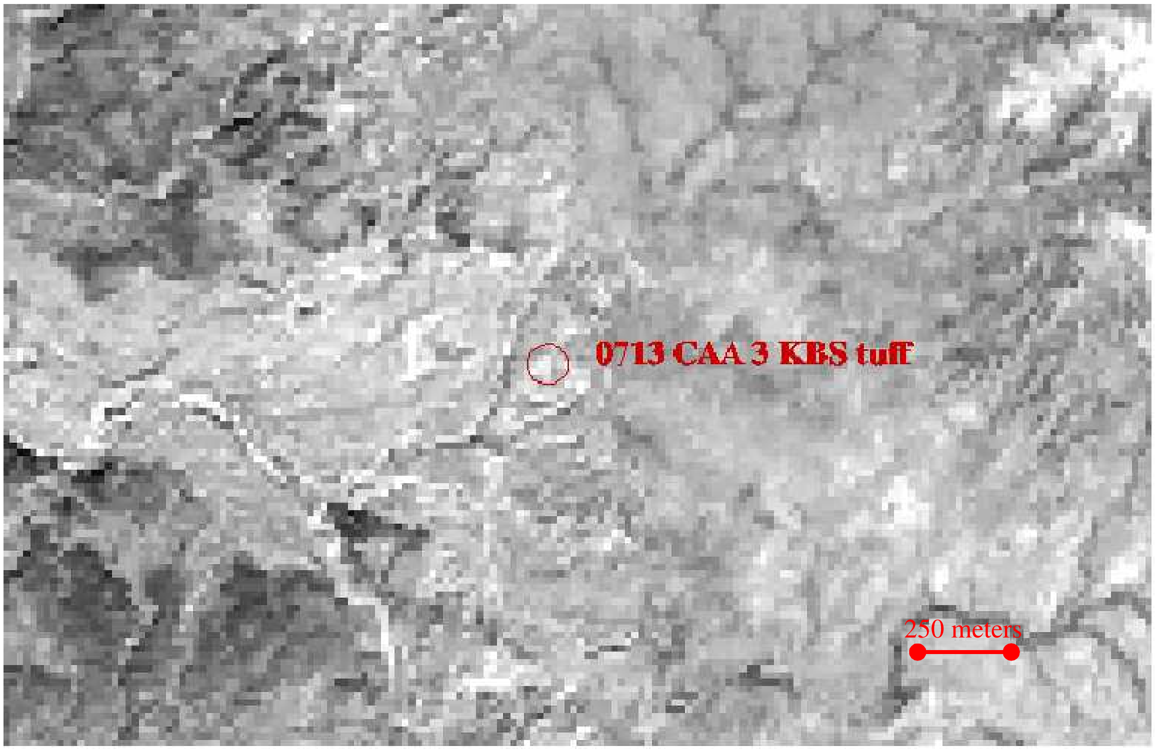

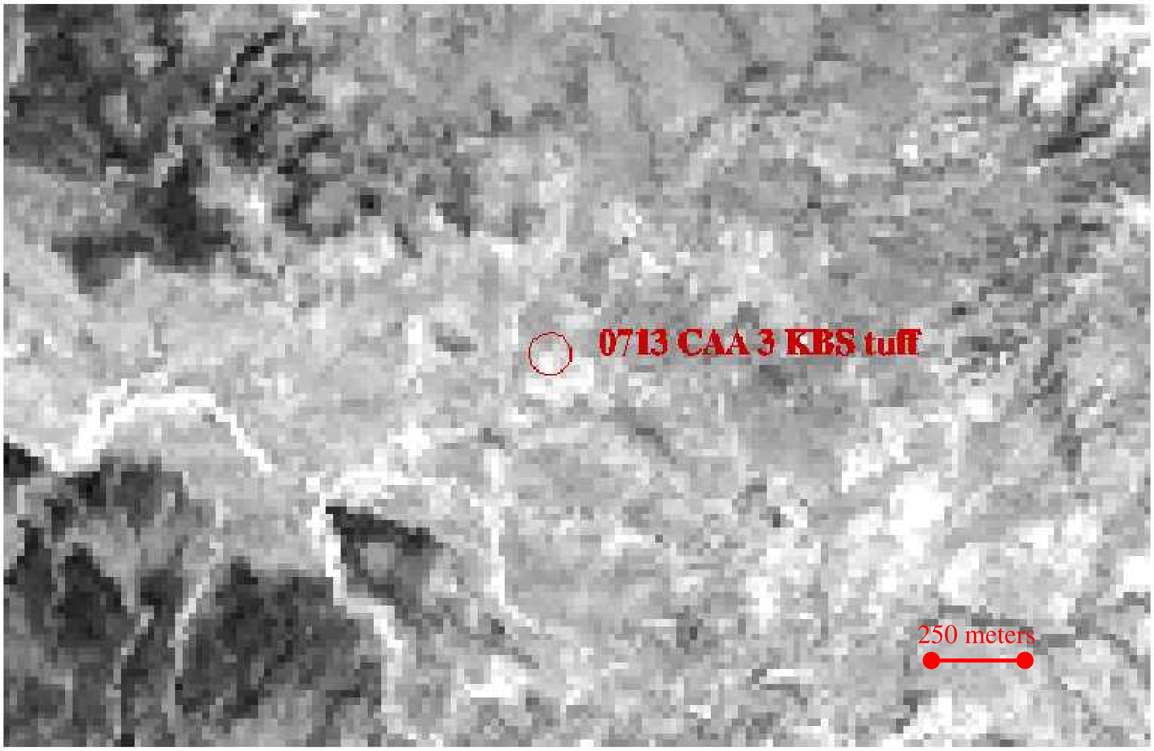

Figure 7.13. Comparison of run 1 (top) and run 2 (bottom) percent tuff cover maps. The tuff outcrop is better defined in run 2.

shows the run 1 tuff map for this area, and the bottom image shows the run 2 map. The tuff outcrop, which was selected as a geologic classification point and described in the field, was more clearly defined in the run 2 map. The tuff outcrops in the northern portion of the study area near Ileret were also more clearly defined in this image.

Figure 7.14 shows the percent carbonate cover map for run 2. This map is almost identical to the run 1 percent basalt cover map. Basalt is misclassified throughout the map as carbonate. The exceptions to this pattern are the Upper Burgi molluscan packstone in the southern portion of the map and the stromatolites near Ileret in the northern portion of the map. Both of these lithologies were misclassified as basalt in run 1. Because the pure spectra of tuff and carbonate are quite similar, confusion between these two lithologies would be expected but is not present in this map.

The percent vegetation cover map for run 2 is shown in Figure 7.15. Although the vegetation along the dry stream beds is classified correctly, the basalts in the northeastern and southeastern portions of the image are assigned to the vegetation class. The Kokoi Horst is also misclassified as vegetation. This result is not easily explained, as the pure spectrum for vegetation (Figure 7.6) is the exact opposite of that of tuff and carbonate. Vegetation has low radiance in band 14, high radiance in band 4, and low radiance in band 10. The RMS error map for run 2, shown in Figure 7.16, offers some insight into this issue. Error is high throughout much of the image. The areas with the highest RMS error throughout the maps are the basalt regions that are misclassified as carbonate and vegetation.

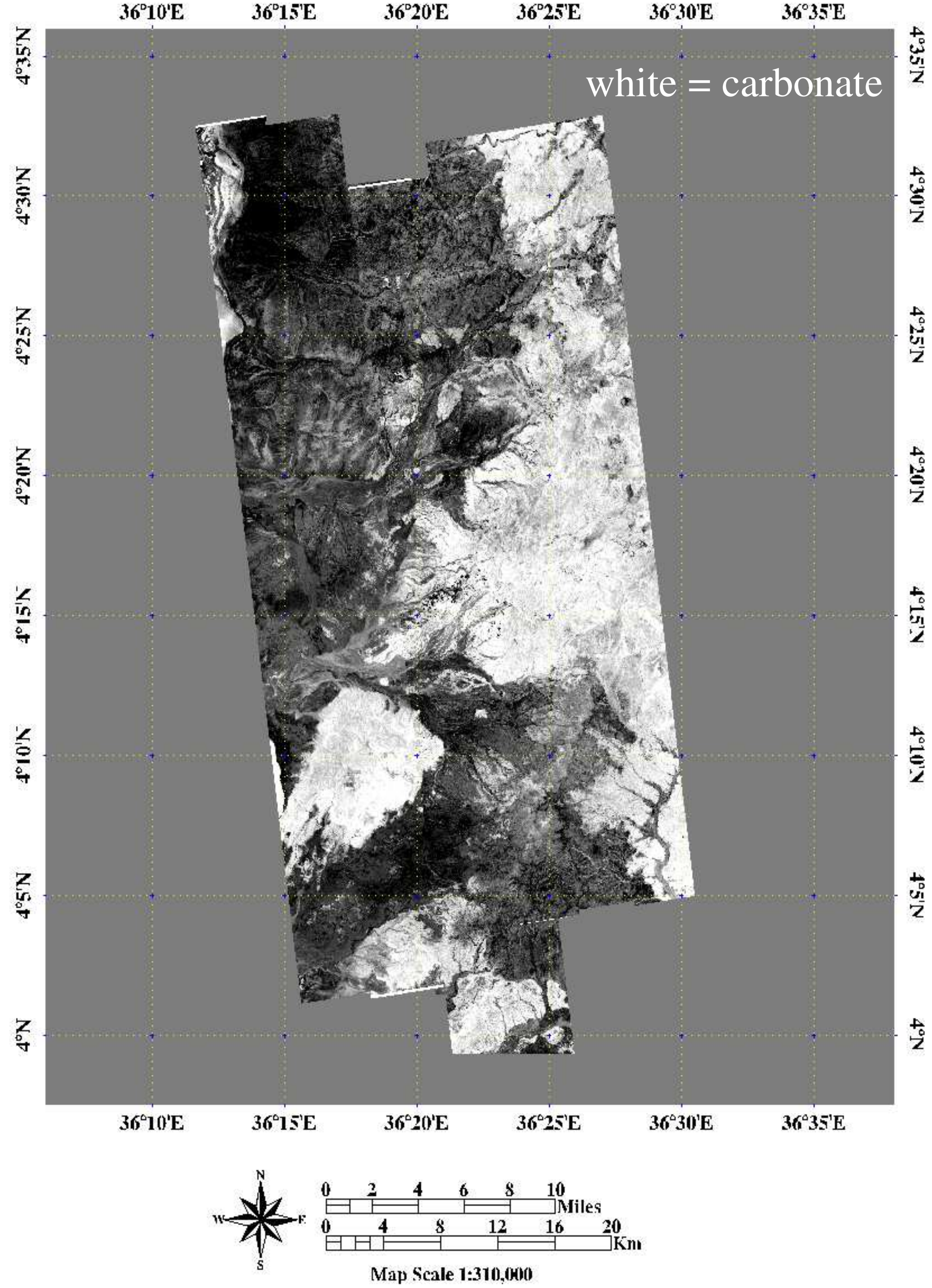

Figure 7.14. Run 2 (tuff/carbonate/vegetation) percent carbonate map.

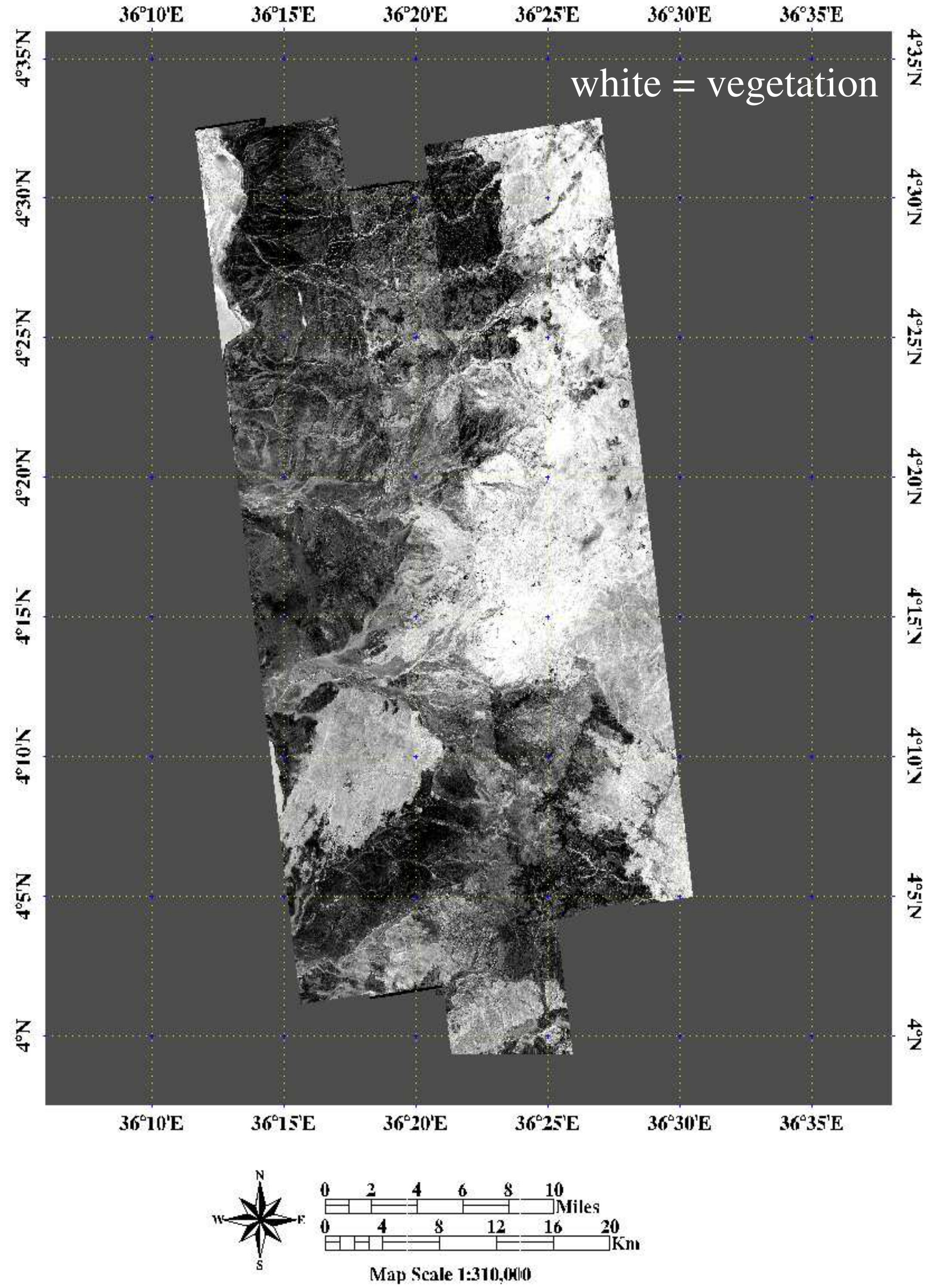

Figure 7.15. Run 2 (tuff/carbonate/vegetation) percent vegetation map.

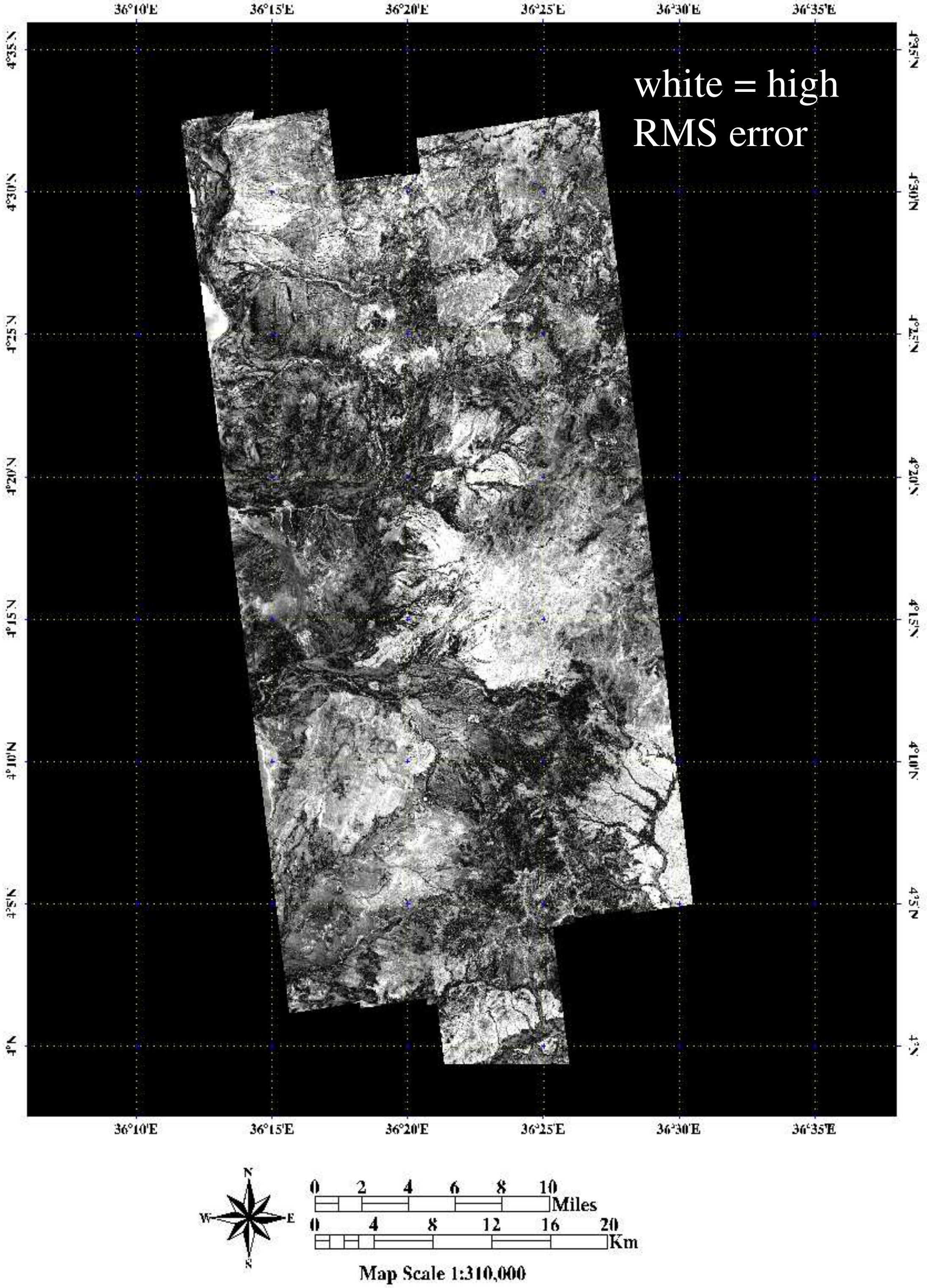

Figure 7.16. Run 2 RMS error map.

7.5 Results- run 3

Run 3 had the second highest overall accuracy of all of the runs. The error matrix for run 3 is shown in Table 7.4. This combination of pure spectra yielded an overall accuracy of 87.5 percent, and this bears out in a qualitative analysis of the imagery. In general, though some misclassification occurs, outcrops are constrained to their true bounds in the percent cover maps for this run. The graph of the normalized pure spectra (Figure 7.6) shows that basalt and vegetation have very different pure spectra when compared with one another. Each of these spectra is also very different from the similar spectra of tuff and carbonate. These differences may help to explain the accuracy of the run 3 maps.

	tuff	carbonate	basalt	vegetation		
tuff	7	1	0	0	8	
carbonate	3	9	0	1	13	
basalt	0	0	10	0	10	
vegetation	0	0	0	9	9	
	10	10	10	10	40	

	producer's accuracy %		user's accuracy %		overall accuracy %	
tuff	70		tuff	87.5		87.5
carbonate	90		carbonate	69.23		
basalt	100		basalt	100		
vegetation	90		vegetation	100		

Table 7.4. Error matrix for run 3.

The percent tuff cover map for run 3 is shown in Figure 7.17. Tuff definition is much less precise in this map than in any of the previous runs. The definition of tuff outcrops illustrated in Figures 7.8 and 7.13 is not possible in this map. However, the outcrops of tuff in the Ileret region and in the southwestern portion of the map display

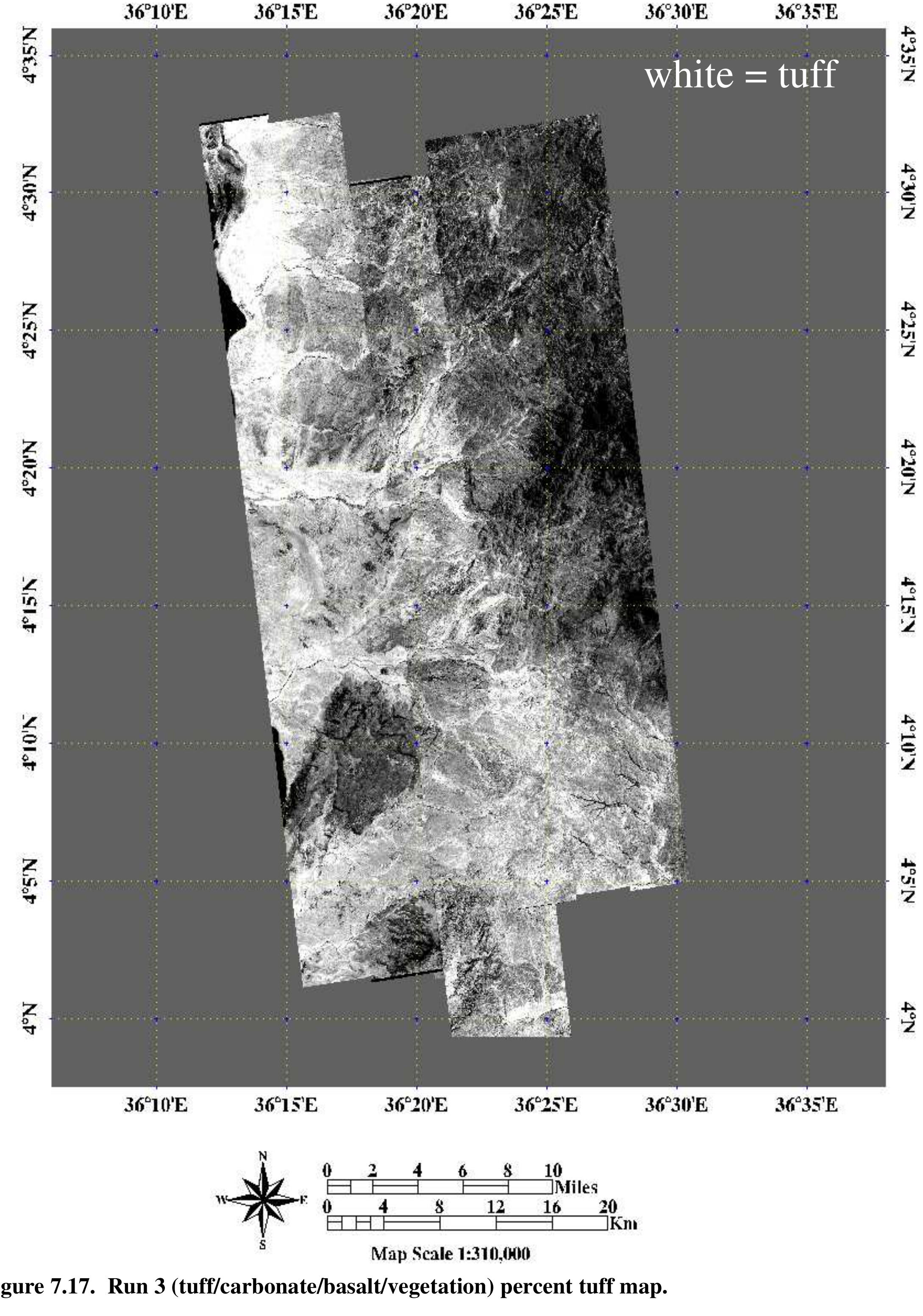

Figure 7.17. Run 3 (tuff/carbonate/basalt/vegetation) percent tuff map.

slightly better definition than in runs 1 and 2.

The percent carbonate cover map for run 3 is shown in Figure 7.18. This result is the best of any run in its definition of the carbonate outcrops in the study area. The Upper Burgi molluscan packstone in the southern portion of the image is more accurately defined in this map than in any other, and the stromatolites near Ileret are also well-defined. However, the northwestern edge of the Kokoi Horst and the basalt in the northeastern portion of the map are classified as carbonate. This misclassification is much less intense in degree than in run 2, but is nonetheless present.

Figure 7.19 shows the percent basalt cover map for run 3. The result is not as accurate as the first run, but is qualitatively quite good. All of the basalts in the northeastern portion of the image are correctly classified, the Kokoi Horst is correctly classified, and the stromatolites near Ileret are not incorrectly classified as basalt in this image. The only regions in which misclassification occurs are in the south-central portion of the map, where Upper Burgi bone beds have been classified as basalt, and in the southern portion of the image, where once again the Upper Burgi molluscan packstone is misclassified as basalt. However, as in the previous percent cover maps for this run, when misclassification occurred, it was less intense than in runs 1 and 2.

The percent vegetation cover map for run 3 is shown in Figure 7.20. As with the basalt class, this map is second in accuracy only to the run 1 percent vegetation cover map. The vegetation along the dry river and stream beds was well defined. The one notable exception to this is the very center of the map, which shows an anomalous

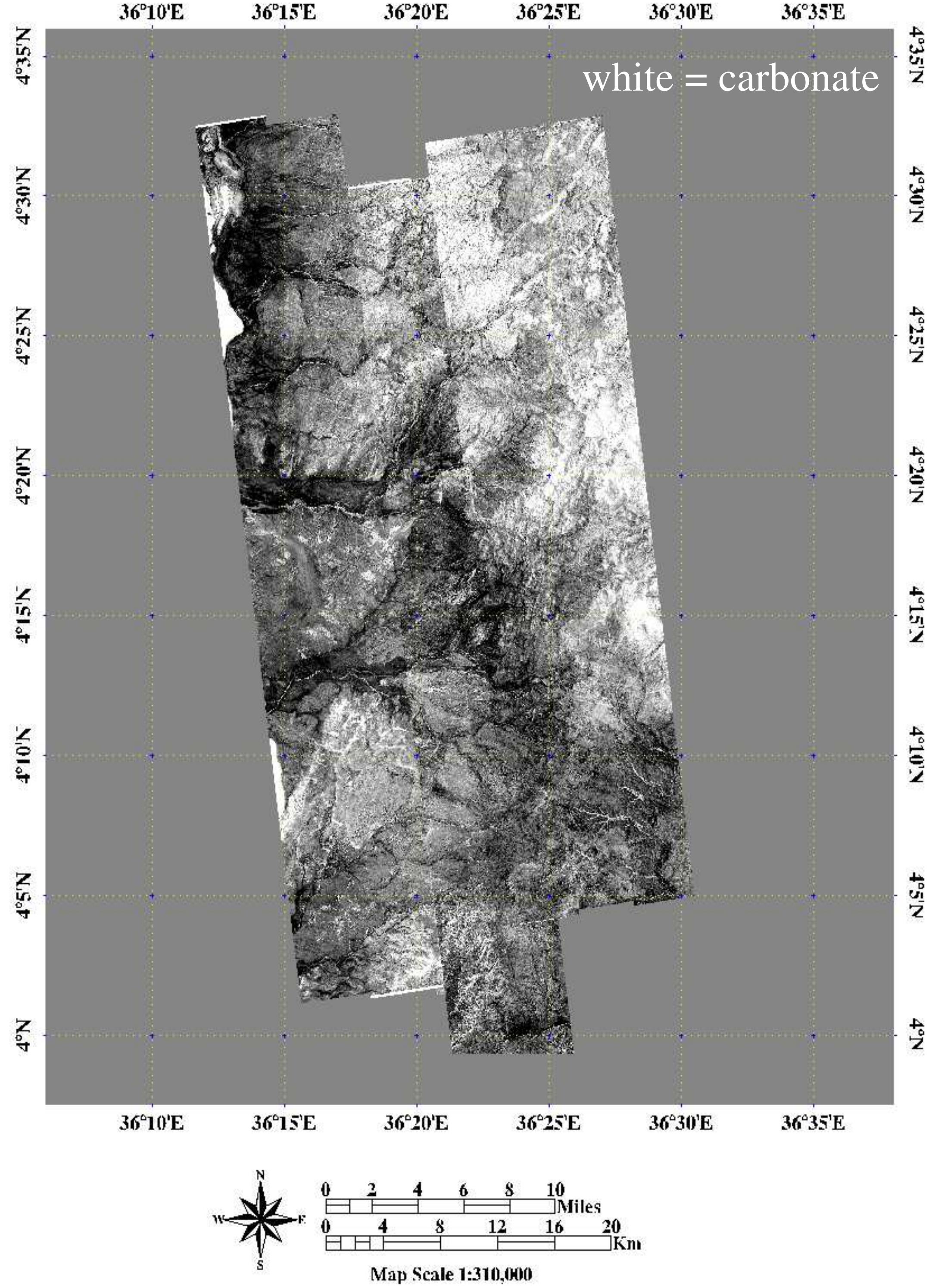

Figure 7.18. Run 3 (tuff/carbonate/basalt/vegetation) percent carbonate map.

response. As in the percent vegetation cover map for run 1 (Figure 7.10), this is most likely due to the contrast matching problem in the final mosaic. The RMS error map for run 3 (Figure 7.21) shows that the error is highest in the extreme northwest of the image and in areas where basalt was misclassified as vegetation. The rest of the image shows relatively low error, a finding which is supported by the error matrix (Table 7.4).

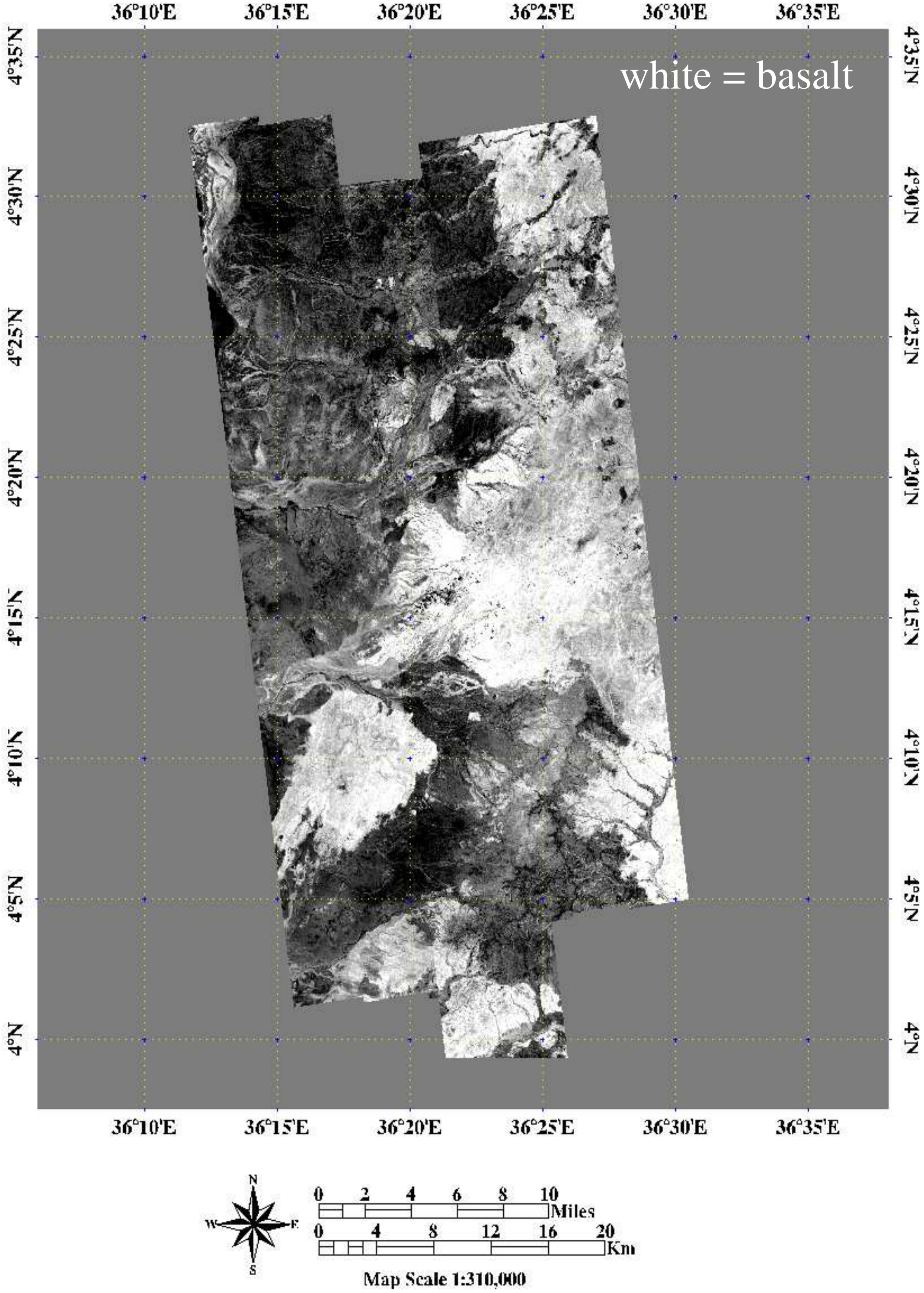

Figure 7.19. Run 3 (tuff/carbonate/basalt/vegetation) percent basalt map.

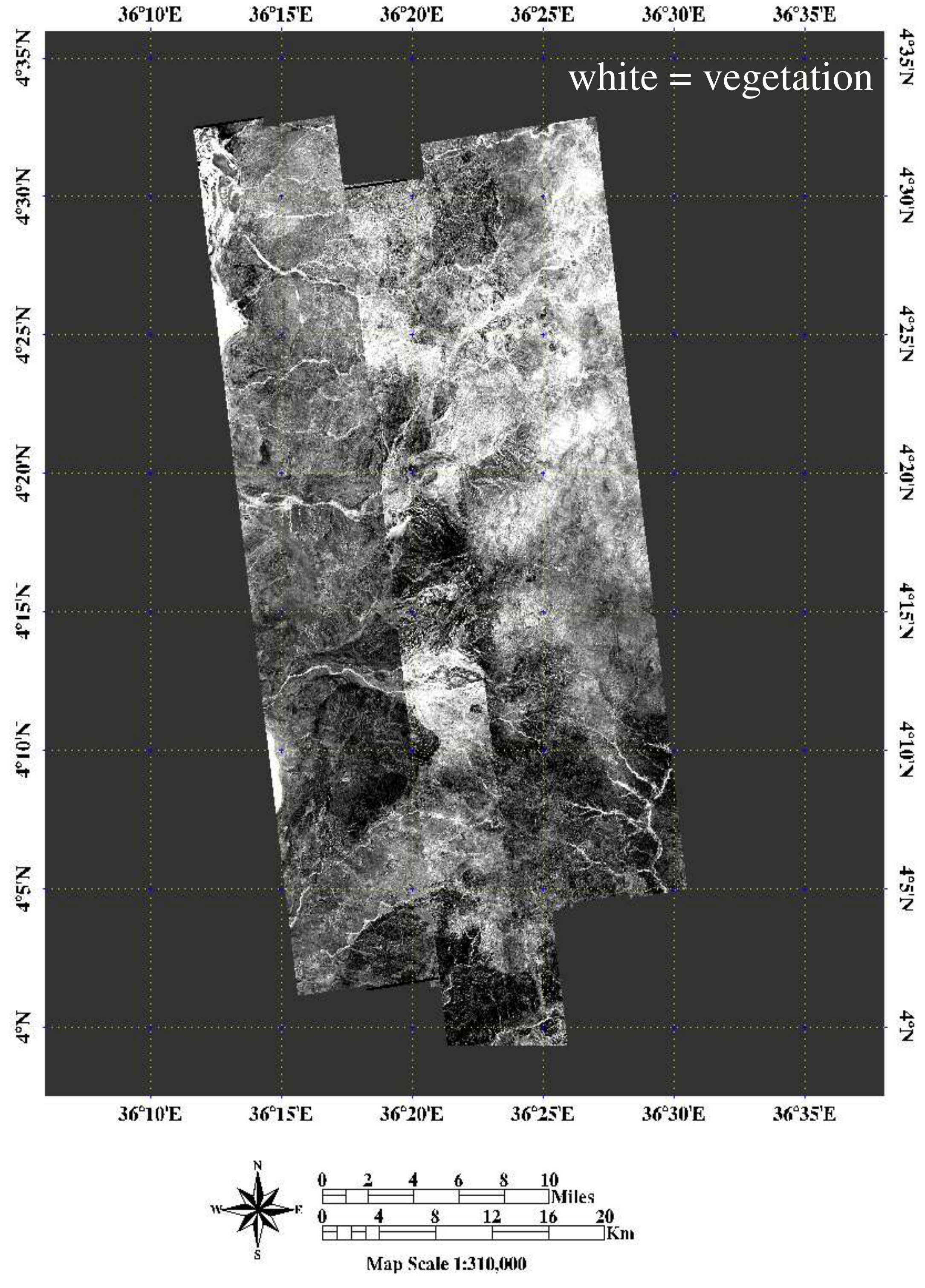

Figure 7.20. Run 3 (tuff/carbonate/basalt/vegetation) percent vegetation map.

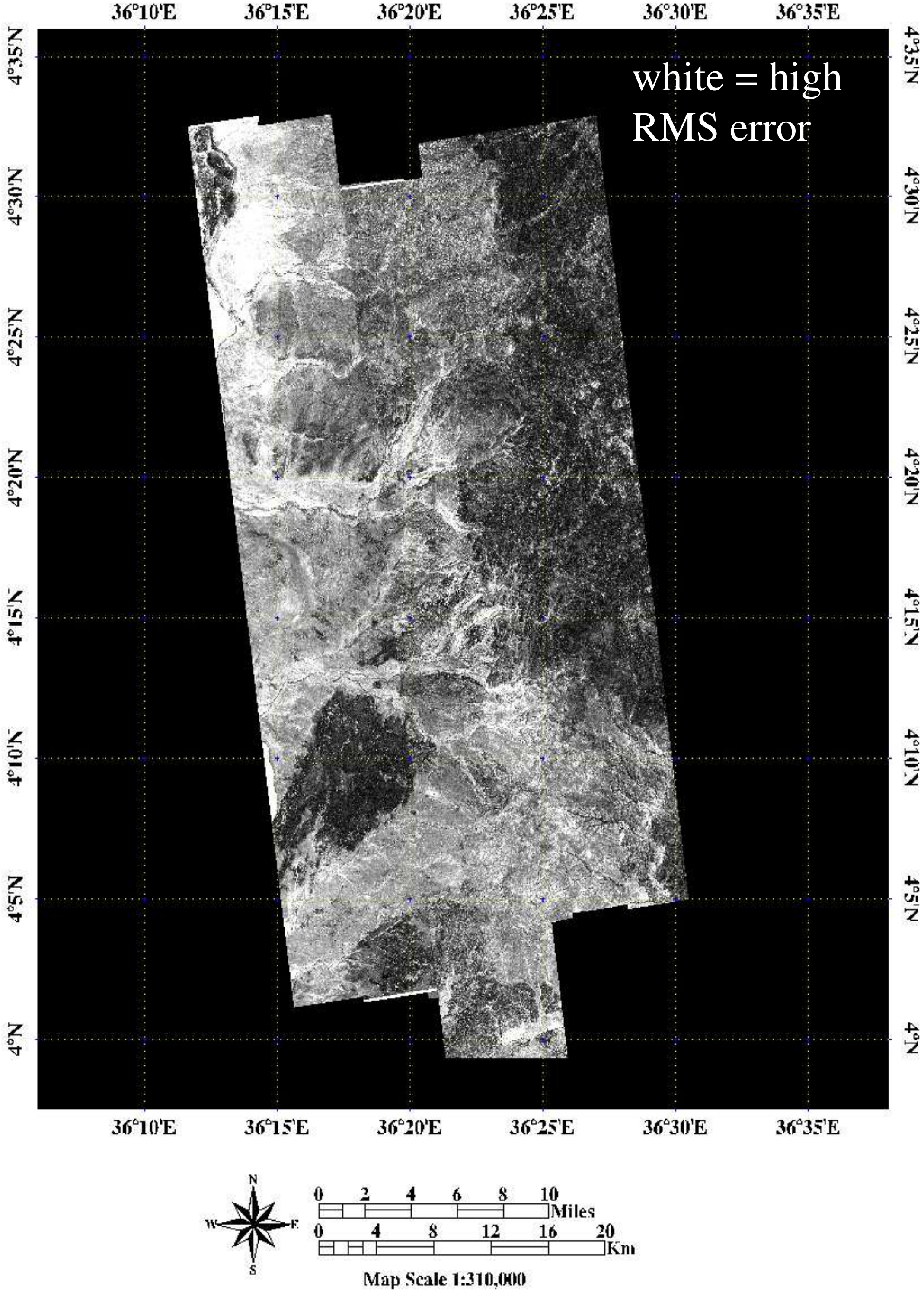

Figure 7.21. Run 3 RMS error map.

7.6 Results- run 4

As stated previously, the last run consisted of four geologic end members, tuff, alluvium, carbonate and basalt. The error matrix for run 4 is shown in Table 7.5. Introduction of the alluvium class into the unmixing algorithm brought the pure spectrum with the highest radiance in bands 4 and 10 into play. Furthermore, the graph of the normalized pure spectra (Figure 7.6) shows that alluvium and basalt have radiance responses that are almost exactly opposite of one another. However, in spite of the uniqueness of the alluvium pure spectrum, the results produced by inclusion of this class were not as accurate as the runs that included vegetation.

	tuff	alluvium	carbonate	basalt		
tuff	5	2	1	3	11	
alluvium	0	8	0	0	8	
carbonate	5	0	9	0	14	
basalt	0	0	0	7	7	
	10	10	10	10	40	

	producer's accuracy %		user's accuracy %		overall accuracy %	
tuff	50		tuff	45.45		72.5
alluvium	80		alluvium	100		
carbonate	90		carbonate	64.29		
basalt	70		basalt	100		

Table 7.5. Error matrix for run 4.

Figure 7.22 shows the percent tuff cover map for run 4. The 50% accuracy of tuff definition is accurate; qualitative analysis of this map also shows that this run produced the poorest definition of tuff. While the basalts in the northeastern portion of the map were not classified as tuff, portions of the basalt of the Kokoi Horst were classified as such. This is the only run in which confusion between tuff and basalt was seen.

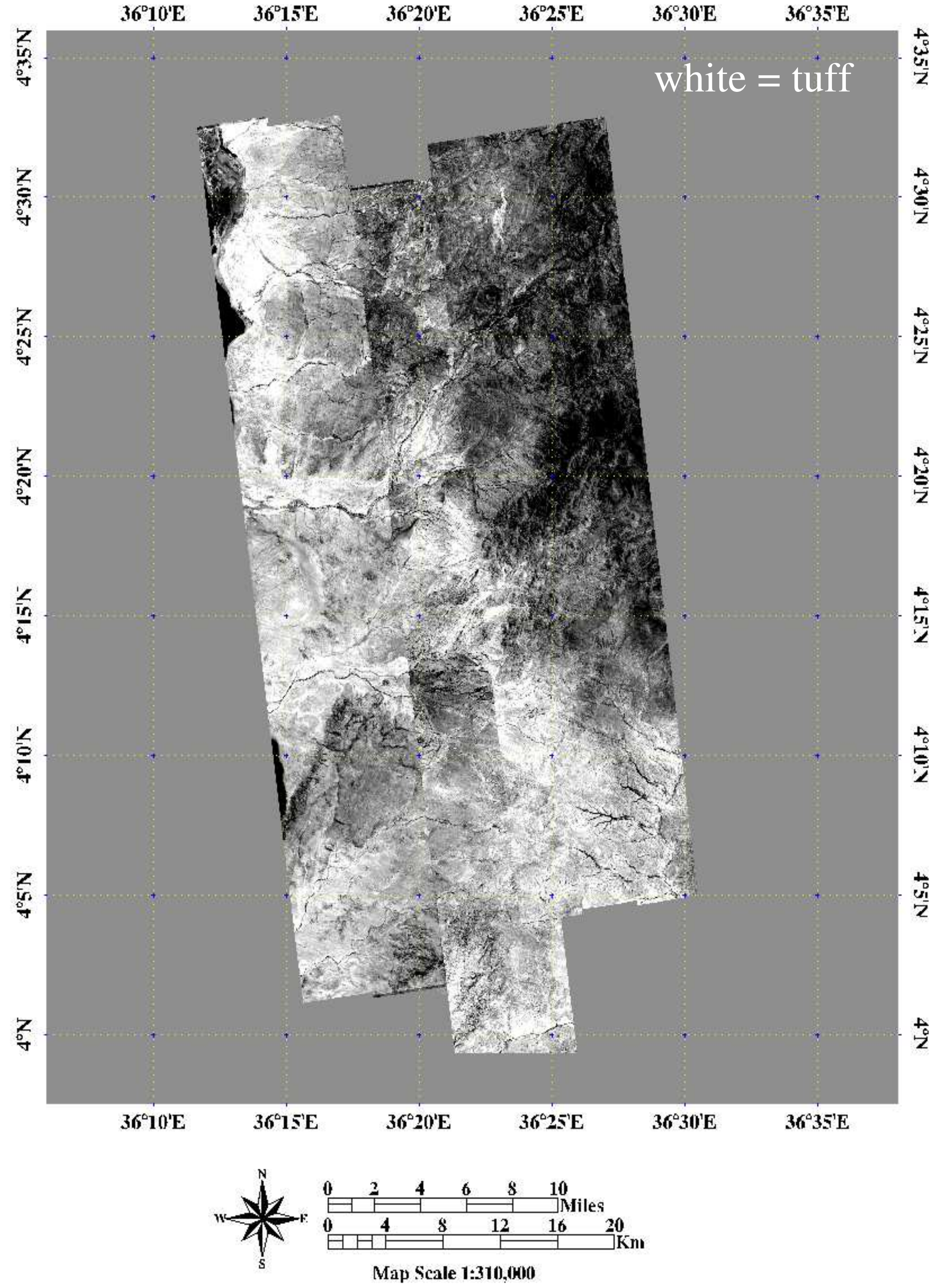

Figure 7.22. Run 4 (tuff/alluvium/carbonate/basalt) percent tuff map.

The percent alluvium cover map for run 4 is shown in Figure 7.23. The error matrix (Table 7.5) shows that the alluvium is the best defined class in the entire run. However, the percent alluvium cover map is identical to the percent vegetation cover map of run 3 (Figure 7.20). While the pure spectra for these two classes are distinct, the unmixing results were not. This illustrates the difficulty of defining a purely alluvium class or a purely vegetation class for Koobi Fora, as the distribution of vegetation within the study area is too closely linked to the dry river and stream beds and the lake shore.

The percent carbonate cover map for run 4 is shown in Figure 7.24. It is identical to the percent carbonate cover map from run 3 (Figure 7.18). The error matrix shows that run 3 and run 4 have a similar producer's and user's accuracy for carbonate as well. Qualitatively, the map analysis is the same as that of Figure 7.18; the algorithm defined carbonate very well in this run.

Figure 7.25 shows the percent basalt cover map for run 4. In spite of the error matrix (Table 7.5), it is the least accurate basalt map produced by the unmixing algorithm. While the basalt in the northeastern portion of the map was classified correctly, the Kokoi Horst and the basalt in the southeastern portion of the map were not. However, it should be noted that this is the only basalt unmixing result that did not classify the Upper Burgi molluscan packstone as basalt. The RMS error map for run 4 (Figure 7.26) shows that error is high throughout much of the image, but that it is relatively low in the Kokoi Horst region and in the northeastern portion of the mosaic. The poor definition of basalt in this map may be due to the cancellation effect of the

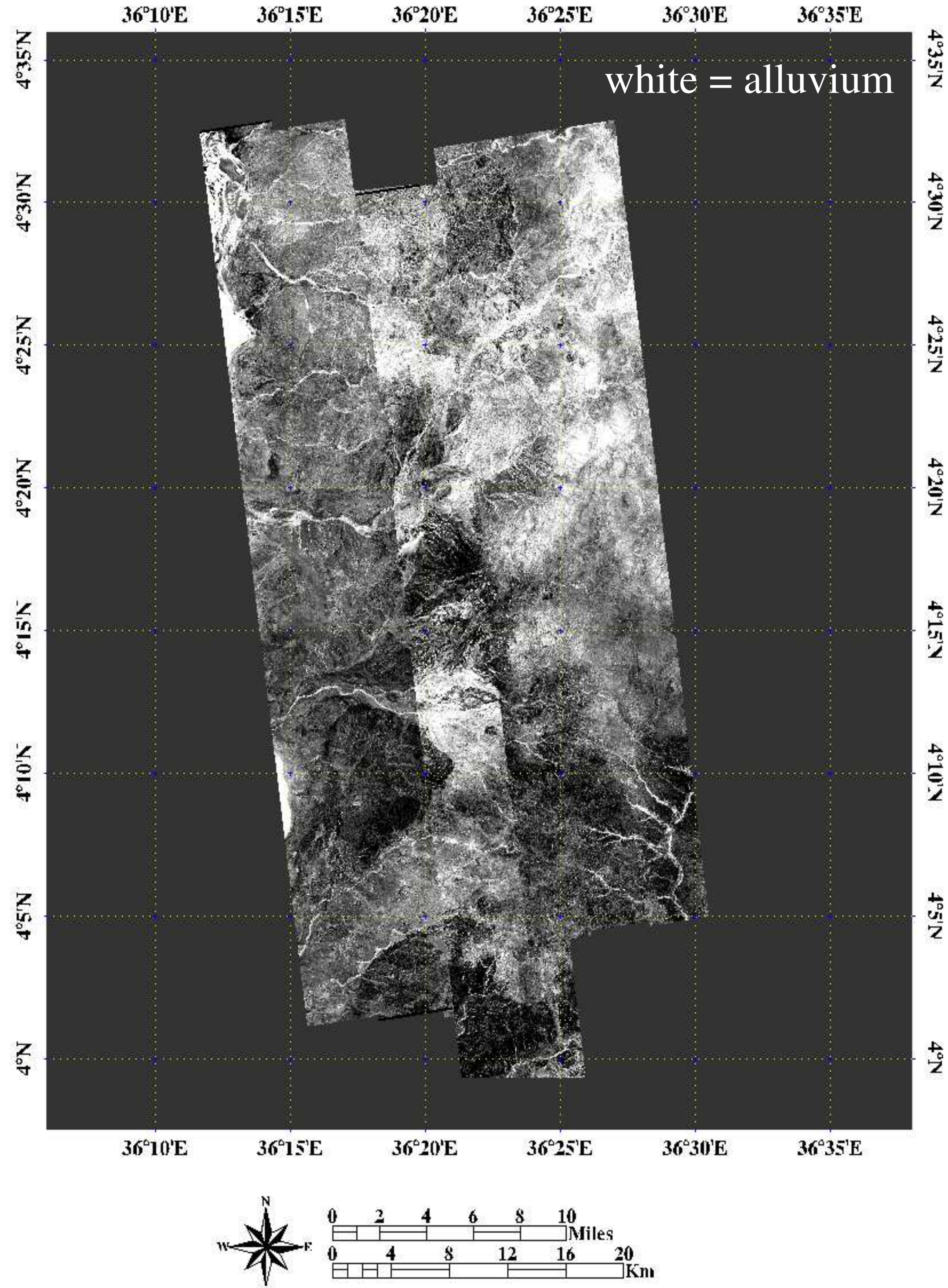

Figure 7.23. Run 4 (tuff/alluvium/carbonate/basalt) percent alluvium map.

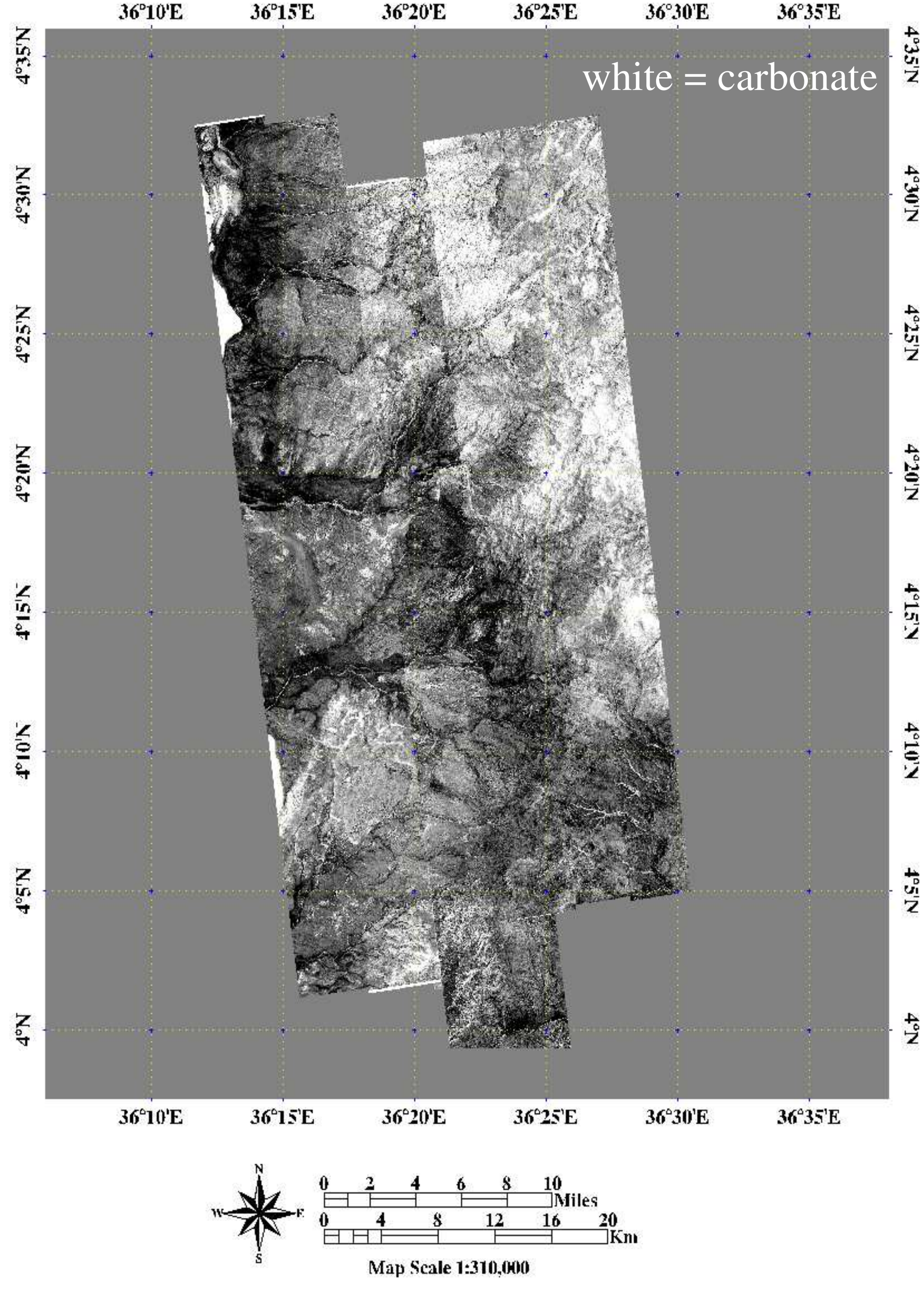

Figure 7.24. Run 4 (tuff/alluvium/carbonate/basalt) percent carbonate map.

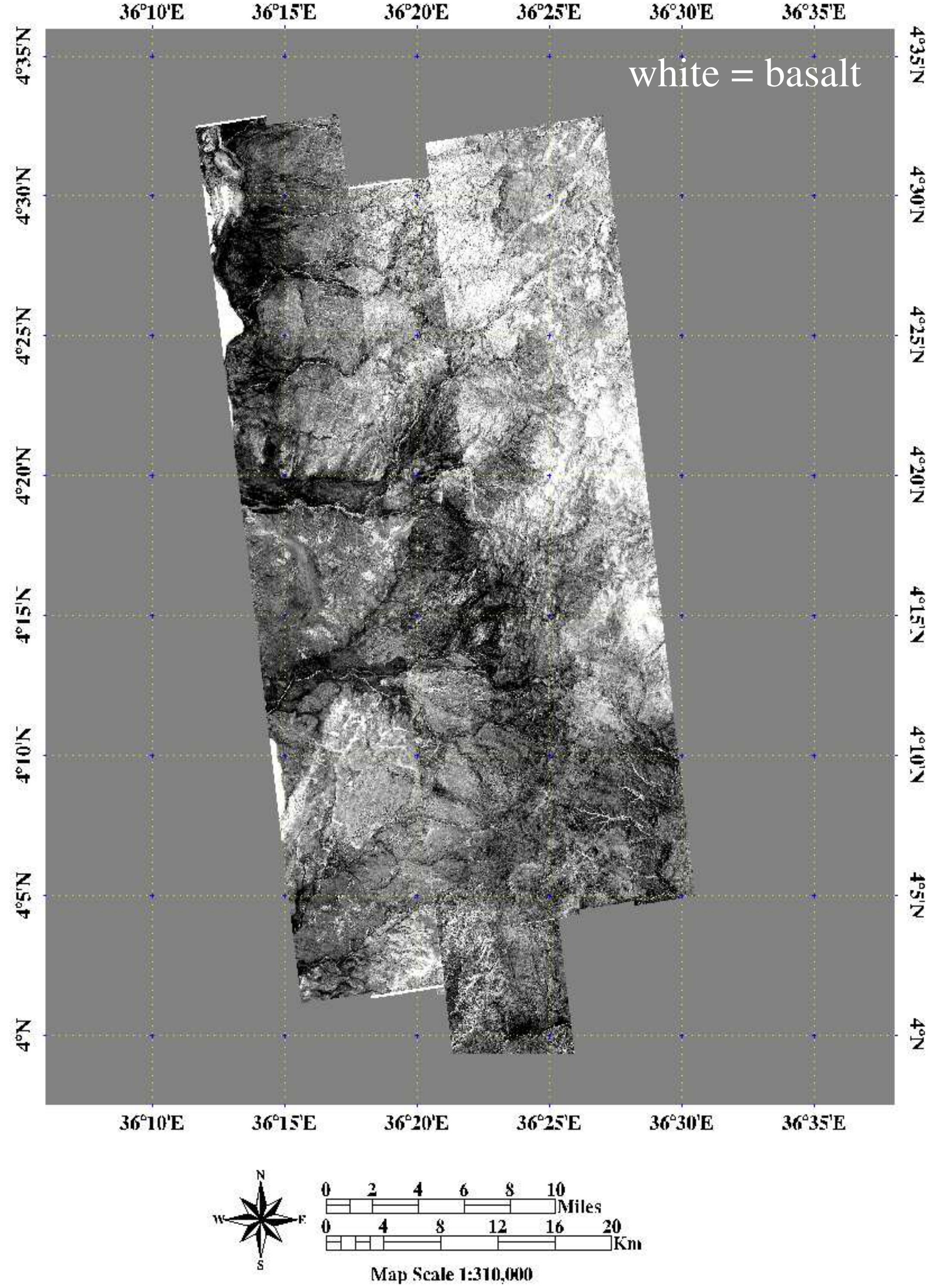

Figure 7.25. Run 4 (tuff/alluvium/carbonate/basalt) percent basalt map.

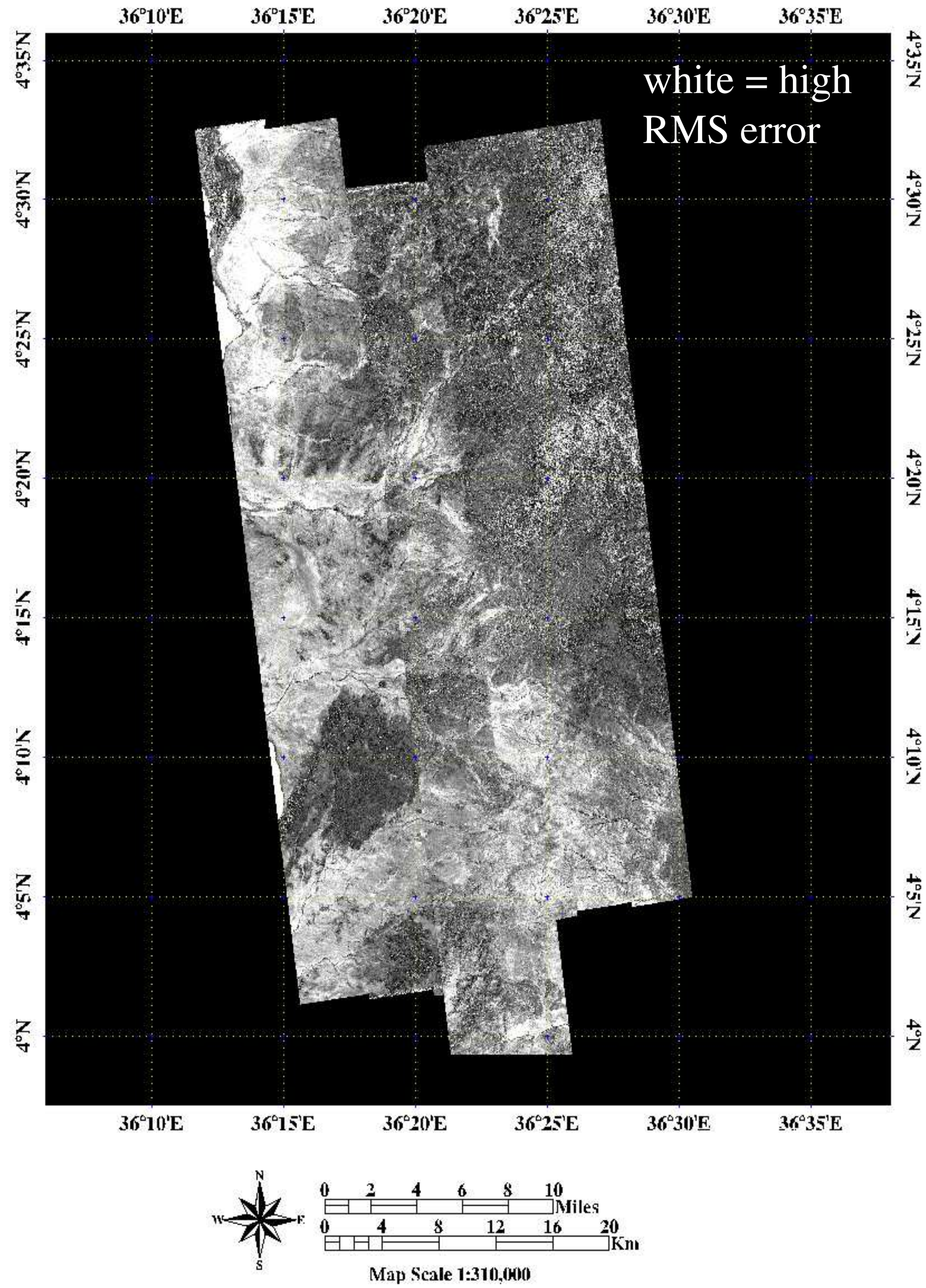

Figure 7.26. Run 4 RMS error map.

alluvium pure spectrum, which is almost exactly opposite of that of basalt.

In summary, the success of pure spectrum definition in the unmixing products depended on the combination of pure spectra used. The best definition of tuff took place in runs 1 and 2, and the worst definition of tuff took place in run 4. The best definition of basalt took place in runs 1 and 3, and the worst definition of basalt took place in run 4. The best definition of carbonate took place in run 3, and the worst definition of carbonate took place in run 2. Finally, the best definition of vegetation took place in runs 3 and 1, and the worst took place in run 2. The almost identical nature of the percent vegetation cover map in run 3 and the percent alluvium cover map in run 4 suggests that, though their pure spectra are very different, the alluvium and vegetation pure spectra might best be combined into one class.

CHAPTER 8
CONCLUSIONS AND FURTHER RESEARCH

This research defined the pure spectra for tuff, basalt, and carbonate within the Koobi Fora Formation, as well as those of alluvium/vegetation. This was achieved via a combination of field description and historical map research. A digital surface geologic map of a portion of the Koobi Fora Formation with an absolute accuracy of 73 meters has been created.

The linear spectral unmixing algorithm used to analyze the MTI data yielded results with varying degrees of quantitative and qualitative accuracy. In sum, the success of geologic classification of the MTI mosaic via linear spectral unmixing depended on the combination of pure spectra used in the unmixing process and accurate class definition. The error matrix for run 1, which states that all classes are defined with 100% accuracy, is misleading. This result does not mean that tuff is defined throughout the image in a completely accurate manner; rather, this figure means that the definition of tuff was completely accurate for the defined regions of interest.

Misclassification of carbonate as basalt occurs in run 1 as a result of the similar spectral responses that dark carbonate and basalt have in the thermal infrared. Likewise, runs with lower total quantitative accuracy produced unmixing results that were somewhat qualitatively better than run 1. Definition of alluvium and vegetation as separate classes is most likely unnecessary; though pure spectra were defined for each for these classes, both the observed spatial relationship between them and the unmixing results suggests that they are highly correlated and should be one class.

Nevertheless, definition of the tuff members of the Koobi Fora Formation was highly accurate when the right combinations of lithology and vegetation were used with the unmixing algorithm. To differentiate the Koobi Fora tuffs precisely, it is best to use a combination of pure spectra that are very different and do not consist of different polymorphs of SiO_2. Definition of similar tuffs in other areas of the East African Rift System may be aided by the pure spectrum defined for the Koobi Fora Formation. Spectral definition of basalts in the study area was also quite successful, and separation of volcanics from sedimentary lithologies via spectral unmixing may also prove useful in other tectonically complex areas of the rift. The ability to successfully differentiate these lithologies demonstrates MTI's utility as a geologic mapper, and it may be useful to include an MTI-like sensor on a future satellite mission for this reason.

Future research with the map products from this study may take many forms. It may be useful to take some of the more accurate unmixing maps into the field to test their accuracy. It may also be useful to compare the MTI unmixing results with unmixing results from hyperspectral satellite imagery. Such a study may indicate if it is possible to classify the geology of the Koobi Fora Formation more accurately with the pure spectra defined herein and data that have different band definitions.

LIST OF APPENDICES

APPENDIX A

Geologic classification points

All points are within the Koobi Fora Formation unless otherwise noted.
Moisture is dry unless otherwise noted.

July 6, 2003

Point 1
Member: Chari Tuff
Very fine grained, well sorted, buff sandy tuff, color 10 YR 8/2, no vegetation.

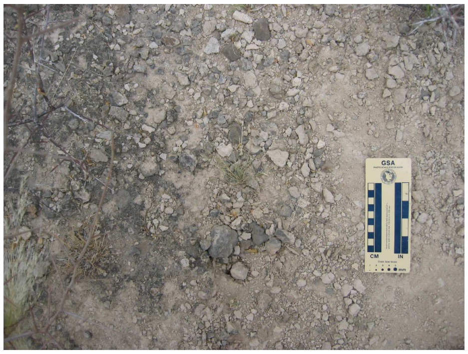

Point 2

Member: Okote

Well sorted carbonate nodules (1-3 cm), color 10 YR 8/1, no vegetation.

July 7, 2003

Point CAA_1

Formation: Galana Boi

Medium to coarse grained, subangular, moderately sorted sand, color 10 YR 8/6, vegetation cover over the entire site (*Comiphera,* grasses).

Point 2

Member: Okote

Angular well sorted quartz and carbonate pebbles (4-5 cm), color 2.5 Y to 2.5 Y 4/1, no vegetation.

Point 3

Member: Okote

Heavily cemented subangular carbonate pebbles (0.5-1 cm), color 2.5 Y 8/2, no vegetation.

Point 4

Member: Okote

Coarse to very coarse grained, angular, well sorted sand and carbonate pebbles (1-2 cm), color 2.5 Y 7/3, no vegetation.

July 8, 2003

Point CAA_4

Formation: alluvium

Very coarse grained, subangular to angular, poorly sorted silty sand, color 10 YR 6/6, vegetation cover over entire landscape (a few *Acacia, Comiphera,* grasses).

Point CAA_14

Member: Upper Burgi

Angular, poorly sorted carbonate pebbles (4-5 cm) and red chert fragments, color 2.5 YR 4/6, sparse vegetation (*Acacia*, grasses).

Point 3

Member: KBS Tuff

Very fine grained, very well sorted gray tuff, breaks into glass grains out of outcrop, color GLEY 1 7/10 Y, sparse grasses.

Point 4

Formation: alluvium

Rounded to subangular, poorly sorted mixed lithology sand and gravel (basalt pebbles, quartz sand), color 10 YR 2/1 (basalt pebbles) and 10 YR 6/3 (quartz sand), no vegetation.

July 9, 2003

Point CAA_1

Formation: alluvium

Very fine grained, very well sorted silty sand, color 7.5 YR 5/3, heavy vegetation (*Acacia*, *Comiphera*, dead grasses).

Point CAA_8

Formation: alluvium

Coarse to medium grained, subrounded to subangular, well sorted mixed lithology sand (quartz, basalt, hornblende, mica), color 2.5 Y 7/2, no vegetation.

July 10, 2003

Point 1

Formation: alluvium

Medium to coarse grained, angular, well sorted silty quartz sand, color 10 YR 6/4, sparse vegetation (*Comiphera*, dead grass).

Point 2

Formation: alluvium

Sandy silt, a few basalt cobbles on land surface, color 10 YR 6/3 (slightly moist), brown silt matrix containing sand grains, well rounded and well sorted, vegetation sparse (dead grass, sparse *Comiphera* bushes, a few *Acacia*).

Point 3

Formation: Tertiary volcanics, Kokoi outlier

Basalt pebbles with basalt boulders on outcrop, color 5 YR 4/1, pebbles are about 1 cm in size, lots of vegetation (*Comiphera* bushes, cactus, dead grass).

Point 4

Formation: Tertiary volcanics, Kokoi Horst

Basalt, weathered red, color 2.5 YR 4/4, columnar structure, sparse *Acacia* vegetation, some *Comiphera* bushes.

July 12, 2003

Point 1

Member: Chari Tuff

Fine grained buff tuff, color 10 YR 7/2,, no vegetation.

Point 2

Member: Okote

Very fine grained silts, color 10 YR 6/4, no vegetation.

Point 3

Member: upper KBS

Heavily cemented carbonate rock, color 10 YR 8/2, no vegetation on site surface.

July 13, 2003

Point 1

Member: post-KBS erosional surface

Heavily cemented carbonate sands, color 10 YR 8/2, weathering into large pebbles/small cobbles, no vegetation.

Point 2

Member: KBS Tuff

Fine grained tuff, color 2.5 Y 8/2, no vegetation.

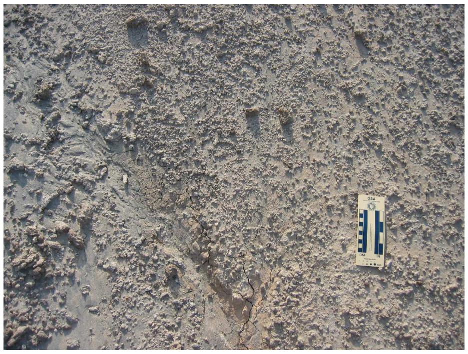

Point 3

Member: KBS Tuff

Fine grained tuff, color 10 YR 8/2, no vegetation.

July 14, 2003

Point 1

Member: Okote

Extremely fine grained, well sorted silts, some tuffaceous/carbonate surface nodules (size 1 cm), color 10 YR 6/4, grasses and stunted *Comiphera* vegetation.

Point 2

Member: Okote

Mixed rock type variegated pebbles (0.5 to 2 cm) covering surface, extremely fine-grained, well-sorted silts underneath, color 10YR 6/3, no vegetation.

Point 3

Member: Okote

Stream channel gravels (2 cm), color 10 YR 3/1, extremely fine grained, well sorted silts underneath, color 10 YR 6/4, no vegetation.

Point 4

Member: Okote

Conglomerated (well cemented in outcrop) very coarse grained, subrounded, moderately sorted silty sands, color 10 YR 6/4, no vegetation.

Point 5

Member: Okote

Very fine grained, well sorted silt, color 10YR 6/4, and carbonate pebbles (1 cm), no vegetation.

CAA point 6
Member: Okote
Carbonate pebbles (0.5 to 2 cm), color 10 YR 8/1, no vegetation.

Point 7
Member: KBS Tuff
Fine grained tuff weathering to powder, color 10 YR 6/1, no vegetation.

Point 8
Member: Upper Burgi
Claystone, color 10 YR 5/4, no vegetation.

Point 9
Member: undetermined, probably Okote
Very fine to very coarse grained, subangular, very poorly sorted mixed lithology (quartz, calcite, volcanic) sands, dominant color is 10 YR 6/4, and angular carbonate pebbles (1-2 cm), color 10 YR 8/3, and well rounded basalt pebbles (0.5 to 1 cm), color 10 YR 4/1, no vegetation.

Point 10
Member: Okote
Very coarse to medium grained, well sorted mixed lithology (quartz, mica, hornblende) silty sand, color 10 YR 6/3, and angular carbonate pebbles (0.5 to 2 cm), color 10 YR 8/2.

July 17, 2003

Point 1

Member: Okote

Coarse grained, subrounded, poorly sorted silty sand and pebbles (0.5 cm), color 10YR 8/2, sparse vegetation (*Acacia*, grasses).

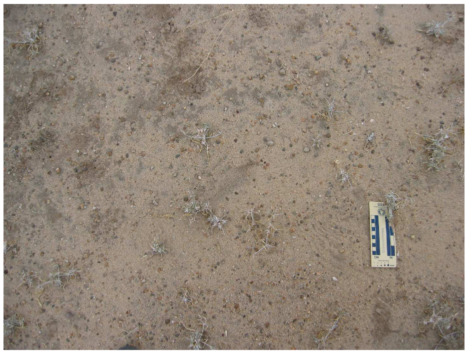

Point 2

Formation: alluvium

Coarse grained, subangular, well sorted quartz and basalt sand, surface mottled, colors 10 YR 8/2 and 10 YR 2/1, no vegetation.

Point 3
Formation: Okote
Carbonate pebbles (1-2 cm), color 10 YR 7/2, sparse vegetation (grasses only).

July 19, 2003
Point 1
Member: Upper Burgi
Angular orange carbonate pebbles (2-3 cm) and sandy silts, color 10 YR 5/8 (pebbles) and 10 YR 4/4 (silt), no vegetation.

Point 2
Member: KBS Tuff
Very fine grained, very well sorted tuff, color GLEY 2 7/5B.

Point 3
Member: Upper Burgi
Carbonate molluscan packstone, color 7.5 Y 2 to 7.5 YR 5/6, no vegetation.

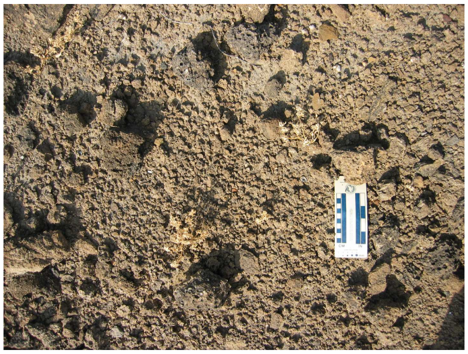

Point 4
Member: undetermined, possibly Okote
Angular well sorted carbonate nodules (1 cm) and silt, color 10 YR 8/2 (carbonate) and 5 YR 5/3 (silt)

July 20, 2003

Point 1
Member: KBS tuff in area 130
Fine grained tuff, weathering to powder, black weathering rind on top of outcrop, color 10 YR 6/2, grass, *Comiphera*, and acacia vegetation on outcrop.

Point 2
Member: Upper Burgi
NOTE: It is really hard to tell if this area is KBS post-erosional surface or Upper Burgi. Well sorted angular pebbles of carbonate (1 cm), color 10 YR 7/2, and angular blocky clay nodules (0.5 cm or less), color 10 YR 5/2, sparse dead grass to barren outcrop.

July 21, 2003
Point 1
Member: Upper Burgi
Carbonate sands and pebbles (2-3 cm), black with red and gray clays underneath, color 10 YR 3/2, no vegetation.

Point 2
Formation: alluvium
Very coarse to medium grained, subangular, well sorted quartz sand, color 10 YR 8/2, no vegetation.

Point 3
Member: Upper Burgi
Claystone, popcorn weathering, color 10 YR 6/3, no vegetation.

July 23, 2003

Point 1

Member: Upper Burgi

Carbonate sand and angular gravel/pebbles (2-3 cm), a few cobbles, color 10 YR 6/4, surface weathers red to black in some areas, no vegetation.

Point 2

Formation: undetermined

Carbonate sands, color 10 YR 4/4, and gravel, color 10 YR 2/1 with a black to red weathering patina, no vegetation.

Point 3
Formation: alluvium
Very coarse to medium grained, subrounded, moderately sorted quartz and hornblende sand, color 10 YR 8/6, scattered *Comiphera* and *Acacia* vegetation.

Point 4
Member: Chari Tuff
Subangular to well rounded, poorly sorted tuffaceous silts and carbonate pebbles (1 cm), color 10 YR 6/4, heavy vegetation, mostly *Comiphera* thickets.

July 24, 2003

Point 1
Formation: Upper Burgi
Angular carbonate pebbles to gravel (2-3 cm), 10 YR 6/3, no vegetation, numerous hippo bones across the entire surface.

REFERENCES

Altman, D., 1994. Fuzzy set theoretic approaches for handling imprecision in spatial analysis. International Journal of Geographical Information Systems, 8, no. 3, pp. 271-289.

Asfaw, B., et al., 1990, Space-based imagery in paleoanthropological research: an Ethiopian example. National Geographic Research, 6, pp. 418-434.

Bainbridge, R.B., 1976. Stratigraphy of the Lower Member, Koobi Fora Formation, northern Karari Escarpment, East Turkana Basin, Kenya. Iowa State University unpublished Masters thesis, Ames, IA, pp. 133.

Baker, B.H., Mohr, P.A., and Williams, L.J., 1972. Geology of the eastern rift system of Africa. The Geological Society of America Special Paper 136, Boulder, CO, pp 67.

Barsi, A., 1995. Thematic mapping of the Naivasha region (Kenya) from Landsat images. Periodica Polytechnica Civil Engineering, 39, no. 2, pp. 127-133.

Beaumont, E.A. and Foster, N.H. (eds.), 1992. Remote Sensing. The American Association of Petroleum Geologists Treatise of Petroleum Geology Reprint Series, 19, Tulsa, OK, pp. 605.

Behrensmeyer, A.K. and Issac, G.L., 1997. Geological context and paleoenvironments. *In*: Isaac, G.L. (ed.), The Koobi Fora Research Project Volume 5: Plio-Pleistocene Archaeology. Clarendon Press, Oxford, UK, pp. 12-70.

Bell, W.R. and Weber, P.G., 2001. Multispectral thermal imager- overview. LA-UR-01-1253, Los Alamos National Laboratory Unclassified Research Library, pp. 11.

Bowen, B.E., 1974. The Geology of the Upper Cenozoic in the East Rudolf Embayment of the Lake Rudolf Basin, Kenya. Iowa State University unpublished Ph.D. dissertation, Ames, IA, pp. 164.

Brown, F.H., 1994. Development of Pliocence and Pleistocene chronology of the Turkana Basin, East Africa, and its relation to other sites. *In*: Corruccini, R.S. and Ciochon, R.L. (eds.), Integrative Paths to the Past. Prentice Hall, Englewood Cliffs, NJ, pp. 285-312.

Brown, F.H. and Feibel, C.S., 1986. Revision of lithostratigraphic nomenclature in the Koobi Fora region, Kenya. Journal of the Geological Society of London, 143, pp. 297-310.

---1991. Stratigraphy, depositional environments, and paleogeography of the Koobi Fora Formation. *In*: Harris, J.M. (ed.), The Koobi Fora Research Project Volume 3: Fossil Ungulates: Geology, Fossil Artiodactyls, and Paleoenvironments. Clarendon Press, Oxford, UK, pp. 1-30.

Burggraf, D.R., 1976. Stratigraphy of the Upper Member, Koobi Fora Formation, southern Karari Escarpment, East Turkana Basin, Kenya. Iowa State University unpublished Masters thesis, Ames, IA, pp. 116.

Clodius, W.B., 2004. The multispectral thermal imager sensor. *In*: Lawson, S.L. and Krone, J.B. (eds.), Multispectral Thermal Imager Four-Year Report. LA-UR-04-3378, Los Alamos National Laboratory Unclassified Research Library, pp. 5-14.

de Jong, S.M., and Riezebos, H.T., 1990, The Use of Multispectral Satellite Images for Land Use and Land Cover Mapping in Kakamega District, Kenya. University of Utrecht unpublished report, Utrecht, NL, pp. 56.

de Menocal, P.D., 1995. Plio-Pleistocene African climate. Science, 270, pp. 53-59.

de Wit, A., 2001. Runoff controlling factors in various sized catchments in a semi-arid Mediterranean environment in Spain. Nederlanse Geografische Studies, 284, Utrecht, NL, pp. 240.

Drury, S., 2001. Image Interpretation in Geology. Blackwell Science Publishing, Malden, MA, pp. 290.

Dunkelman, T.J., Karson, J.A., and Rosendahl, B.R., 1988. Structural style of the Turkana Rift, Kenya. Geology, 16, pp. 258-261.

Feibel, C.S., Brown, F.H., and McDougall, I., 1989. Stratigraphic context of fossil hominids from the Omo Group Deposits: Northern Turkana Basin, Kenya and Ethiopia. American Journal of Physical Anthropology, 78, pp. 595-622.

Feibel, C.S., Harris, J.M., and Brown, F.H., 1991. Paleoenvironmental context for the late Neogene of the Turkana Basin. *In*: Harris, J.M. (ed.), The Koobi Fora Research Project Volume 3: Fossil Ungulates: Geology, Fossil Artiodactyls, and Paleoenvironments. Clarendon Press, Oxford, UK, pp. 321-346.

Feibel, C.S., 1997a. A terrestrial auxiliary stratotype point and section for the Plio-Pleistocene boundary in the Turkana basin, East Africa. Quaternary International, 40, pp. 73-79.

---1997b. Debating the environmental factors in hominid evolution. GSA Today, 7, no. 3, pp. 1-7.

Findlater, I.C., 1978. Stratigraphy. *In*: Leakey, M.G. and Leakey, R.E. (eds.), The Koobi Fora Research Project Volume 1: The Fossil Hominids and an Introduction to their Context, 1968-1974. Clarendon Press, Oxford, UK, pp. 14-31.

Foody, G.M., 1996. Approaches for the production and evaluation of fuzzy land cover classifications from remotely-sensed data. International Journal of Remote Sensing, 17, no. 7, pp. 1317-1340.

Foody, G.M. and Cox, D.P., 1994. Sub-pixel land cover composition estimation using a linear mixture model and fuzzy membership functions. International Journal of Remote Sensing, 15, no. 3, pp. 619-631.

Frank, H., 1976. Stratigraphy of the Upper Member, Koobi Fora Formation, northern Karari escarpment, East Turkana Basin, Kenya. Iowa State University unpublished Masters thesis, Ames, IA, pp. 118.

GretagMacbeth, 2000. Munsell Soil Color Chart, pp. 56.

Gupta, R.P., 2003. Remote Sensing Geology. Springer-Verlag, Berlin, Germany, pp. 655.

Harris, J.W.K. and Isaac, G.L., 1997. Sites in the upper KBS, Okote, and Chari members: reports. *In*: Isaac, G.L. (ed.), The Koobi Fora Research Project Volume 5: Plio-Pleistocene Archaeology. Clarendon Press, Oxford, UK, pp. 115-220.

Hunt, G.L., 1980. Electromagnetic radiation--- the communication link in remote sensing. *In*: Siegal, B.S. and Gillespie, A.R. (eds.), Remote Sensing in Geology. John Wiley and Sons, New York, NY, pp. 5-45.

Jensen, J.R., 1996. Introductory Digital Image Processing: a Remote Sensing Perspective. Prentice Hall, Upper Saddle River, NJ, pp. 318.

Key, R.M. and Watkins, R.T., 1988. Geology of the Sabarei area. Republic of Kenya Ministry of Environment and Natural Resources, Mines and Geological Department Special Report 111, Nairobi, Kenya. pp. 58.

Leakey, M.G., Feibel, C.S., McDougall, I., and Walker, A., 1995. New four-million-year-old hominid species from Kanapoi and Allia Bay, Kenya. Nature, 376, pp. 565-571.

Leakey, M.G. and Leakey, R.E., 1978. The Koobi Fora Research Project, Volume 1: The Fossil Hominids and an Introduction to their Context, 1968-1974. Clarendon Press, Oxford, UK, pp. 191.

Lillesand, T.M. and Kiefer, R.W., 2000. Remote Sensing and Image Interpretation. John Wiley and Sons, Inc., New York, NY, pp. 724.

McDougall, I., 1985. K-Ar and $^{40}Ar/^{39}Ar$ dating of the hominid-bearing Plio-Pleistocene sequence at Koobi Fora, Lake Turkana, Kenya. Geological Society of America Bulletin, 96, pp. 159-175.

Morley, C.K., 1999. Geoscience of Rift Systems- Evolution of East Africa. AAPG Studies in Geology, 44, Tulsa, OK, pp. 242.

NASA JPL, 2003. Shuttle Radar Topography Mission (SRTM) digital elevation model, N04 E36, northern Kenya.

Pope, P.A. and Greene, M.K., 2005. Geologic Mapping through Linear Spectral Unmixing of MTI Imagery. Proceedings of the Pecora 16 Conference, Global Priorities in Land Remote Sensing, in press.

Price, J.C., 1995. Examples of high resolution visible to near-infrared reflectance spectra and a standardized collection for remote sensing studies. International Journal of Remote Sensing, 16, pp. 993-1000.

Rogers, M.J. and Harris, J.W.K., 1994. Changing patterns of land use by Plio-Pleistocene hominids in the Lake Turkana basin. Journal of Human Evolution, 27, pp. 139-158.

Savage, R.J.G. and Williamson, P.G., 1978. The early history of the Turkana depression. *In*: Bishop, W.W. (ed.), Geological Background to Fossil Man. Scottish Academic Press, Edinburgh, UK, pp. 375-394.

Sabins, F.F., 1997. Remote Sensing: Principles and Interpretation. W.H. Freeman and Co., New York, NY, pp. 494.

Settle, J.J. and Drake, N.A., 1993. Linear mixing and the estimation of ground cover proportions. International Journal of Remote Sensing, 14, no. 6, pp. 1159-1177.

Siegal, B.S. and Gillespie, A.R. (eds.), 1980. Remote Sensing in Geology: New York, NY, John Wiley and Sons, pp. 702.

Smith, M.O., et al., 1990. Vegetation in deserts: I. a regional measure of abundance from multispectral images. Remote Sensing of Environment, 31, pp. 1-26.

Tibaldi, A., and Ferrari, M., 1988. Potential of Landsat thematic mapper image for crystalline rock type discrimination. Geocarto International, 1, pp. 3-12.

Tucker, C.J., Grant, D.M., and Dykstra, J.D., 2004. NASA's global orthorectified Landsat data set. Photogrammetric Engineering and Remote Sensing, 70, no. 3, pp. 313-321.

Vidal, G.F., 1987. Characteristics of the Gregory Rift (Kenya): dynamics, ground structural analysis and remote sensing. Acta Astronautica, 15, no. 6/7, pp. 313-319.

White H.J., et al., 1981. Hominid habitats in the Rift Valley: part 1. *In*: Rapp, G. and Vondra, C. (eds.), Hominid Sites: their Geologic Settings. AAAS Selected Symposium 63 Proceedings, Washington, DC, pp. 57-113.

White, H.J., 1976. Stratigraphy of the Lower Member, Koobi Fora Formation, southern Karari Escarpment, East Turkana Basin, Kenya. Iowa State University unpublished Masters thesis, Ames, IA, pp. 134.

Williamson, P.G., 1982. Molluscan biostratigraphy of the Koobi Fora hominid-bearing deposits. Nature, 295, pp. 140-142.

Wolf, P.A. and Dewitt, B.A., 2000. Elements of Photogrammetry with Application in GIS. McGraw Hill, Boston, MA, pp. 608.

Los Alamos
NATIONAL LABORATORY
EST. 1943